Development and Characterisation of Plasmonic Devices for Sensing Applications

A thesis submitted to the
University of Waikato
for the degree
of
Doctor of Philosophy
by

Nemanya Sedoglavich

THE UNIVERSITY OF
WAIKATO
Te Whare Wānanga o Waikato

The University of Waikato
Hamilton New Zealand
September 2009

Abstract

In recent years, discoveries and advances that utilise nano-scale (10^{-9}m) structures and associated phenomena have led to a number of entirely new areas of research in the fields of physics, chemistry, biology, and materials science. The photonic field of plasmonics is the study of light interaction with nanometer-scaled metal-dielectric features, which gives rise to a variety of phenomena, including surface plasmon resonance, localised surface plasmon resonance, and metal enhanced fluorescence. The focus of this thesis is on the development and characterisation of nanophotonic devices, which utilise plasmonic phenomena and have potential for sensor applications.

During the course of this research a surface plasmon resonance analysis platform was devised, which utilises the gold grating of commercially available compact disks as the sensing substrate. This measurement method offers a high resolution refractive index analysis of gases and surface chemistry and is capable of analysing a large number of samples by scanning over the entire disk surface. The system implements a method of phase-polarisation contrast to improve the sensing performance. It enhances signal detection through redistributing the residual p-polarised waves, which have been strongly absorbed by the surface plasmon resonance substrate/sensor. This effectively lowers the reflected light intensity at the surface plasmon resonance minimum. The scheme results in the deepening of the intensity minimum to below 3.5% reflection and the enhancement of resonance to non-resonance contrast by up to 14 times, and thereby increasing sensitivity.

A range of new nanophotonic structures have been modelled, developed, fabricated, and characterised, which we call wavelength and polarisation selective polariton generators (SPGs). These polarisation-sensitive structures combine a tuneable plasmon resonator and a subwavelength aperture to selectively generate and transmit polaritons of a desired wavelength through a central nanohole. Individual SPGs permit modulation of transmission intensity, with calculated enhanced optical transmission (ratio of output to input flux) of up to 10 and up to 4-fold measured amplitude modulation. The paired SPGs gave rise to multiple spectrally discrete transmission peaks which, when modulated, provide a multi-state operation in a single device. The measured amplitude modulation was up to 10-fold. For the linearly continuous SPG, by controlling the polarisation as a tuning variable, it selectively generated and transported polaritons of a desired wavelength. It exhibited a spectral shift of 40 nm over the full range of polarisation angles. The modelled enhanced optical transmission was calculated to be up to 17.2. An instrument was developed for measuring and characterising light transmission through single nanoholes, nanohole arrays, and other complex structures. The operational characteristics of these elements show close agreement between model predictions and experimental data. It also demonstrates new designs of plasmonic structures which utilise selective behaviour based on the polarisation of incident light.

Acknowledgements

I wish to thank my chief supervisor Dr. Rainer Künnemeyer and my industry supervisor Dr. Johnathan Sharpe for their patience in guiding me through my research and most of all the friendship we developed along the way. Also, I would like to express my appreciation for letting me pursue a number of ideas during this study. It was this process of pursuing creative thoughts and critical analysis that has contributed most significantly to my personal and professional development.

I would especially like to acknowledge my family for their endless support over the past years. Since arriving from Serbia, together we have endured what can only be described as a rollercoaster ride. As migrants, the challenges imposed by the local people have only helped forge a closer, more determined, and unstoppable family. Achievement of one is the achievement of all.

A big thanks goes out to the unnamed heroes of this study, the many who have helped along the way with their skills, time, and questions. Also, I would like to thank HortResearch for letting me use their facilities over the past 3 years.

Thanks to the Top Achievers Doctoral Scholarship from Tertiary Education Commission.

Table of Contents

List of Figures

Chapter 1

1 INTRODUCTION

This thesis presents the work carried out at The Horticulture and Food Research Institute of New Zealand. The chapter sets the scene for the thesis. Sections 1.1 and 1.2 addresses the aim of the research, the main intended contributions, and the structure of the thesis.

In recent years, discoveries and advances that utilise nano-scale (10^{-9}m) structures and associated phenomena have led to a number of entirely new areas of research in the fields of physics, chemistry, biology, and materials science. The photonic field of plasmonics is the study of light interaction with nanometer-scale metal-dielectric features, which gives rise to a variety of phenomena, including surface plasmon resonance, localised surface plasmon resonance, and metal enhanced fluorescence. The study of these phenomena has yielded a number of new technologies vastly expanding the scientific and engineering capabilities of modern research. Some of the initial applications were in the medical field, like sensing of low concentrations of specific biological and chemical targets. This was followed by a wide range of developments in near-field, and fluorescence microscopy, industrial applications, and development of new types of (meta-) materials.

The ultimate application of such technologies has been identified as essential for solving many of the problems facing humanity today. The rapidly emerging field of nanophotonics is studying and utilising these highly complex phenomena to yield completely new sensing approaches in biology and medicine, to address the energy needs of the world through improvements in solar energy capture, and

potentially to meet the ever-demanding needs of increased computer processing power with decreased size.

Much has recently been learnt regarding the fabrication of objects with nanometer dimensions, in many instances, using relatively simple techniques and equipment. This comparative simplicity has made very fundamental studies of object interactions at a molecular scale possible without the need for expensive equipment and facilities.

The literature review has identified a research direction into sensor platforms which offer higher sensitivity, lower cost, faster, and multi-analyte readout. This is covered in more detail in chapter 2.

1.1 Research objectives

The purpose of this research is the development and characterisation of nanophotonic devices, which utilise plasmonic phenomena and have potential for sensor applications. The key elements of this research are to design, fabricate, test, and optimise the devices.

The foundation of plasmonic based sensors is based on a photon coupling mechanism between photons and oscillating electron waves, referred to as a plasmon resonance condition. This research seeks to combine aspects of electronics, photonics, and nanotechnology to develop, characterise, and report on new plasmonic devices.

The thesis has three main objectives:

The first objective is to develop and characterise (explore function of) a gold grating surface plasmon resonance sensor platform for use with one or multiple target samples. Look into improving the platform sensitivity along with utilizing a

low cost substrate. This work has led to two conference presentations regarding phase-polarisation contrasting technique (Sedoglavich et al. 2007b) and surface plasmon resonance imaging (Sedoglavich et al. 2007a), and produced a publication on the implementation of phase-polarisation contrasting (Sedoglavich et al. 2008b).

The second objective is to gain scientific understanding of the operation of localised surface plasmon resonance devices. The aim is to develop an instrument for resolving transmission of single nanoholes in arrays and other complex structures, as a tool for characterising individual nano-scale devices. This work has contributed to the publication on implementation of gold nanohole arrays as immunoassays (Sharpe et al. 2008).

The third objective is to model, develop, fabricate, and characterise new nanophotonic structures based on plasmonic phenomena. The intent of the objective is to explore new designs of nanophotonic structures, utilising selective behaviour based on the polarisation of incident light. This work has led to a conference presentation (Sedoglavich et al. 2008a) and two publications on selective polariton generator structures (Sedoglavich et al. 2008c; Sedoglavich et al. 2009).

The findings of this study could provide potentially helpful information about the instrument design of surface plasmon resonance imaging platforms and open new avenues into nanophotonic structures, which offer polarisation and wavelength selective behaviour. Potential for further research and applications of this selective behaviour is in the areas ranging from polariton generators, and multi-state nanophotonic switching and devices, to tuneable spectroscopic elements, and biosensors.

1.2 Thesis outline

This thesis is divided into seven chapters and four appendices. Chapter two introduces the nanophotonic field of plasmonics by discussing the background of plasmonics, critically evaluates the relevant literature on the implementation and applications of these phenomena. Furthermore, it explains a variety of optical phenomena that arise within plasmonics and talks about the experimental instrumentation during this research work.

Chapter three describes the development of a surface plasmon resonance sensing and analysis platform, which is capable of scanning over a large number of samples. The platform uses the excitation of surface plasmon resonance on a gold grating compact disk. The system utilises a method of phase-polarisation contrast to improve the system sensing performance.

Chapter four discusses the design and implementation of the far-field, spatially resolved single nanohole transmission instrument. The setup was used for characterising single nanoholes by scanning over the nanohole array surface.

Chapter five explains the polariton generator structures with the emphasis on polarisation and wavelength selective behaviour. Data from the finite-difference time-domain software simulation, and the experimental results of the fabricated structures are presented.

Chapter six reviews the development of the compact disk surface plasmon resonance analysis platform, and the new polariton generator structures. The chapter concludes by recalling the thesis aims and objectives, and comments on their achievement. It further expands on the direction of future work and also potential applications.

Chapter 2

2 LITERATURE REVIEW

The focus of this study is the development and characterisation of nanophotonic devices, which utilise plasmonic phenomena and have potential for sensor applications. The key elements of this research are to design, fabricate, test, and optimise the devices. This chapter introduces the nanophotonic field of plasmonics discussing its background and related literature relevant to the present research. This discussion will serve as the starting point for defining the direction of the research. The section 2.1 introduces surface plasmon resonance, localised surface plasmon resonance, single nanohole apertures, and enhanced optical transmission. Enhanced optical transmission is defined as the ratio of the output to input power flux. It follows on to explain the principles of surface plasmon waves and a variety of optical phenomena that arise in plasmonics. Section 2.2 illustrates their application and instrumentation in the area of bio-chemical sensing.

2.1 Background of plasmonic phenomena

The phenomenon of anomalous diffraction on diffraction gratings due to the excitation of surface plasmon waves was first described by Wood (1902). A practical and commonly used method to optically excite surface plasmons by attenuated total reflection was suggested in two publications in 1968, one by Kretschmann and Raether (1968), and the other by Otto (1968). Using total internal reflection, light passes through a glass prism on a metal film deposited onto a glass substrate. At the surface plasmon resonance angle the momentum of the incident photon matches that of the charge density wave, absorbing the photon energy into surface plasmon waves, causing a dip in reflected intensity. The dip in

intensity is the basis of sensor applications, where the resonance angle change is monitored (Homola et al. 1999a).

The understanding of surface plasmon resonance has lead to a rapid increase in surface plasmon studies, giving rise to the field of plasmonics. The field examines the interaction of light with surface plasmon waves through metal-dielectric interfaces. Depending on the geometric features and physical properties at the metal-dielectric interface, a variety of plasmonic phenomena may occur, ranging from travelling to localised surface plasmon waves.

The nanophotonic field of plasmonics is the study of light interaction with nanometer-scaled metal-dielectric features. These features can be designed to meet momentum matching conditions of incident light and surface plasmon waves. This gives rise to a variety of phenomena that include surface plasmon resonance, localised surface plasmon resonance, metal enhanced fluorescence, surface plasmon coupled emission, subwavelength enhanced transmission, and new metamaterials (Lakowicz 2005; Barnes et al. 2003).

Over the past two decades the study of plasmonic phenomena has yielded a number of new technologies ranging from highly sensitive chemical or biological sensors and improved light emitting diodes to alternative solar power generation. A range of upcoming advancements includes metamaterials, promising the potential of perfect lens and cloaking techniques for optical invisibility.

Very recently, a number of fascinating and quite unexpected discoveries have also been made with light interactions with matter at the nano-scale. Examples include extremely high frequency switching, high absorption, and ultra-sensitive spectroscopy. These effects are not completely understood, but hold significant promise to major increases in computing power, solar energy efficiency, and measurement applications.

2.1.1 Surface plasmon resonance

Surface plasmon resonance (SPR) is a charge-density oscillation that may exist at the interface of a metal and a dielectric. Predominant to this phenomenon is the role of surface waves such as surface plasmons. These are electromagnetic waves trapped at a metallic surface through their interaction with the free electrons of the metal. They result under special momentum matching circumstances where energy is transferred from a photon into an oscillating electron wave (Homola et al. 1999b). This phenomenon can be observed as a sharp decrease in reflected light intensity at the resonant angle. The electromagnetic field of surface plasmons has maximum intensity at the metal-dielectric interface, decaying exponentially into both media. The evanescent field of the surface plasmon waves interacts with the close vicinity of the interface. Changes in the optical properties of this region cause a change in the SPR angle. This is the basis of the use of SPR for biological and chemical sensing purposes (Cullen et al. 1987).

The surface plasmon wave (SPW) is a transverse-magnetic (TM) polarised wave; the magnetic field vector is perpendicular to the direction of propagation of the SPW and parallel to the plane of interface. This is also often referred to as p-polarised lights. For a semi-infinite dielectric-metal interface, the wavenumber, k_{SP}, of the surface plasmon wave travelling along the surface of the interface is given by the expression (Homola et al. 1999a),

$$k_{SP} = \frac{2\pi}{\lambda_0}\sqrt{\frac{\varepsilon_{mr} n_D^2}{\varepsilon_{mr} + n_D^2}}, \qquad \text{Eq. 2-1}$$

where λ_0 is the free space optical wavelength, ε_{mr} the real permittivity of the metal, and n_D the refractive index of the dielectric. The SPW may be supported

by the structure, provided $\varepsilon_{mr} < -n_D^2$. At optical wavelengths, this condition may be fulfilled by a number of metals such as gold, silver, and aluminium.

Following from Eq. 2-1, the propagation constant of surface plasmons is always higher than that of the optical wave propagating in the dielectric, which prevents the surface plasmons from being excited directly by the incident optical wave at a planar metal-dielectric interface. Therefore, for the momentum matching condition to be met, the momentum of the incident optical wave, k_S, has to be increased to equal that of the surface plasmon wave, $k_{SP} = k_S$. The momentum enhancement is commonly achieved by means of attenuated total reflection in optical waveguides and prism couplers (Liedberg et al. 1995; Homola et al. 1999a), subwavelength features (Brolo et al. 2004; Barnes et al. 2003) and diffraction at the surface of gratings (Singh and Hillier 2006; Lawrence et al. 1996; Homola et al. 1999a).

Grating based surface plasmon resonance

The advantage of grating-based SPR over prism coupled sensing includes the fact that a prism is not necessary to excite surface plasmons, and the optical quality of the substrate is not crucial. A drawback for certain applications is that in grating-based SPR systems, the light propagates through the sample solution and therefore the analyte and flow-cell need to be optically transparent (Singh and Hillier 2006).

For a periodically modulated interface between a metal and a dielectric with period, Λ, the surface component of the wavevector, $2\pi/\lambda_0$, of the incident light can increase (or decrease) by integral multiples of the grating wavevector, $2\pi/\Lambda$, (Singh and Hillier 2006). If the surface component matches that of SPWs in the metal, it can couple to and excite them. Therefore, momentum can be matched using metal diffraction gratings. The wavevector of the surface component diffracted wave, k_S, is calculated as

$$k_S = \frac{2\pi}{\lambda_0} n_D \sin\theta_0 + m\frac{2\pi}{\Lambda}, \qquad \text{Eq. 2-2}$$

where θ_0 is the angle of incidence and m is an integer (0, ±1, ±2...) indicating the order of diffraction. Matching of the incident light with the SPWs occurs when k_S equals k_{SP}. For surface plasmons that propagate in the forward direction, the diffracted order of m = +1 will result in the strongest coupling (Pockrand and Raether 1976; Fontana 2004). When this coupling occurs, a sharp resonance dip is observed in the reflectance of p-polarised light, while the s-polarised light is not affected.

2.1.2 Localised surface plasmon resonance

Nanometer scale confinement of surface plasmon waves, such as in metal nanoparticles, gives rise to the phenomenon of localised surface plasmon resonance (LSPR). The LSPR results when the incident photon frequency is in resonance with the collective oscillation of the free electrons of the nanoparticles. As well as tuneable optical properties this confinement produces the intense scattering and absorption of light seen in noble metal nanoparticles.

Mie theory is a theoretical approach for modelling the optical properties of nanoparticles estimating the extinction coefficient of a metallic sphere in the long wavelength, electrostatic dipole limit. This is given by the following expression (Kreibig and Vollmer 1995):

$$E(\lambda) = \frac{24\pi N_A a^3 \varepsilon_D^{3/2}}{\lambda \ln(10)} \left[\frac{\varepsilon_{mi}}{(\varepsilon_{mr} + 2\varepsilon_D)^2 + \varepsilon_{mi}^2} \right], \qquad \text{Eq. 2-3}$$

where $E(\lambda)$ is the extinction coefficient which is equal to the sum of absorption and Rayleigh scattering, N_A is the density of nanoparticles, a is the radius of metallic nanospheres, ε_D is the dielectric constant of the medium surrounding the metallic nanosphere (assumed to be a positive, real number and wavelength independent), λ is the free space wavelength of the absorbing light, ε_{mi} is the imaginary part of the metallic nanosphere's dielectric permittivity, and ε_{mr} is the real part of the metallic nanosphere's dielectric permittivity. The LSPR condition is met when $(\varepsilon_{mr} + 2\varepsilon_D)^2$ in the denominator approaches zero. From the above equation Eq. 2-3 the LSPR spectrum of a nanoparticle depends on its radius, material, and the environment's permittivity.

2.1.3 Single nanohole apertures

Characteristics of a single hole milled in a metal film (e.g. gold) are determined by the hole diameter and its depth. In defining the system, Bethe (1944) simplified the structure to be infinitely thin and the metal to be a perfect conductor. With these assumptions he proposed that the transmission efficiency, η, normalized to the area of the hole, scales as $\left(\frac{D}{\lambda}\right)^4$, where D is the hole diameter and λ is the wavelength, It is given by the following equation:

$$\eta = \frac{64\pi^2}{27}\left(\frac{D}{\lambda}\right)^4, \qquad \text{Eq. 2-4}$$

Eq-2-4 shows that the transmission efficiency rapidly decreases as the hole diameter is reduced, where the cut-off wavelength is defined when $\lambda > 2D$. Gordon and Brolo (2005) have found that the real cut-off condition occurs at longer wavelengths, when the finite conductivity is taken into account.

Another prediction made by Bethe (1944) was that the light would diffract as it emerges from the hole in an annular pattern that depends on the orientation relative to the polarisation of the incident light. If the diffraction pattern is scanned along the direction of incoming polarisation, the intensity should be constant (like a spherical wave plane), while in the perpendicular direction, the intensity decreases with increasing angle. In the later case, the angular dependence is a $\cos^2\theta$ function.

The use of near-field scanning optical microscopes for enhanced transmission phenomenon stimulated experimental studies (Yin et al. 2004; Degiron et al. 2004), the results of which challenge Bethe's predictions, as in real metals it cannot be modelled as a infinitely thin sheet of a perfect conductor. Specifically, angular measurements at the output of subwavelength apertures show that the light diffracts less then expected and the transmitted light can have unexpected features where the circular aperture has a peak in the transmission spectrum not predicted by equation Eq. 2-1 (Degiron et al. 2004). Also, the results challenge the proposal that the transmission, normalised to the area of the hole, scales as $\left(\frac{D}{\lambda}\right)^4$.

2.1.4 Enhanced optical transmission

Enhanced optical transmission is defined as the ratio of the output to input power flux, e.g. the output power over the nanohole area divided by the power over the illuminated surface area.

According to diffraction theory, apertures smaller than the wavelength of light have very low transmission. Since Ebbesen et al. (1998) reported enhanced optical transmission through nanohole arrays in metal films, there has been significant interest in understanding and utilising the interactions of nano-geometries on metal-dielectric interfaces. Surface waves such as surface plasmons, play a principal role in this phenomenon.

Excitation and localisation of surface plasmon polariton (SPP) modes in metal-dielectric structures can be utilised to construct unique nanophotonic materials and devices with tuneable optical transmission (Barnes et al. 2003). To explore plasmon resonance effects, a range of geometries have been modelled and characterised, such as nanohole arrays (Ebbesen et al. 1998; Chang et al. 2005), slit with corrugations (Lezec et al. 2002; Garcia-Vidal et al. 2003) and apertures with annular corrugations (Lezec et al. 2002).

Nanohole arrays

Due to simple design, the spectral properties of periodically spaced nanoholes in thin metal films can be tuned. This has resulted in nanohole arrays being utilised in a number of applications. It was reported by Ebbesen et al. (1998) that nanohole arrays in metal films exhibit enhanced optical transmission, where the transmission spectrum contains peaks with transmission efficiency larger than one. This was true even when the individual holes were so small that all light propagating within the holes was evanescent. At the peak transmission, standing surface plasmon waves are formed on the surface. The intensity of the surface plasmon electromagnetic field above each hole compensates for the inefficient transmission through each individual hole (Genet and Ebbesen 2007). The peak wavelength position, $\lambda_{\max}$, at normal incidence is given by the first order approximation (Genet and Ebbesen 2007):

$$\lambda_{\max} = \frac{\Lambda}{\sqrt{\frac{4}{3}\left(i^2 + ij + j^2\right)}} \sqrt{\frac{\varepsilon_m \varepsilon_D}{\varepsilon_m + \varepsilon_D}}, \qquad \text{Eq. 2-5}$$

where Λ is the period of the array, ε_m and ε_D are the dielectric permittivity of metal and the dielectric material in contact with the metal, respectively. i and j are the scattering orders of the array.

Surface plasmon antenna - single nanohole surrounded by corrugations

Nanostructures consisting of annular grooves and gratings in metal films exhibit properties such as photon to plasmon coupling (Lezec et al. 2002), focusing (Steele et al. 2006; Liu et al. 2005), and intensity enhancement (Steele et al. 2006; Liu et al. 2005). Modern nanofabrication techniques, such as electron beam lithography and focused ion beam milling enabled the design and production of structures with complex surface wave dynamics (Degiron et al. 2004; Garcia-Vidal et al. 2003). A number of groups have extensively researched and characterised the properties of circular surface plasmon (SP) antennae (Shuford et al. 2006; Hofmann et al. 2007), a single aperture surrounded by annular corrugations.

The periodic structures act as antennae, coupling the incident light into SPs for a specific wavelength. This results in a high intensity electromagnetic field at the surface above the nanohole, producing high transmission efficiency and a well defined spectrum. As defined by the Eq. 2-2, the incident light momentum can be matched to surface plasmon waves using metal diffraction gratings. Therefore, a single aperture surrounded by a periodic corrugation in the metal surface will also display surface plasmon-enhanced transmission.

2.2 Implementation and applications of plasmonic phenomena

The following section presents the implementation and applications of plasmonic phenomena. It covers the work of various international research groups in the areas of surface plasmon resonance, enhanced optical transmission, and subwavelength structures.

A grating-based gas sensor, with silver as the SPR active metal, has attained high sensitivity of 1000 nm spectral shift per refractive index unit (RIU) in wavelength

interrogation mode (Jory et al. 1994). In angular interrogation mode, the system's sensitivity is about 100° shift per RIU (Homola et al. 1999b). Another approach was the measuring of the modulation frequency with the use of an acousto-optical modulator has recently been reported (Jory et al. 1995). This technique improves the accuracy with which the resonant wavelength in a wavelength interrogation-based SPR sensor is detected to about $5x10^{-4}$ nm and leads to a sensor resolution of better than $1x10^{-6}$ RIU. The grating method has also been used for the excitation of surface plasmon waves (SPW) in an optoelectronic SPR-sensing device based on a Schottky-barrier semiconductor structure (Nikitin and Beloglazov 1994; Nikitin et al. 1997). The resolution is as high as $1x10^{-5}$ RIU.

A number of surface plasmon imaging configurations have been reported (Wilkop et al. 2004; Smith and Corn 2003; Xinglong et al. 2005; Nikitin et al. 2000). The use of SPR imaging as a method for screening biomolecular interactions has been described by Smith and Corn (2003). They analysed the reflected light intensity at a fixed reflection angle. The angle is set to the linear region of the reflection gradient where spatial changes in reflected light intensity are measured across a substrate. This was a result of a resonance angle change, shifting the SPR curve and producing a reflected intensity change at a specific observation angle. Nelson et al. (2001) used five-phase Fresnel calculations to determine the samples' corresponding refractive index based on the change in reflected intensity percentage, as measured through SPR imaging. The main limitation of these approaches to SPR imaging is the small dynamic range, which is only over the linear region of the reflection gradient at a single interrogation angle.

The concept of surface plasmon resonance interferometry has been introduced as a novel method for sensing, in which phase and/or intensity of the reflected light is utilised (Nikitin et al. 1999; Kabashin et al. 1998). An interferometry based setup that detects the phase of a beam reflected under surface plasmon resonance has been developed for biological and chemical sensing by Nikitin et al. (2000). The phase of reflected light abruptly jumps in response to a small change in the

effective thickness of a receptor layer that binds analyte particles on the sensor surface. This formed the basis for biosensing with much higher sensitivity compared to traditional SPR sensors, achieving the resolution of 10^{-7} refractive index units. Their approach to SPR interferometry also provided spatial resolution at the micron scale, a form of SPR imaging.

Another method of SPR interferometric imaging has been reported by Xinglong et al. (2005) for micro-array analysis. The authors implemented common optical path polarisation interferometry, which offers better immunity to environmental noise and drift than the traditional methods of intensity measurement SPR imaging and different optical path SPR interferometry. The setup utilised a Wollaston prism to achieve interference of the p- and s-polarised light, introducing spatial phase modulation measurement to the configuration.

An important fact to note is that a dramatic change in the phase under resonance, due to variation of coating thickness or refractive index, occurs only within a narrow range, near the minimum reflected intensity of the SPR dip (Nikitin et al. 1999; Kochergin et al. 1998). To maintain the high sensitivity over a wider dynamic range, the authors suggest a wavelength feedback control.

Another interesting concept for surface plasmon resonance sensing was the suggestion of using a one-dimensional photonic band-gap material as a replacement for the metal film (Shinn and Robertson 2005). The multilayer material provides enhanced sensitivity because of the low material losses, and may be designed to work at any desired wavelength. The setup still implements a glass prism coupling format. The development of these photonic band-gap based sensors is possible with the current readily available commercial thin film fabrication technology, for making simple one-dimensional multilayer systems (Shinn and Robertson 2005).

A number of groups in sensor development use diffraction grating for optical excitation of surface plasmon waves. Nikitin and Beloglazov (1994) presented a multi-purpose sensor concept based on surface plasmon resonance in a Schottky barrier structure for photoelectric signal generation. A metal film grating was combined with a semiconductor into a single solid structure, where resonant photoelectric enhancement is generated when surface plasmon polaritons are resonantly excited on the grating. Lawrence et al. (1996) investigated whether a perspex replica of a holographic diffraction grating can be used as a momentum coupling device. Their work indicated that low cost, easy to fabricate replicas may offer disposable substrates for biosensors.

A surface plasmon resonance sensor array based on a grating substrate was developed for the detection of biomolecular interactions by Singh and Hillier (2006). The substrate is a gold grating prepared by wet chemical treatment of a commercial recordable compact disk (CD-R). Changes in plasmon resonance were monitored in a fixed-angle imaging configuration, looking at the intensity along the reflection gradient. The SPR imaging readout from the CD-R surface was improved by capturing the p- and s-polarised light, producing normalised intensity. This was achieved by dividing the reflected intensity of p- by that of s-polarised light. Their grating-based SPR imaging platform showed a simple method of performing fluorescence-label-free, high sensitivity and high throughput detection of biomolecular interactions.

The work of Singh and Hillier builds on the previously reported use of gold grating from commercial CD-R, where it was found that the pitch in the pregroove is sufficient to excite surface plasmons in air (Fontana 2004). They also found that all raw images captured using p-polarised light showed light and dark bands, similar to interference fringes. These bands appear parallel to the grating ridges, but their origin was unclear. Fast-Fourier transform was performed to reduce the impact of these bands in data analysis, removing its associated frequencies.

A phase-polarisation contrast (PPC) technique was reported by Kabashin et al. (1998) for the enhancement of contrast in the surface plasmon resonance intensity profile, exploiting the light phase and intensity behaviour under SPR. The setup implements glass prism coupling. It is well established that for an arbitrary dielectric layer on a metal film, the reflected intensity can be suppressed at an optimum film thickness (Kabashin et al. 1998). However, practical SPR biosensors usually have a number of biomolecular layers immobilised on the metal surface, preventing the metal thickness from being pre-set to optimum. PPC applies to non-optimum SPR coupling conditions, lowering the resonant minimum of reflected intensity nearly to zero. Kabashin et al. (1998) in their experiments achieved the deepening of the minimum down to 1% and a contrast enhancement of about 20 fold.

Another instrument was reported by Wu and Pao (2004) which utilises phase detection at surface plasmon resonance in a total internal reflection configuration. The SPR response curve was optimised and sensitivity increased by applying a quarter-wave-plate in front of and behind the sensor. This sensitivity adjustable optical sensor was reported to have a resolution of 1×10^{-6} refractive index units.

Enhanced optical transmission by nanohole arrays in metal films has been extensively studied. Experiments have provided evidence that these optical properties are due to the coupling of light with surface plasmons of the two-dimensional array of subwavelength holes, patterned on a metal film (Ebbesen et al. 1998). This study was followed by a proliferation of publications of experimental and theoretical work regarding isolated nanoholes and nanohole arrays in thin metal films (Chang et al. 2005; Shuford et al. 2007; Prikulis et al. 2004; Degiron et al. 2004; Gordon et al. 2004; Chen et al. 2007; Degiron and Ebbesen 2005). Gordon et al., Degiron and Ebbesen, and DiMaio and Ballato (2006) examined a number of nanohole arrays with polarisation sensitive transmission, by varying the nanohole shape and array layout configuration.

Another work on periodic arrays considered subwavelength double-hole apertures in 100 nm gold films, resulting in controlled and predictable surface-enhanced Raman scattering (Lesuffleur et al. 2007). Shuford et al. (2007) examined the electric field properties of far-field illuminated single subwavelength cylindrical apertures. The largest enhancements are localised at the edge of the aperture, where both the entrance and the exit edges of the hole may produce intense fields. Theoretical studies have shown that in addition to such surface plasmon modes (Popov et al. 2005a) other resonant modes defined along the depth of the hole might also contribute to the transmission signal (Garcia-Vidal et al. 2005).

Leebeeck et al. (2007) reported a microfluidic device with integrated surface plasmon resonance chemical and biological sensors, based on arrays of nanoholes in a gold film. A sensitivity of 333 nm resonance wavelength shift per RIU was demonstrated with this device.

Small apertures are routinely used in scanning near-field optical microscope tips to explore electromagnetic fields in the immediate vicinity of a surface with subwavelength resolution (Betzig and Trautman 1992). Recently, nanometre sized apertures were used in fluorescence correlation spectroscopy (Levene et al. 2003; Rigneault et al. 2005), a technique for the study of diffusion and reaction of single fluorescent biomolecules. By using small apertures in metal, the analysis volume was reduced by a factor of 1,000 allowing them to study molecular events at close to biological conditions.

A chip based biosensor array was constructed with 600 nm period nanoslits and 50 nm widths on a 150 nm thick gold film (Lee et al. 2007). The detection sensitivity is up to 668 nm resonant wavelength shift per RIU, a significant improvement compared to the previously reported sensitivity of nanohole arrays.

Prikulis et al. (2004), Degiron et al. (2004), Gordon et al. (2006) have reported work on isolated holes in optically thin gold films, which showed localised

surface plasmon resonance in the red to near-infrared region. There is a red shift with increasing hole diameter or increasing refractive index of the surrounding medium. Pronounced blue shift is observed when the distance between holes is decreased, which indicates enhanced surface plasmon polariton coupling between holes. Degiron et al. (2004) suggest that these properties follow from the dipolar nature of the localised surface plasmon resonance and can be tuned by an appropriate design of the aperture shape, also leading to polarisation selective characteristics.

A few groups (Cui et al. 2004; Csaki et al. 2006) have published work on characterisation and integration of nanoparticles inside nanohole arrays, designing photonic composite materials as a new format for plasmonic devices. Another group (Baida and Labeke 2003) presented a new design configuration of nanohole arrays, using finite-difference time-domain simulations that show transmission efficiency may reach 80% in the visible spectral range. This was achieved by filling the central region of each hole with a concentric cylinder of smaller diameter, resulting in a periodic array of annular apertures.

Another significant improvement in transmission enhancement of nanohole arrays was reported with the use of plasmonic Bragg reflector structures (Marthandam and Gordon 2007). The structures consisted of periodic depressions, while another design uses corrugations. To meet the Bragg reflection condition, the periodicity of the plasmonic Bragg reflectors were chosen to be half the periodicity of the array. In order to reflect in-phase with the light from enhanced optical transmission, the plasmonic Bragg reflectors are placed half a period away from the array.

Njoh et al. (2007) presented experimental observations of highly collimated beams of radiation generated when a periodic subwavelength grating interacts with surface plasmon polariton modes of a thin gold film. A number of groups have studied optical transmission through a circular nanohole in a metal film

surrounded by concentric circular corrugations, either on illumination, exit or both sides (Lezec et al. 2002; Popov et al. 2005b; Shuford et al. 2006; Degiron and Ebbesen 2004). The structures are often called surface plasmon antennae. These groups have shown that the spectral dependence of the transmission has a sharp intensity maximum related to the surface plasmon excitation of the illuminated corrugations.

Extensive finite-difference time-domain studies have been performed by Shuford et al. (2006), who found that light transmission is extremely sensitive to the hole size, corrugation period and corrugation depth. The authors determined a set of corrugation parameters that optimise transmission. One of the suggestions is that the optimal corrugation depth is 15%-20% of the corrugation period.

Lezec et al. (2002) published experimental work on the benefits of periodic corrugations on the exit side of a single aperture. This confined the transmitted light to emerge from the aperture as a beam with narrow angular divergence (approximately ±3°). The structures were fabricated using focused ion beam milling of a 300 nm thick silver film. The corrugations on the exit side were combined with the corrugations on the illuminated side of the single aperture, providing surface plasmon enhanced and narrow beam transmission. They reported two formats of structures, a single nanohole encircled by concentric corrugations and a single subwavelength slit flanked by parallel corrugations on each side.

Other groups have also presented experimental and theoretical work on a single subwavelength slit flanked by parallel grooves (Garcia-Vidal et al. 2003; Martin-Moreno et al. 2003). Garcia-Vidal et al. have identified three primary mechanisms that may enhance optical transmission: groove cavity mode excitation (controlled by the depth of the corrugations), in-phase groove re-emission (controlled by the corrugation array period), and slit waveguide mode (controlled by the thickness of the metal film). The structures were fabricated using focused ion beam milling.

The light transmission was enhanced by up to 2 orders of magnitude when all three mechanisms coincide. Bravo-Abad et al. (2003) explored the transmission properties of single subwavelength apertures in a thin metal film flanked by asymmetric configurations of periodic grooves. This structure has managed to simultaneously transmit two different wavelengths. By tuning the geometric parameters defining the corrugation of the output side, these two wavelengths can emerge from the structure as two very narrow beams propagating in well-defined directions.

Ishi et al. (2005) proposed a nano-photodiode concept with a subwavelength active area using the enhanced optical near-field of surface plasmon resonance. They fabricated a silicon Schottky photodiode consisting of a 300 nm diameter active area and a surface plasmon antenna. The photodiode showed an increased photocurrent of several orders of magnitude, compared to that without a surface plasmon antenna. Such a nano-photodiode configuration can result in a high-speed optical signal detector as the optoelectronic conversion process occurs within subwavelength scale.

2.2.1 Other related literature

The following presents some of the other related literature that is not directly related to this research but has contributed to the understanding of the field.

Near-field scanning optical microscope study of isolated nanoholes in 100 nm thick Au film has been reported, investigating the generation of surface plasmon polaritons (Yin et al. 2004). The results were interpreted using finite-difference time-domain numerical models. This may be accompanied by the work on transmission of light through single rectangular holes, exhibiting polarisation dependent behaviour (Garcia-Vidal et al. 2005).

Focusing of surface plasmons has been reported with circular and elliptical structures (Liu et al. 2005) and circular gratings (Steele et al. 2006) as plasmonic lens. Both sets of experiments were carried out using a near-field scanning optical microscope. The focusing mechanism of the circular grating is explained with a coherent interference model of surface plasmon polariton generation on the grating by the incident field (Steele et al. 2006). Plasmonic modes of annular resonators fabricated on Ag and Au surfaces were imaged by spectrally resolved cathodoluminescence (Hofmann et al. 2007). This technique produced high resolution images of plasmonic mode excitation.

Cubukcu et al. (2006) demonstrated a plasmonic laser antenna composed of a plasmon resonant optical antenna integrated on the facet of a commercial diode laser, generating enhanced and spatially confined optical near fields with spot sizes of a few tens of nanometers operating at a 830 nm wavelength. The localised plasmon characteristics of single 60 nm nanoholes were investigated and their applicability demonstrated for bio-chemical sensing similar to localised plasmon characteristics of nanoparticles (Rindzevicius et al. 2005).

One group reported experimental results of exceptionally high transmission levels (up to 39%) from planar metallic film closely coupled to periodic nanohole array structure (Lin et al. 2006). An interesting work on focusing of light by nanohole quasiperiodic arrays in metal films has been published with ~290 nm wide, high intensity spots at a distance of ~12.5 μm from the array (Huang and Zheludev 2007).

There has been a report on the excitation of surface plasmon polaritons on a periodic arrangement of metallic ribbons with a tuneable spacing (Rehwald et al. 2007). The material's ability to vary its lattice constant results in an additional degree of freedom which permits the excitation of surface plasmon polaritons for any combination of wavelength and angle of incidence within the tuning range of the system.

The chapter has reviewed literature relevant to the research objectives. The purpose was to provide a brief description of plasmonic phenomena, formats of implementation, and the applications in the area of bio-chemical sensing. Three areas were emphasised: grating based surface plasmon resonance sensing and imaging, nanohole arrays, and single aperture devices. The chapter is a starting point for the research direction. The following chapter presents the work on a surface plasmon resonance analysis platform.

Chapter 3

3 GOLD COMPACT DISK SURFACE PLASMON RESONANCE ANALYSIS PLATFORM

Surface plasmon resonance (SPR) has been used for some time in chemical and biological sensing. Some of the schemes for exciting surface plasmons include prisms and gratings. Grating-based optical SPR sensors have been demonstrated, which use light intensity variations at resonance or wavelength interrogation. Recently, a gold grating made from a commercial recordable compact disk was used for excitation of surface plasmons (Singh and Hillier 2006). This chapter presents a surface plasmon resonance analysis platform with a new grating configuration that combines the benefits of multi-angle interrogation with the phase-polarisation contrast method. It also offers analysis of a large number of samples. The experimental results are shown, providing the concept and the capabilities of the technique.

3.1 Introduction

The platform is based on the gold grating of a commercially available recordable compact disk (MAM-A Gold CD-R), whose pregroove pitch is sufficient to excite surface plasmons at the air-gold interface. The compact disks are mass produced by injection-moulding, resulting in low cost disposable grating substrates.

At the surface plasmon resonance angle the momentum (along the interface) coincides with the incident photon and the charge density wave. The photon energy is then transferred to the charge density wave. This phenomenon can be observed as a sharp dip in the reflected light intensity at the resonant angle. The evanescent field of the surface plasmon wave interacts with the close vicinity of

the interface. The changes in the optical properties of this region will therefore influence the SPR angle, which is the basis of chemical and biological sensing.

The use of a gold grating from a commercial recordable Compact Disk (CD-R) for excitation of surface plasmons (Fontana 2004) and development of SPR imaging (Singh and Hillier 2006) were recently reported. However, the CD-R grating is not optimal for SPR analysis as at resonance the intensity minima drops to ~45% of maximum intensity.

Therefore, to optimise the SPR analysis system, the phase-polarisation contrast technique was implemented as it exploits the interference between s- and p-polarised light to increase the intensity difference (drop in SPR minima).

3.2 Surface plasmon resonance on gold compact disks and digital versatile disc gratings

The SPR excitation angle, Eq: 3-1, shown in the Appendix C, equates the momentum matching equations of the incident light, Eq: 2-1, and the plasmons on the gold grating, Eq: 2-2.

$$\theta_{SPR} = \sin^{-1}\left(\frac{\frac{2\pi}{\lambda_0}\sqrt{\frac{\varepsilon_{mr}\varepsilon_d}{\varepsilon_{mr}+\varepsilon_d}} - \frac{2\pi m}{\Lambda}}{\frac{2\pi}{\lambda_0}} \right) \qquad \text{Eq: 3-1}$$

Strongest coupling of incident light to surface plasmons that propagate in the forward direction (Figure 3-1) is achieved for diffracted order of m = +1 (Fontana 2004). The compact disk grating period is $\Lambda = 1560 \times 10^{-9}$ m. The electric permittivity of gold is $\varepsilon_m = -11.84 + i1.36$ ($\varepsilon_m = \varepsilon_{mr} + i\varepsilon_{mi}$) and of air is $\varepsilon_d = 1.000584$. The electric permittivity of gold is taken from Singh and Hillier (2006), which matches the data provided by Lumerical Solutions, FDTD software

at 650 nm. Eq: 3-1 then predicts the SPR response at the incident angle of 38° for m = +1 and $\lambda_0 = 670$ nm.

The SPR signal was also detectable for back illumination of the grating surface through the polymer layer, which permits the use of a flow-cell where the sample transmittance would not affect the SPR readout. However, the back illuminated approach suffers from total internal reflection, for high incidence angles to the normal.

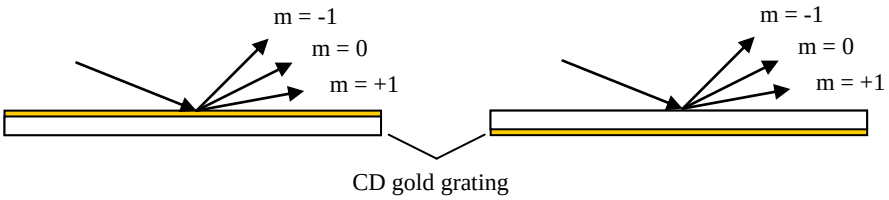

Figure 3-1 Strongest coupling of incident light to the surface plasmons that propagate in the forward direction is achieved for diffracted order of m = +1.

The SPR profile of the gold grating disk was acquired using an intensity interrogation technique, using a 635 nm diode laser as the light source. The incidence angle was incremented by 0.05° steps, over a range of 3.35° around the resonance angle of 38°. Figure 3-2 shows the reflected intensity versus the relative angle of incidence, where median intensity values are plotted. The median values were produces from seven readings at each angle of incidence.

Using a silver ($\varepsilon_m = -16.54 + i1.30$) grating CD and $\lambda_0 = 670$ nm, the predicted SPR angle is approximately 37°. Even though the SPR angle is similar between gold and silver grating surfaces, the advantage of using silver is its narrower SPR dip. The advantage of gold is its chemical stability, which makes it more practical as a biosensor substrate. Therefore, gold grating CD-Rs were used for the experimental work. A 670 nm single mode diode laser was utilised instead of the

common 632.8 nm HeNe laser or the 635 nm diode laser, as longer wavelengths offer a sharper and deeper SPR profile.

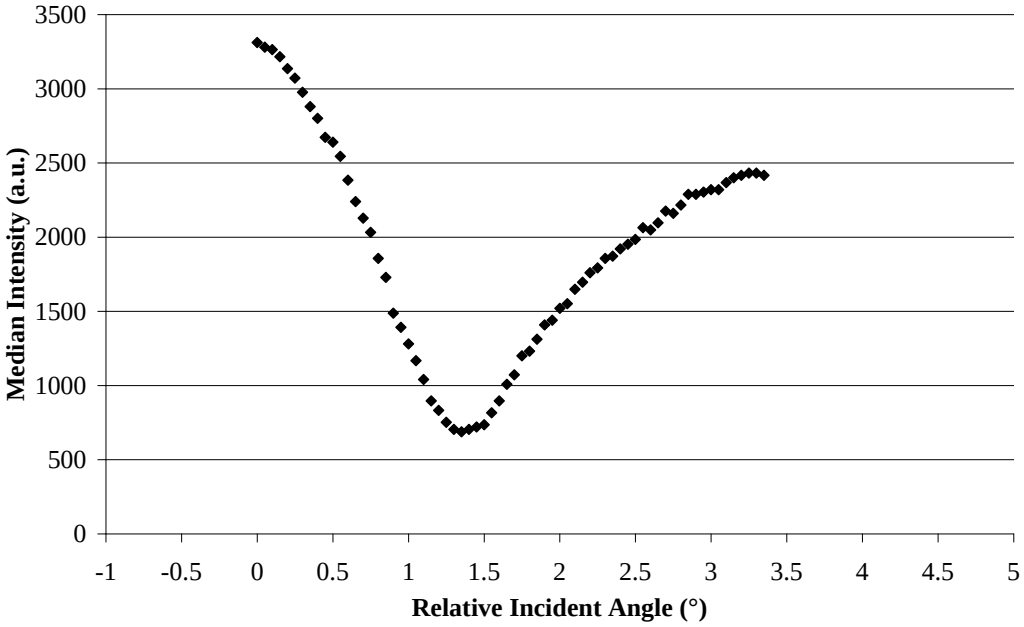

Figure 3-2. Intensity interrogation technique acquired SPR profile of the gold grating CD-R, illuminated with a 635 nm diode laser. The incidence angle was incremented by 0.05 ° steps, 3.35 ° around the resonance angle of 38 °.

3.3 Phase-polarisation contrast method

At surface plasmon resonance, it has been shown that electromagnetic wave phase changes much more abruptly than the intensity as the refractive index or thickness of a binding layer on the surface changes (Kochergin et al. 1998). A number of methods have been used for monitoring the excitation of SPR by measuring the phase change from the sensor interface (Nikitin et al. 1999; Nikitin et al. 2000; Shen et al. 1998).

Using phase-polarisation contrast (PPC) at non-optimum SPR coupling conditions lowers the resonant minimum of the reflected intensity close to zero.

Kabashin et al. (1998) introduced a phase-polarisation contrast technique to a prism-coupled SPR platform that gave a drastic increase in contrast by a minor modification of the optics.

The PPC effect is achieved with the introduction of a phase compensator and a polariser into the optical scheme of an angle interrogation SPR setup. In the most basic form, the PPC technique requires a pair of quarter-wave-plates and polarisers placed in front and behind the sensor.

With an appropriate orientation for each of the fast-axes of the quarter-wave-plates, the residual p-polarised wave, which has been strongly absorbed by the SPR substrate/sensor, is redistributed equally into each of the two elliptically polarised output waves, optimising the response curve and sensitivity (Wu and Pao 2004).

When the incidence angle goes through resonance, the reflected *p*-component changes its intensity and phase dramatically while the *s*-component remains unaffected (Abeles 1976). The difference between the *p*- and *s*-amplitude dependencies leads to a variation of the reflected light polarisation with the angle. The PPC technique transforms the contrast in polarisation into that of intensity. The contrast of the SPR dip is enhanced by the abrupt changes in the *p*-phase relative to the *s*-phase (Nikitin et al. 1997). Thus, the PPC unites the approaches similar to the methods of polarisation contrast and phase contrast.

3.4 CD SPR platform

A measurement platform was developed for SPR analysis that is capable of scanning the entire gold grating surface of a Compact Disk, viewing a small portion at a time. Using the platform a very large number of samples or analytes can be examined.

The experimental setup is shown in Figure 3-3. The apparatus consists of a 3 mW, 670 nm laser diode module (194-004, RS Components, New Zealand), a beam expander, two quarter-wave plates (QWP), two polarisers and two lenses. The SPR readout was performed with a high resolution (1360 x 1024 pixels), 12 bit, PixelFly CCD camera connected to a PC, where the raw SPR data was analysed using a MATLAB program. The instrument is shown in Figure 3-4.

A laser diode in conjunction with a beam expander was used for substrate illumination. The elliptical polarisation of the incident light was varied by the first QWP, while the intensity of the linear polarisation was adjusted by the first polariser. The second QWP and polariser were used for the implementation of the PPC technique.

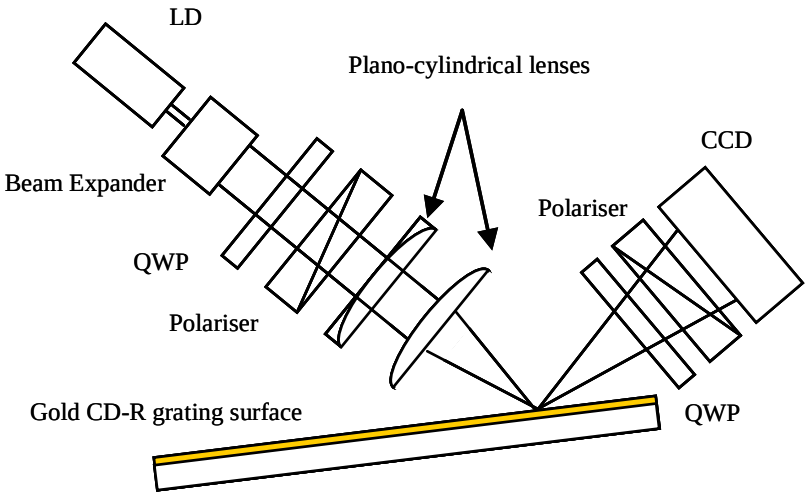

Figure 3-3. Experimental setup of the SPR analysis platform consisting of a (LD) laser diode, a beam expander, (QWP) quarter-wave-plates, polarisers, plano-cylindrical lenses, a CD-R grating substrate and a (CCD) charge coupled detector.

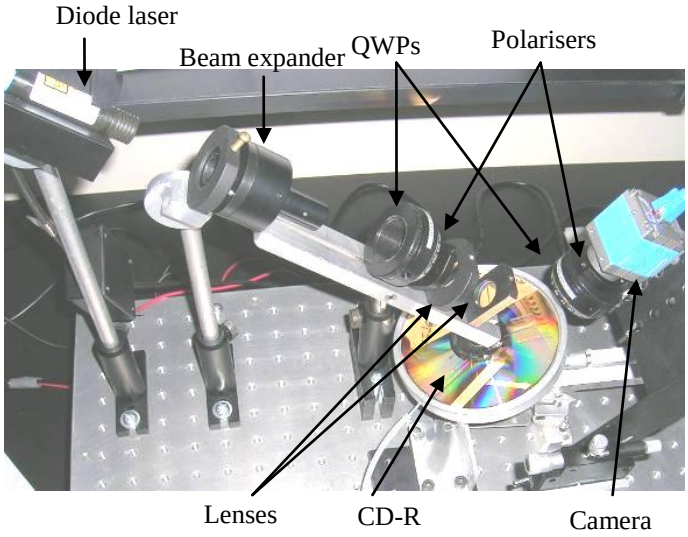

Figure 3-4. The CD-R SPR analysis platform, with a gold CD-R.

Two crossed (orthogonally orientated) plano-cylindrical lenses were used in the setup. The focus of the second lens closest to the substrate was aligned onto the CD-R gold grating surface. This converts the incident beam into a horizontal line (along the disk surface) at the focus, which provides a fan of incident angles. The first lens, orientated perpendicular to the second one, was aligned to focus the beam just prior to the substrate surface, providing beam widening in the horizontal direction. This magnifies the horizontal image resolution.

The analysis platform can control the beam's central incident angle, rotational translation, and radial translation. A notable difference to previous work is the use of the entire CD-R surface, rather than cut-up fragments. The platform allows for linear SPR array imaging and the ability to scan a large number of samples over a full CD-R.

The gold grating surface area of the CD-R is approximately 0.037 m^2. If a single sample is 4 mm^2 with centres 3 mm apart, it takes up 6.25 mm^2. With the SPR platform setup to scan the outer most 10 mm of the CD radius, it has the capacity

of 1,000 samples. In theory, just fewer than 6,000 sample locations would be available on the entire surface of a single gold CD-R. The platform can examine a very large number of samples, while preserving the benefits of the angle interrogation techniques.

3.4.1 Preparation of the CD-R surface

Recordable compact disks (MAM-A Gold CD-R) were purchased from Inkjet Art Solutions (Salt Lake City, UT). The CD-Rs used in this work consist of sequential layers of polycarbonate, dye, gold, protective lacquer, and polymer coatings. The polycarbonate layer has a spiralling groove formed during the injection moulding process. A photosensitive dye is coated on top of the substrate. A thin (50-100 nm) layer of gold is sputtered on top of this dye followed by protective coatings of lacquer and a polymer to prevent the metal film from damage. The pitch of the groove of the gold CD-Rs is suitable to excite surface plasmons in air (Fontana 2004).

The preparation of the gold CD-Rs involved removing the protective polymer and lacquer layers on the top side of the gold layer via wet chemical treatment (Singh and Hillier 2006). An entire CD-R was immersed in concentrated nitric acid for 2.5 minutes. During this time, the CD-R was oscillated up and down encouraging circulation of the nitric acid over the surface. The protective polymer and lacquer layers delaminated to expose the gold grating, which was then washed several times with water and ethanol, and dried with a nitrogen stream. The polycarbonate and gold surfaces were not affected by this treatment.

For one set of experiments, polyvinyl alcohol (PVA) was chosen as an analyte because of its excellent film forming properties. This required well controlled narrow thin films to be produced on a single substrate. The laboratory spin coater (WS-400B-6NPP/LITE/8K, Laurell Technologies) had an angular acceleration that was too large for coating narrow thin films. The samples spread/widened. At

the beginning of the spin coating process the tangential acceleration was greater than the centrifugal acceleration, causing the liquid's surface tension to break down laterally prior to rupturing radially. This produced wide thin films.

For a setting of 3000 RPM, at minimum angular acceleration, the substrate was still accelerating too quickly. Therefore, a custom spin coater was designed that had gradual angular acceleration, so not to break the fluid's surface tension in the lateral direction. Samples were spin coated onto the disk surface with a custom designed device, based on a standard CD-Drive driven by a Philips ARM7 LPC2119 microprocessor. The software program of the spin coater is noted in Appendix A.

The second set of experiments was aimed at the SPR analysis of gases. A gas delivery system was designed using multiple capillary tubes, where CO_2 and He gases were analysed and compared to air at room temperature.

3.4.2 Phase-polarisation contrast configuration

The phase-polarisation contrast (PPC) technique was implemented in an incremental sequence, tracking and evaluating the signal improvements at each step. Five different configurations of QWPs and polarisers were analysed. The purpose was to determine the effectiveness of the PPC method. The raw images were analysed in ImageJ (public domain, Java-based image processing program developed at the National Institutes of Health, United States), where SPR intensity profiles were extracted. We investigated several optical setups from the most basic format of SPR analysis to the more advanced form which utilises the phase-polarsation contrast technique. The six configurations are listed below and describe the progression of the experimental work. The sequence of items illustrates their order in the optical setup. The reason for testing the 6 different configurations was that we wanted to confirm what improvements were made by the changes in the setup.

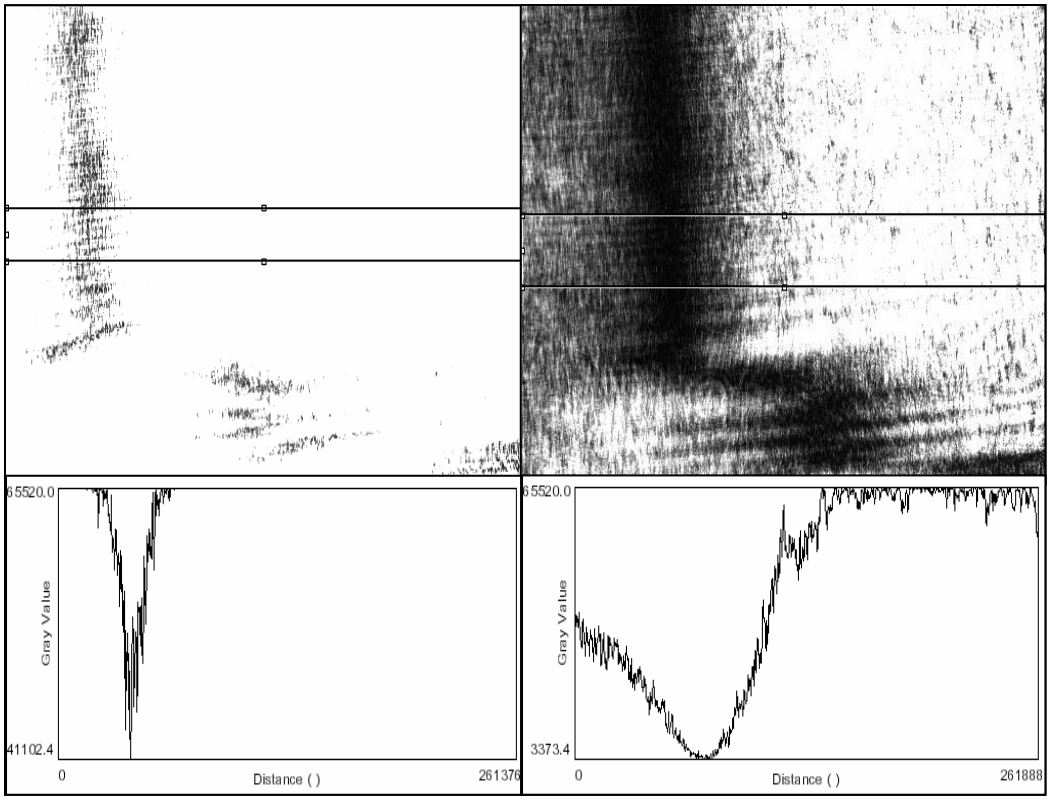

Figure 3-5. Experimental configurations (1) on the left and (6) on the right showing the SPR intensity profile at the camera exposure time of 15 milliseconds. In the images the grey level represents reflected light intensity; the x-axis represents the incidence angle of the reflected light, while the y-axis is the spatial location along the sensing line. The dark band is the low reflected light at the surface plasmon resonance angle. The plot below each image displays reflection intensity versus the angle of incidence for a region of the image selected within two parallel lines.

1. Grating, p-polariser
   exposure time of 15 ms – basic SPR configuration
2. Grating, 90° QWP, 45° polariser
   exposure time of 15 ms
3. 20° QWP, grating, 45°polariser
   exposure time of 15 ms
4. 10° polariser, grating, 8° QWP, 45°polariser
   exposure time (15 ms, 50 ms)

5. 10° polariser, grating, -8° QWP, 15° polariser
   exposure time (15 ms, 50 ms)
6. 60° QWP, 10° polariser, grating, -8° QWP, 15° polariser
   exp. time (15 ms, 50 ms, 100 ms, 150 ms) – full PPC configuration

As expected, the most significant difference in the SPR intensity was noticed between configurations (1) and (6). Figure 3-5, Figure 3-6 and Figure 3-7 are only for illustration purposes. The angular range is estimated to be 3.5°, while the lateral dimension is approximately 4 mm. Figure 3-5 shows SPR intensity profile of the two configurations for the camera exposure time of 15 milliseconds. The grey level represents the intensity of reflected light; the x-axis represents the incidence angle of the reflected light, while the y-axis is the spatial location along the sensing line. The dark band is the low reflected light, at the surface plasmon resonance angle. The plot below each image displays reflection intensity versus the angle of incidence, for a region of the image selected within two parallel lines.

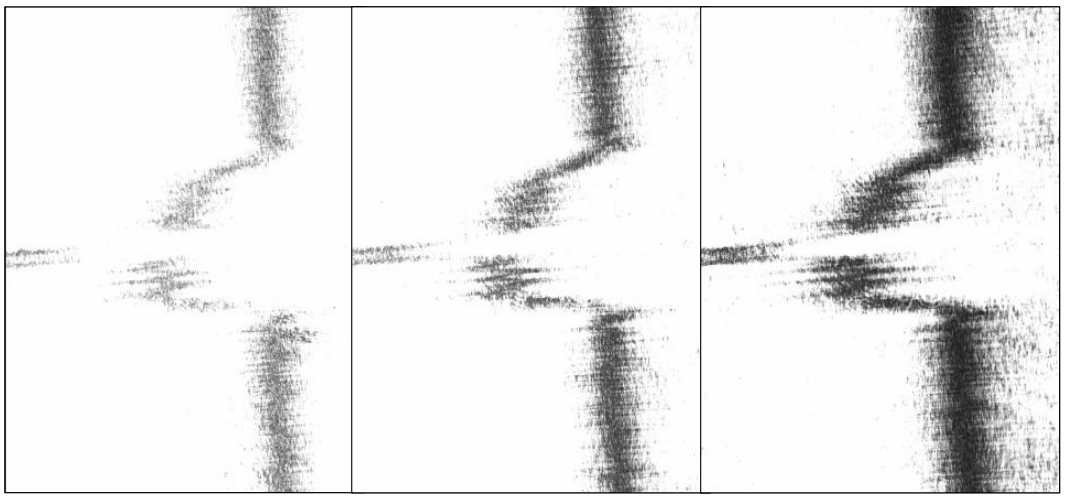

Figure 3-6. Experimental configurations (4), (5) and (6), shown from left to right, with camera exposure time of 50 ms. A noticeable deepening of the SPR minimum from (4) to (5) followed by a further improvement in (6). The variations in the SPR angle featured by dark bands in the middle are due to different PVA film depositions over the substrate grating. The grey level represents the intensity of reflected light in arbitrary units (A.U.). The x-axis represents the incidence angle of the reflected light in A.U., while the y-axis is the spatial location along the sensing line in A.U.. The dark band is the low reflected light at the resonance angle.

Simple configuration (1) was used as a base measure for SPR intensity to provide indication of relative performance enhancements for changes in the optical setup. In Figure 3-5, for configuration (6), the typical SPR profile is clearly distinguishable.

Due to large variation in SPR intensity between optical configurations, the camera exposure time was increased to 50 ms, to include all the results within its dynamic range. Figure 3-6 shows the images of the changes in the raw SPR intensity versus angle, for configurations (4), (5) and (6), from left to right respectively. An incremental improvement in SPR intensity depth (contrast) is noticeable from setup (4) through to (6), where the full PPC configuration is been implemented.

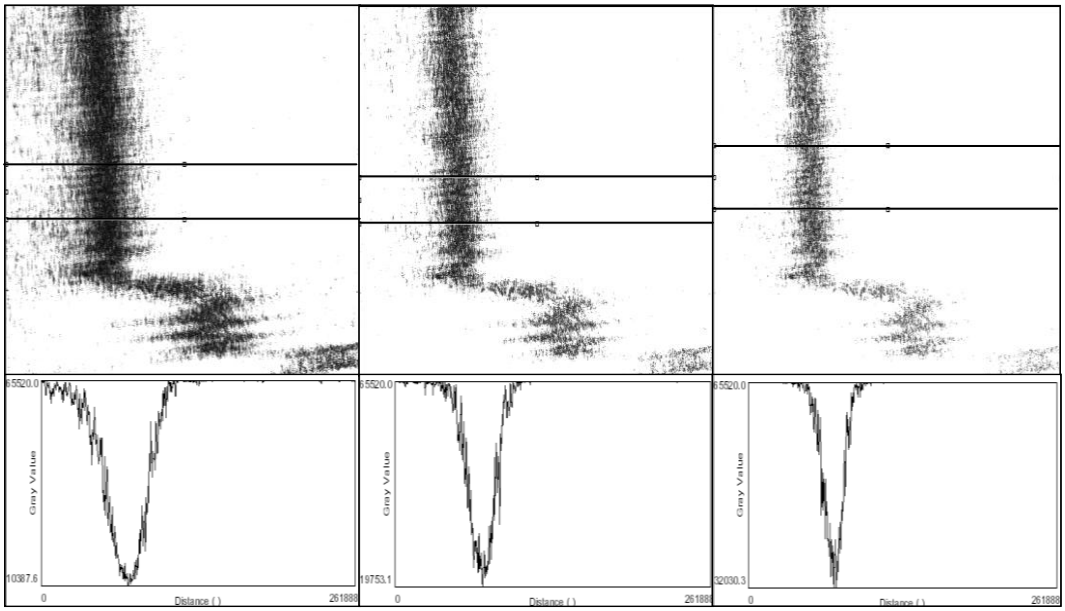

Figure 3-7. Raw SPR images and cross section intensity profiles for experimental configuration (6) with camera exposure times of 50 ms, 100 ms and 150 ms, from left to right respectively. The variations in the SPR angle featured by dark bands in the middle are due to different PVA film depositions over the substrate grating. In the images the grey level represents the intensity level of reflected light in A.U.; the x-axis represents the incidence angle of the reflected light in A.U., while the y-axis is the spatial location along the sensing line in A.U.. The dark band is the low reflected light at the resonance angle. The plot below each image displays reflection intensity versus the angle of incidence for a region of the image selected within two parallel lines.

Based on the images and plots for (6), exposure time of 50 ms seems to be the appropriate configuration, as the SPR dip profile is more strongly defined, enhancing the contrast. Configuration (6) has only 5% less p-polarised incident light than setup (1), while the SPR dip dropped 14 fold to an approximated 3.5% reflection.

Due to the significant decrease in the SPR minima, even higher camera exposure times may be considered. Figure 3-7 shows raw SPR images and cross section intensity profiles using PPC configuration with exposure times of 50 ms, 100 ms and 150 ms. The exposure time of 50 ms produces a narrow, well defined profile of the SPR minimum.

3.5 SPR raw image data processing

The readout of the surface plasmon resonance platform was performed with a high resolution (1360 x 1024 pixel), 12 bit, charge coupled detector (CCD), (PixelFly, The Cooke Corporation, Germany) connected to a PC. The raw image data was processed using MATLAB Image Processing Toolbox. The MATLAB file used for processing the SPR profiles is located in the Appendix B.

Prior to analysis images were de-speckled using ImageJ software and rotation corrected using MATLAB, to compensate for the hardware alignment. Then, separate horizontal and vertical Gaussian filters were applied. This helped to minimise speckle, background noise, and instrumentation and readout noise. The main instrumentation noise was caused by the quality and alignment of the laser diode and lenses, which can compromise the readout sensitivity.

Gaussian filtering was used along the CCD's vertical dimension (angular readout range) to mildly smooth out the SPR response profile. This was followed by

another Gaussian filter to provide a gentle smoothing along the horizontal dimension.

The post filter processing involved a 4th order polynomial fit, along the SPR angular dynamic range, to each of the 1,200 cross-sectional lines that constitute an SPR image. To fit the 4th order polynomial the domain values for the polyfit() function needed to be defined. These were located by finding the minimum and maximum intensity values. The maximum intensity value closest to the minimum intensity was used in defining the preliminary domain values.

The generated polynomial was evaluated using the polyval() function with a domain of 10 times higher resolution than the raw data. This refinement eliminated data pixel discretization by effectively redefining the SPR curves to a higher, sub-pixel angular resolution. The individual SPR response position and curve profiles were recorded and displayed.

The following section presents the experimental demonstration of the surface plasmon resonance analysis platform with deposited polyvinyl alcohol films on the bare gold CD-R surface.

3.6 SPR analysis of PVA films

A set of experiments were carried out, to perform SPR analyses for different refractive index values, using PVA thin film coatings on the gold grating CD-R surface.

Initial spin coating of the CD-R surface has shown that the film thickness has been deposited unevenly along the disk radius. The two raw images of Figure 3-8 clearly demonstrate the increasing layer thickness with radius. The SPR angle (dark band) increases relative to the baseline (right portion) of the clean disk

grating in air. Image (a) was taken 20 mm from the outer edge, while image (b) was taken 6 mm from the outer edge of the CD-R.

Because of the spin coating process (different tangential acceleration at different radii) the PVA film had an increasing thickness profile towards the outer radius. The outer 10 mm of the disk radius were used in the experimental work with different PVA concentrations.

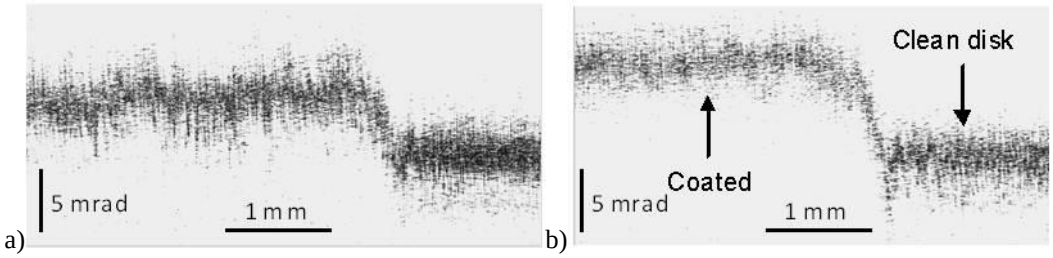

Figure 3-8. Raw SPR images. The x-axis represents lateral position and y-axis the reflected fan of angles. a) Middle CD radius; b) Outer CD radius. The grey level represents the intensity of reflected light. The x-axis is the spatial location along the sensing line, spanning 4.5 mm, while the y-axis represents the incidence angle of the reflected light. The dark band is the low reflected light at the surface plasmon resonance angle.

3.6.1 Experimental results

Two sets of experiments with different PVA concentrations were carried out, in the range from 0 % weight/volume (w/v) to 0.25 % w/v in water. The radial strips of PVA dilutions were spin coated onto the gold grating surface and analysed, Figure 3-9. The SPR measurements were acquired at the same radial position, while different samples were selected through rotation of the disk. The Figure 3-9 shows good consistency of the results from both experiments, with two outliers, at 0.15 and 0.20 % w/v. The trend line was calculated using data points from both sets.

The error bars for the y-axis illustrate only the SPR readout error of the thin film profiles. More significant errors are causes by the PVA deposition along with the edge effect of the film. The readout error from thin films is influenced by the variation in the deposited volume and inner radial point of deposition in the spin coating process. Another variation to the refractive index of the film may be due to the PVA's tendency to absorb water, changing the SPR responses due to the surrounding humidity.

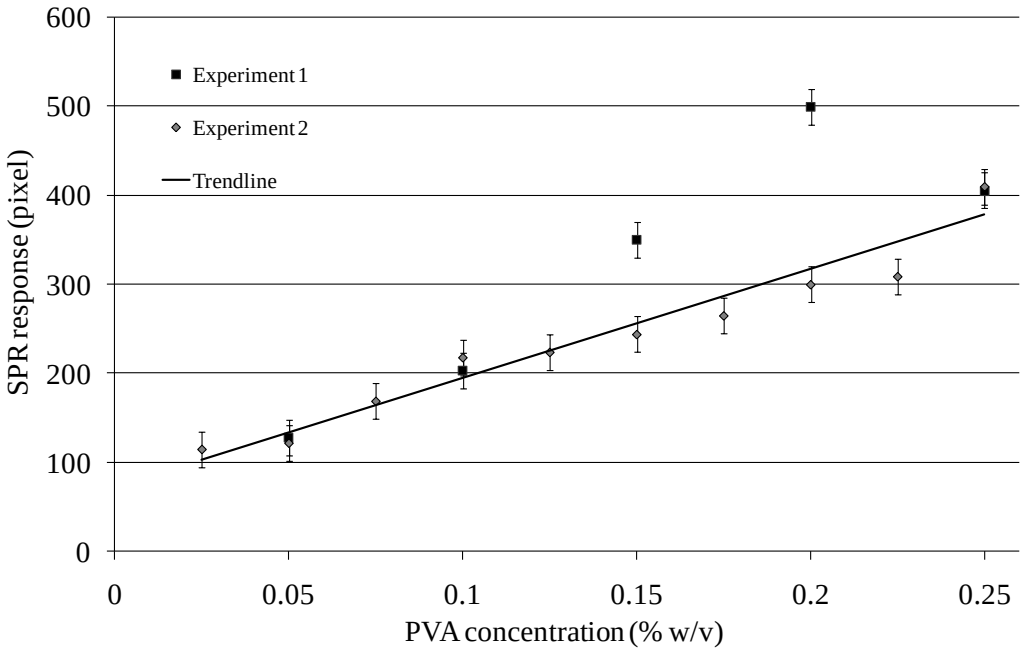

Figure 3-9. Relative SPR response versus PVA concentration results for two sets of experiments.

For each of the thin films, the effective refractive index was calculated using Eq. 2-1 and Eq. 2-2, where, for the SPR condition, the change in incident angle θ_0 relates to change in the refractive index n_D. The permittivity of gold was taken as $\varepsilon_m = -11.84 + i1.36$ (Singh and Hillier 2006). The film thicknesses could then be estimated from the known refractive index of PVA ($n_{PVA} = 1.521$).

The relative SPR shift versus PVA concentration was calculated for the second experiment. The SPR shift is related to the film thickness. The results are shown in Table 3-1 and plotted in Figure 3-10.

Table 3-1. SPR response and estimated film thickness at various PVA concentrations

PVA concentration (% w/v)	Relative SPR (°)	n_eff (RIU)	Estimated thickness (nm)
0	0	1.000292	0
0.025	0.36	1.004617	1.6
0.05	0.38	1.004856	1.7
0.075	0.53	1.006645	2.4
0.1	0.68	1.008433	3.1
0.125	0.70	1.008673	3.2
0.15	0.77	1.009505	3.5
0.175	0.83	1.010218	3.8
0.2	0.94	1.011522	4.3
0.225	0.97	1.011878	4.4
0.25	1.29	1.015657	5.9

The overall SPR active response distance extends as far as 200 nm into the dielectric for wavelengths above 630 nm and is exponentially decaying with penetration depth (Homola et al. 1999b). However, the measured PVA film thicknesses are in the range from 1 nm to 6 nm. Therefore, the thin films are in the linear region of the SPR response profile. This results in the linear relationship between the SPR response related and the PVA concentration.

The ability of the SPR analysis platform to scan over the CD-R surface was used to acquire lateral film profiles. The SPR response profile of the 0.175 % w/v PVA thin film strip is shown in Figure 3-11. The strip consists of snapshots taken as the disk was rotated. The individual snapshots were analysed and overlaid to form a continuous strip. The x-axis is the spatial location along the sensing line, while the y-axis represents the surface plasmon resonance angle in arbitrary units. A single

raw snapshot image prior to image processing is shown in Figure 3-12. This corresponds to the highlighted boxed part of Figure 3-11.

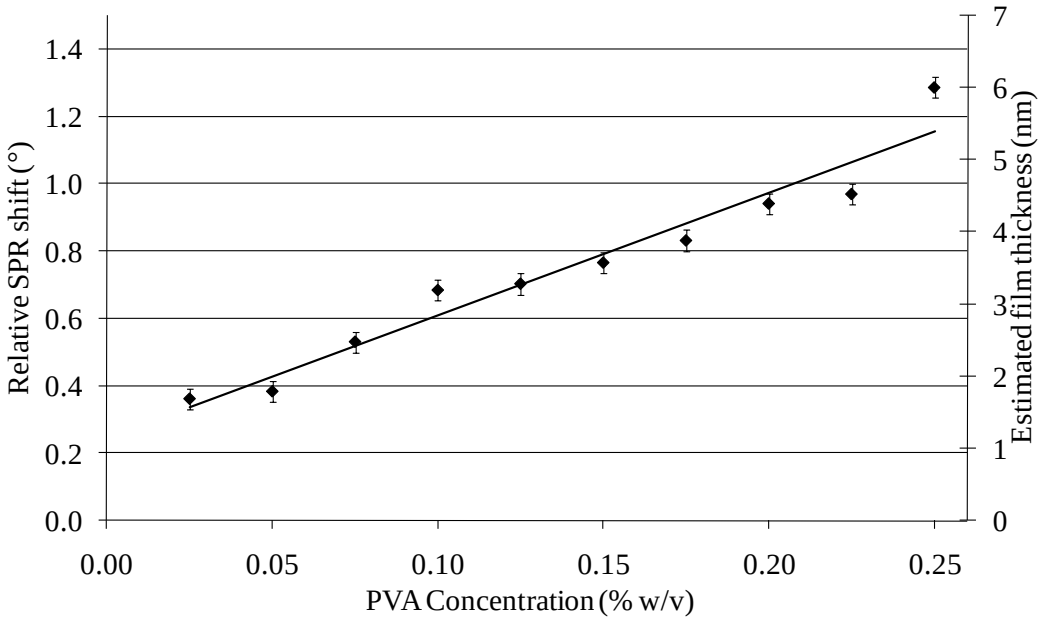

Figure 3-10. Experimental results and a linear trend line of the SPR shift for different PVA concentration. The second y-axis presents the estimated film thickness which is related to the SPR response.

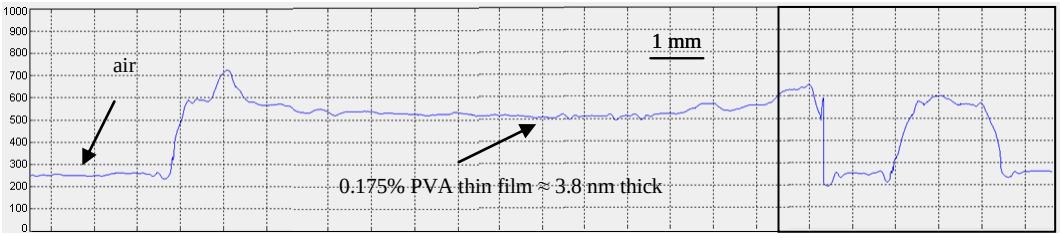

Figure 3-11. SPR profile of the thin film cross-sectional strip for a 0.175 % PVA concentration. The boxed right portion of the film strip corresponds to the raw snapshot image shown in Figure 3-12. The x-axis is the spatial location along the sensing line, while the y-axis represents the surface plasmon resonance angle, in arbitrary units. The angle change of 250 a.u. corresponds to the SPR shift of 0.7°.

The experiments show that we can observe the individual thin film's lateral SPR profiles along with the linear SPR response for different film thicknesses. The platform can also be used for the observation of changes to the PVA refractive index properties, which might occur due to the environmental conditions such as humidity.

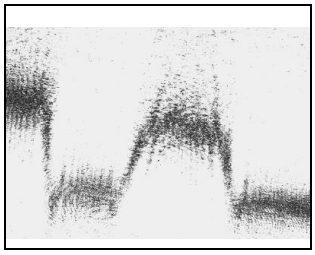

Figure 3-12. Raw snapshot image of the SPR response corresponding to the highlighted box in Figure 3-11. The colour intensity represents level of reflected light. The x-axis is the spatial location along the sensing line, while the y-axis represents the incidence angle of the reflected light. The dark band is the low reflected light at the surface plasmon resonance angle.

Using the current configuration, the strip analysis reveals the thin film lateral profile, where the edge effects are clearly visible. The film is approximately 12 mm wide, while the middle section of the 0.175 % w/v PVA film is estimated to be 3.8 nm thick. Figure 3-11 shows that the thin film SPR profile does not exhibit variations due to surface grating, as over 12 mm there are around 8,000 grooves. It is the effective SPR profile of those grooves that is measured.

Atomic force microscopy analysis

Atomic force microscopy (AFM) was used for analysing the PVA thin films on the disk surface. The AFM confirmed a grating structure with a period of 1560 nm. Figure 3-13 shows the bare grating surface on the left side and the PVA thin film formed from 0.125 % w/v concentration on the right.

The film thickness is greater in the grooves than at the top, due to the spin coating process. The first five films of least PVA concentration have thickness of less than 5 nm on top of the grooves and less than 10 nm inside the grooves, while the remaining films seem to be around 5 nm on top of the grooves and 20 nm inside the grooves. These AFM results closely coincide with the expected range of film thicknesses, verifying the SPR measurements.

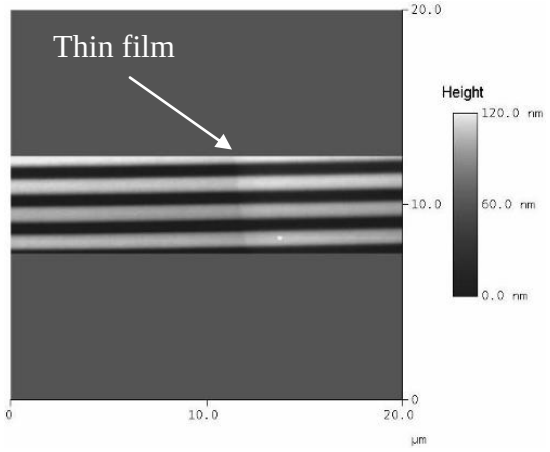

Figure 3-13. Atomic force microscope image of exposed gold layer on the left and the spin coated thin film of 0.125 % PVA concentration on the right portion of the image.

The following section presents the experimental demonstration of the SPR analysis platform in detecting small changes in refractive index using differential analysis of He and CO_2 gases relative to air.

3.7 SPR analysis of gases

A set of experiments was aimed at the SPR analysis of gases, where CO_2 and He gases were analysed and compared to air at room temperature. A gas delivery system was designed using multiple capillary tubes with an outer diameter of 360 µm and the inner diameter of 250 µm. CO_2 gas has 1.000449 refractive index units (RIU) at the wavelength of 589.3 nm and temperature of 0°C while He gas has 1.000035 RIU. These gases were analysed and compared to air (1.000292

RIU). Differential analyses of the SPR responses were performed for greater resolution of the signal and noise levels. Air was used as a base line, reference signal.

3.7.1 Experimental results

The initial experiments looked at the SPR response for CO_2 and He gases relative to air. The plot of the resulting refractive index difference is shown in Figure 3-14. A capillary tube outlet for streaming the gases was located in the middle of the SPR image view.

The measured difference between air and CO_2 was 120×10^{-6} RIU, and between air and He was -220×10^{-6} RIU, with an experimental uncertainty of $\pm 20 \times 10^{-6}$ RIU. The small difference between the expected and the measured values could be due to the diffusion and mixing of gasses with the surrounding air, changes due to temperature, and the fluctuations in the baseline reading.

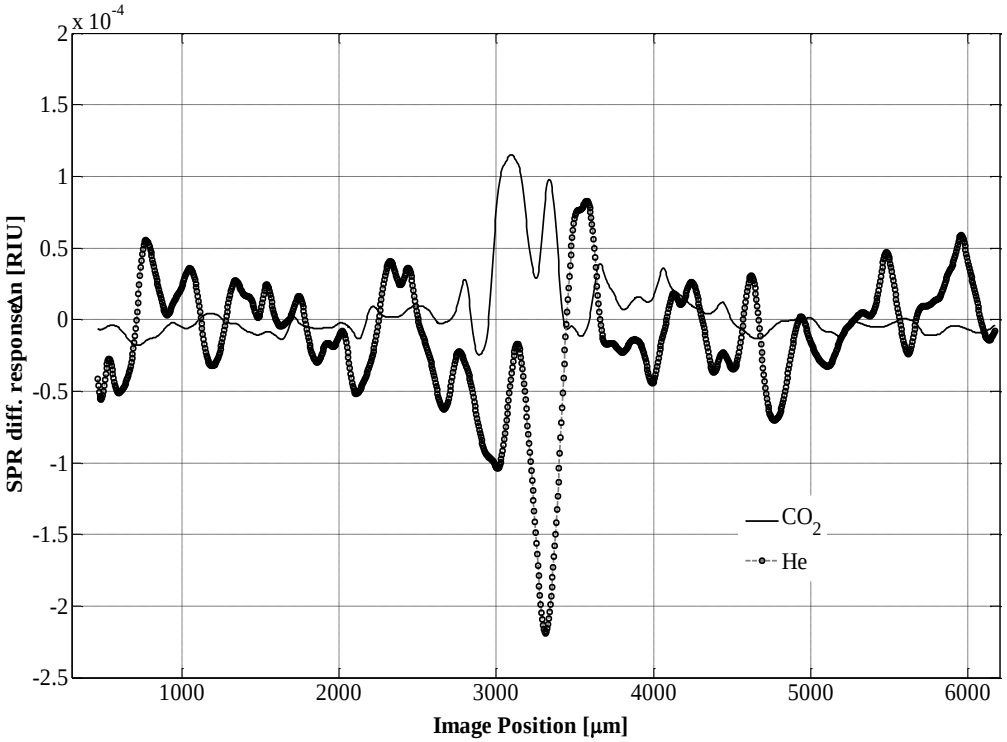

Figure 3-14. SPR responses for CO_2 and He gases relative to air.

An array of capillary tubes was made which released the gases closer to the sampling surface and allowed also multiple gas flows. To acquire a cleaner SPR response of the CO_2 gas, the gas stream was switched, allowing or preventing the flow. Difference of these sequentially acquired raw SPR images was analysed to give an improved CO_2 profile. This further optimisation achieved a better response profile and reduced noise. Figure 3-15 shows a difference of raw SPR images of the CO_2 and air SPR responses.

The raw SPR images are prior to any automated image processing and alignment correction which precedes the extraction of the SPR information. The portion of the raw difference image, shown in Figure 3-15, laterally spans over 5 mm, while the fan of reflected angles is ~1.5° wide.

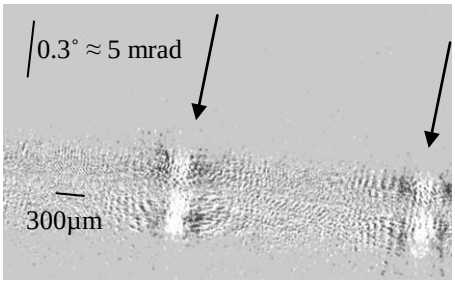

Figure 3-15. Part of the raw difference image of CO_2 relative to air SPR responses. Arrows show the location of gas flow. The x-axis is the spatial location along the sensing line, while the y-axis represents the incidence angle of the reflected light.

A positive difference in the SPR response between the images is shown as two white bands surrounded by dark strips, while a negative difference would be seen as a dark band surrounded by white strips. These points are the locations where the capillary tubes release the flow of CO_2 gas.

The subsequent SPR analysis of the modified configuration shows a clearer response profile, Figure 3-16. The SPR analysis revealed that the experimental

results, a shift of 160 × 10^{-6} RIU, closely matched the predicted value of 157 × 10^{-6} RIU. A small portion of the right-sided CO_2 stream is seen from the multiple capillary tubes.

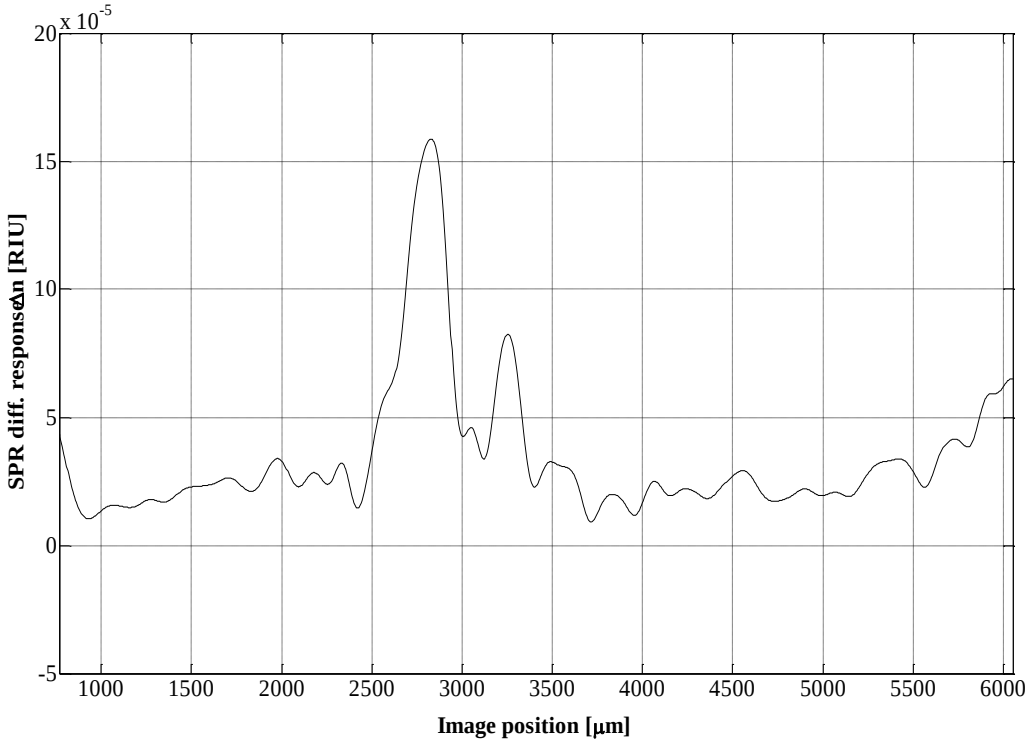

Figure 3-16. The SPR shift of CO_2 stream relative to air.

Another important observation was that along with the SPR response shift, there was a change in the minimum intensity and the SPR curve width. All of these are indicators of the variation in the refractive index as shown by the experimental SPR curves in Figure 3-17.

The noise level for the differential style analysis is below 50 × 10^{-6} RIU. By increasing the flow width (sample width), currently less than 400 μm, the noise levels would be further minimised through averaging.

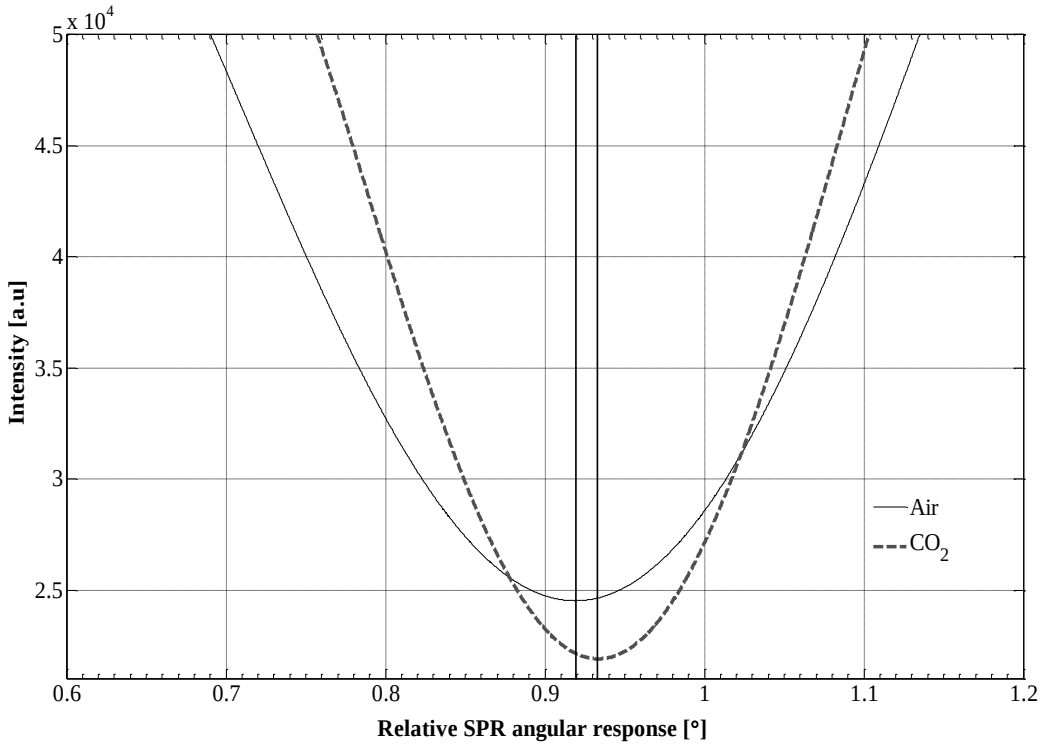

Figure 3-17. SPR curve of CO_2 and air.

3.8 Discussion and implications

We have devised a surface plasmon resonance analysis platform which utilises gold grating compact disks as the sensing substrate. These experiments proved the concept and capabilities of the technique. The measurement method allows high resolution analysis of gases and surface chemistry, and is capable of analysing a large number of samples by scanning over the entire surface of the gold grating recordable compact disk.

The inherently non-optimum coupling conditions of a gold grating CD-R was compensated with the phase-polarisation contrast technique. It was implemented on the analysis platform improving the measurement resolution by lowering the reflected resonant minimum under surface plasmon coupling conditions. The PPC scheme resulted in the deepening of the intensity minimum down to

approximately 3.5% reflection and the enhancement of the contrast by up to 14 times compared to the results without the PPC implementation.

Two sets of validation experiments were performed using spin coated PVA thin films and different gasses. This provided a form of testing and demonstrating the performance of the SPR analysis platform. The experimentation was designed so to mimic biological responses using physical characteristics. As with any grating based SPR system, the sample was required to be optically transparent, as the incident light passes through the medium being analysed.

Using PVA thin films, it was demonstrated that a linear array of samples can be examined, while preserving the benefits of SPR angular interrogation techniques. Therefore, using the SPR analysis platform, the entire gold grating CD-R surface is read by controlling the beam incident angle, disk rotation, and radial translation. A very large number of samples can be examined, permitting an extensive number of reference samples for improved precision.

For gasses, differential analyses of the SPR responses were performed so to gain greater resolution of the signal and noise levels. Air was used as a base line reference signal. The differential SPR analysis of gases revealed that the experimental results closely matched the expected SPR shift values. Another important observation was that the SPR response shift was accompanied by a change in the minimum intensity and the SPR curve width, where both are indicators of refractive index variation.

A difference to previous work by Singh and Hillier (2006) and Fontana (2004) is the implementation of the PPC technique and the use of the entire CD-R surface, rather than cut-up fragments. Therefore, the platform allows for SPR array imaging and the ability to scan over the entire disk surface. Furthermore, the platform offers a significantly improved sensing performance by combining SPR angular interrogation with the PPC technique.

A noteworthy limitation to this approach of SPR imaging was the grating curvature throughout the CD-R. The study has resolved this by linearly scanning throughout the entire surface.

3.8.1 Limitations of the study and future research

A number of potential improvements are recommended, and may be implemented as future work on the design of the CD-R surface plasmon resonance analysis platform.

As with any grating based SPR system, the sample was required to be optically transparent, as the incident light passes through the medium being analysed. The enhancement due to the PPC technique was limited by the quality of the polarisers and the residual light scatter.

As suggested by Singh and Hillier (2006) the CD-R substrates should be cleaned in oxygen plasma for one minute to remove any residual organic impurities, improving the sensing resolution, and sensitivity. This was not performed as we did not have access to oxygen plasma.

The SPR profile resolution of the platform may be further increased by narrowing the incidence fan angle range. Therefore, using a lens with longer focal length, a smaller incidence fan angle range would be spread over the entire CCD camera surface. This would produce a much higher resolution at the trade-off to dynamic range.

Even though the surface plasmon resonance angle is similar between gold and silver grating surfaces of the same period the advantage of implementing silver is the inherently sharper SPR dip with a narrower resonance profile. The advantage of gold is its chemical stability, which makes it more practical as a biosensor

substrate. Therefore, the use of a silver grating disk (MAM-A Silver CD-R) within the presented SPR analysis platform may offer improved precision through a sharper surface plasmon resonance dip.

A suggestion for an improvement to the current processing of acquired SPR data is to include image distortion correction into the image processing program. The image distortion results from non-ideal lenses. This would minimise the possible deviation between the result readout in the centre of the image to those at the edges.

Using the presented approach, a very large number of samples may be analysed. The grating surface area of the CD-R is approximately 0.037 m^2. For 4 mm^2 samples centred 3 mm apart, the outer most 10 mm of the CD-R surface permits the capacity of 1,000 samples to be scanned, while in theory, just fewer than 6,000 such sample locations are available on the entire disk. By reducing the focal length of the first plano-cylindrical lens the horizontal magnification would increase. By increasing horizontal image resolution, smaller sample sizes can be analysed, leading to a greater number of sample sites.

3.9 Summary

The phase-polarisation contrast technique was implemented within the SPR analysis platform due to its signal enhancement in non-optimum SPR coupling conditions. It improved the measurement resolution by lowering the resonant minimum intensity. The platform's ability to scan over the disk surface, by rotation, permits a thin film profiling such as formation and topography.

Using spin coated PVA thin films, it was demonstrated that the platform can be used for examining a linear array of samples, while preserving the benefits of SPR angular interrogation techniques. Therefore, using the SPR analysis platform, the entire gold grating CD-R surface is sampled by controlling the beam incident

angle, rotational translation, and radial linear translation. This allowed a very large number of samples to be examined over the entire disk surface, permitting an extensive number of reference samples for improved precision.

Differential analyses of SPR responses were also performed to gain greater resolution of the signal and noise levels. The differential SPR analysis of gases revealed that the experimental results closely matched the expected SPR shift values.

The platform offers significantly improved sensing performance by combining SPR angular interrogation with the PPC technique. This work is an incremental step towards taking the large scale SPR analyses to a lower cost, desktop format. Based on the results presented, it is feasible that the technique could be implemented for a number of biological and physical applications where screening of very large number of samples may be beneficial.

The following chapter describes the far-field transmission instrument designed for acquiring spatially resolved transmission spectrum of single nanoholes.

Chapter 4

4 FAR-FIELD, SPATIALLY RESOLVED TRANSMISSION OF SINGLE NANOHOLES

Modern nanofabrication techniques, such as electron beam lithography and ion beam milling are used in custom designing material surface wave dynamics by structuring the surface at the subwavelength scale. The increasing use of scanning near-field optical microscopy and interest in the enhanced transmission phenomenon has stimulated experimental (Degiron et al. 2004; Yin et al. 2004) studies, the results of which challenge Bethe's predictions. In particular, it has become possible to measure the transmission and diffraction from a single subwavelength aperture in a metallic film at optical wavelengths (Degiron et al. 2004; Yin et al. 2004). Degiron et al. also demonstrated that the spectrum becomes sensitive to the incident light polarisation for geometries such as rectangular nanohole. This chapter describes the far-field transmission instrument designed for acquiring spatially resolved single nanohole transmission spectra by scanning over the nanohole array surface.

4.1 Introduction

A range of geometries have been modelled and characterised, such as nanohole arrays (Ebbesen et al. 1998; Chang et al. 2005), slit with corrugations (Lezec et al. 2002; Garcia-Vidal et al. 2003), and apertures with annular corrugations (Lezec et al. 2002) with varying dimensions. There have been a number of approaches to analysing these subwavelength structures and their optical behaviour, with considerably less emphasis on monitoring single nano-scale structures. A dominant approach to characterising single nano-scale geometries has been the use of near-field techniques such as scanning near-field optical microscopy.

Of particular interest to this research is the analysis of single nano-scale geometries, such as a single nanohole in an array or single surface plasmon antennae, using far-field measurements of the transmission spectrum. Such access to individual nanostructures as single sensing units permits the design of sensor array platforms, e.g. nanohole arrays.

4.2 Apparatus

A far-field transmission instrument was designed for acquiring spatially resolved single nanohole transmission spectrum by scanning over the nanohole array surface.

In the instrument, Figure 4-1, the sample was illuminated by a Halogen lamp (Avantes AvaLight-Hal-S, Phillips, Netherlands) through a 400 µm fibre with numerical aperture (N.A.) of 0.22 (divergence angle of 25 degrees). The surface plasmons show angular dependence to incident light as demonstrated by Ebbesen et al. (1998). The zero-order transmission spectra changed even for very small angles as shown by recording the spectra every 2°. The peaks changed in intensity and split into new peaks which moved in opposite direction. This is the exact behaviour observed when light couples with surface plasmons in reflection gratings (Homola et al. 1999a; Vukusic et al. 1992). If the angle of incidence is varied, the incident radiation excites different surface plasmon modes. Therefore, to excite the plasmons of the lower modes one needs to illuminate the sample with a collimated beam. However, for a collimated white light source, the beam intensity is not high enough to be measured at the single nano-hole scale. Consequently, there needs to be a way to increase the beam intensity without too greatly deviating from a collimated beam.

Three different illumination approaches were analysed and their transmission spectra compared. The light source that is closer to collimated should excite a smaller number of plasmon modes, resulting in sharper, well defined transmission

spectrum. Amongst a number of illumination schemes a bare fibre and a 40X objective lens were used.

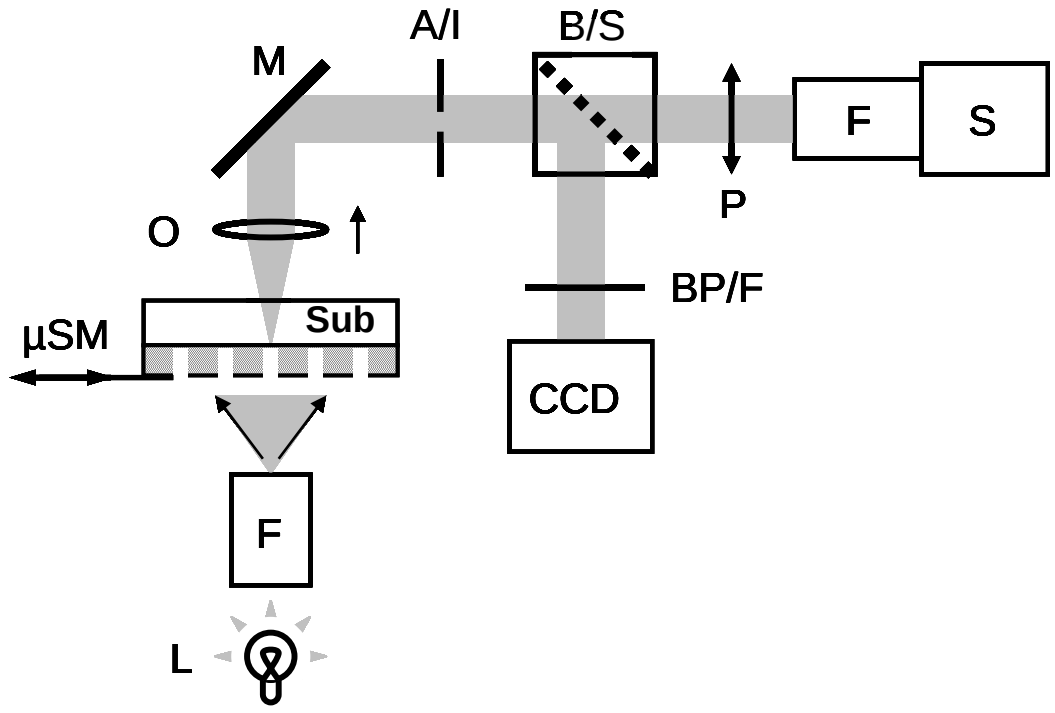

Figure 4-1. Far-field instrument for measuring transmission spectrum of single nanostructures. Halogen lamp light source (L); illumination and collection fibres (F); micro stepper motor (µSM) supporting a nanostructured substrate (Sub); objective lens (O); mirror (M); adjustable iris (A/I); beam splitter (B/S); bandpass filter (BP/F); CCD camera (CCD); polarising element (P); linear CCD spectrometer (S).

The 400 µm fibre with N.A. of 0.22 has the critical angle of 12.7° which gives an acceptance angle of 25.4°. The 40X objective lens with N.A. of 0.65 has a critical angle of 40.5˚, with acceptance angle of 81°, which is able to excite a wide number of plasmon modes. Therefore, the normalised transmission spectrum of the 40X objective lens lacks the number of spectral features, due to the averaging of all the excited plasmon modes that may have been spectrally as well as intensity altered. Based on this information, a 400 µm fibre with N.A. of 0.22 was

selected for substrate illumination, exciting the least number of plamon modes and offering more spectral features.

The transmitted light is collected with a 100X objective lens (MUE20900, Nikon, Japan) with extra long working distance and extended near-infra-red (NIR) transmission and then guided through an optical path of ~1 m to the charge coupled detector (CCD) spectrometer (USB2000, Ocean Optics, Dunedin, Fl, USA). The CCD spectrometer has a 1.4 nm spectral resolution.

The setup benefits from the high transmission performance in the visible and NIR spectrum of the objective lens, and from its practical benefit of extra long working distance. The long optical path length further magnifies the image. Prior to the spectrometer, the 420X magnified image is passed through a beam splitter, where a portion of the light is redirected through a 488 nm (±10 nm) bandpass filter and imaged with the 12 bit CCD camera (PixelFly, The Cooke Corporation, Germany). The other portion of light illuminates the 200 μm (N.A. of 0.22) fibre plane. By having removed the long wavelengths, the inspection with the CCD camera allows easier sharpening of the images and better focusing onto the collection fibre's plane.

The setup permits the spectral analysis of the signal transmitted from a 480 nm diameter spot. This resolution was confirmed by an experiment where the aperture was slowly moved past a knife edge, and the intensity change from black to white was measured. The travel of the aperture was accomplished using a micro-stepper motor (ZST13, Thorlabs Inc.). This result compares reasonably well with the calculated resolution of 450 nm, determined from the system's magnification and the acceptance aperture of the spectrometer.

A photodiode array (PDA) spectrometer from Zeiss and the charge coupled detector (CCD) spectrometer from Ocean Optics Inc., Dunedin, Fl, USA were compared. The CCD spectrometer was set-up for transmission spectrum analysis

as the PDA spectrometer was found to have inadequate sensitivity. The PDA spectrometer required ~3000 photon-electron conversions per count, while the CCD spectrometer required only ~30 photon-electron conversions per count. Due to the significantly higher sensitivity, the shot noise in the CCD based instrument is more noticeable. However, this choice resulted in integration time reduction of 100 times, faster spectrum acquisition and data averaging, offering improved sample characterisation.

Sub-micrometer movements of the substrate in one dimension were achieved using the micro-stepper motor (ZST13, Thorlabs Inc.). Therefore, the sample surface (nanohole array) is characterised by scanning across with an effective 480 nm probe with 50 nm minimum step size.

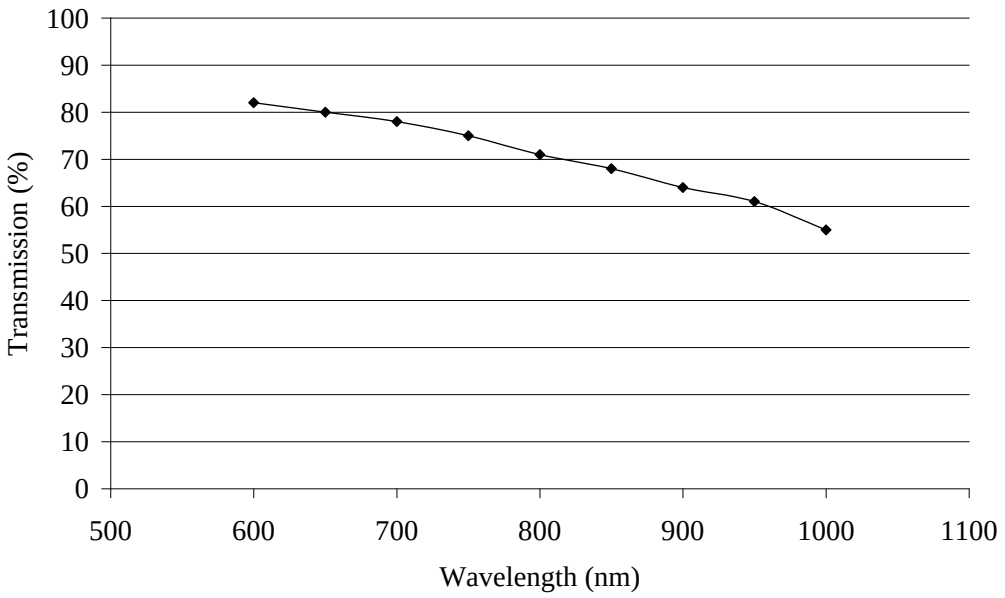

Figure 4-2. Transmission spectrum of the 100X Nikon MUE20900 objective lens (Matsuura 2007)

The 100X objective lens was used in the setups for characterising individual nanoholes in nanohole arrays and selective polaritons generator structures. The numerical aperture of the objective lens is 0.8. The transmission spectrum of the

objective lens is shown in Figure 4-2. The extended NIR performance was essential for correctly characterising selective polariton generator structures throughout their intended practical spectrum.

4.3 Characterisation of results

A number of gold and silver nanohole array substrates were analysed with various periodicities from 520 nm to 1500 nm, where Figure 4-3 shows spectral transmission profiles of the gold substrates. The Figure 4-4 shows a spectral profile of a 1500 nm period gold (Au) nanohole array. The two transmission profiles represent measurements over the aperture and between the nanoholes respectively.

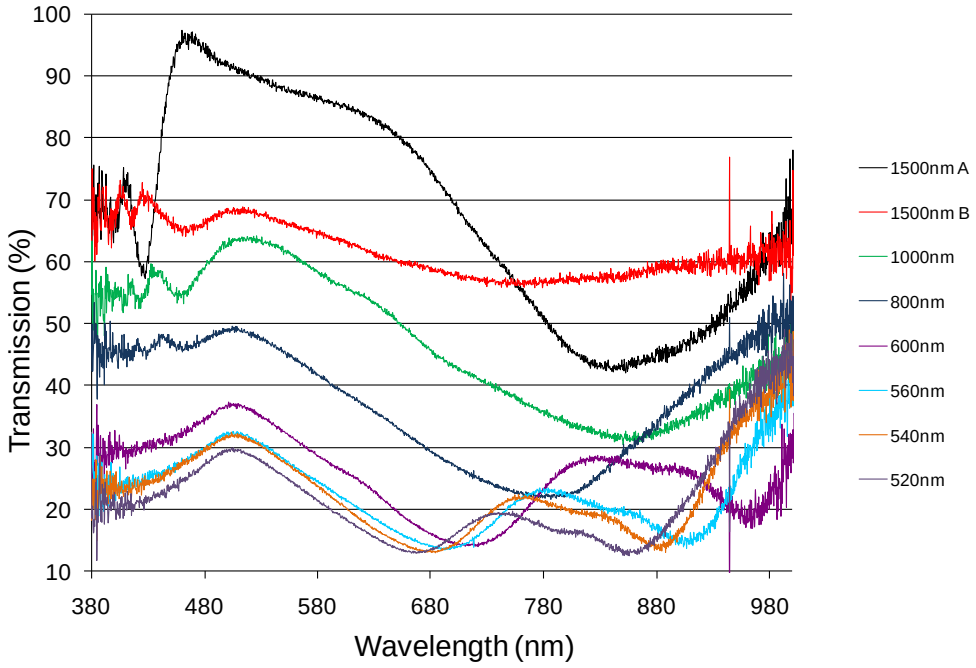

Figure 4-3. Spectral transmission profiles of the Au nanohole arrays with periodicities ranging from 520 nm to 1500 nm, and 50 nm film thickness.

The two transmission images shown in Figure 4-5 are from the 800 nm period Au nanohole array. In the left image a defect is visible, confirming that the images are

of the nanohole structure and not an interference pattern. The individual nanoholes are imaged with a camera through the 488 nm (±10 nm) bandpass filter. The image resolution is diffraction limited and cannot have sharper features as the nanoholes are 200 nm in diameter.

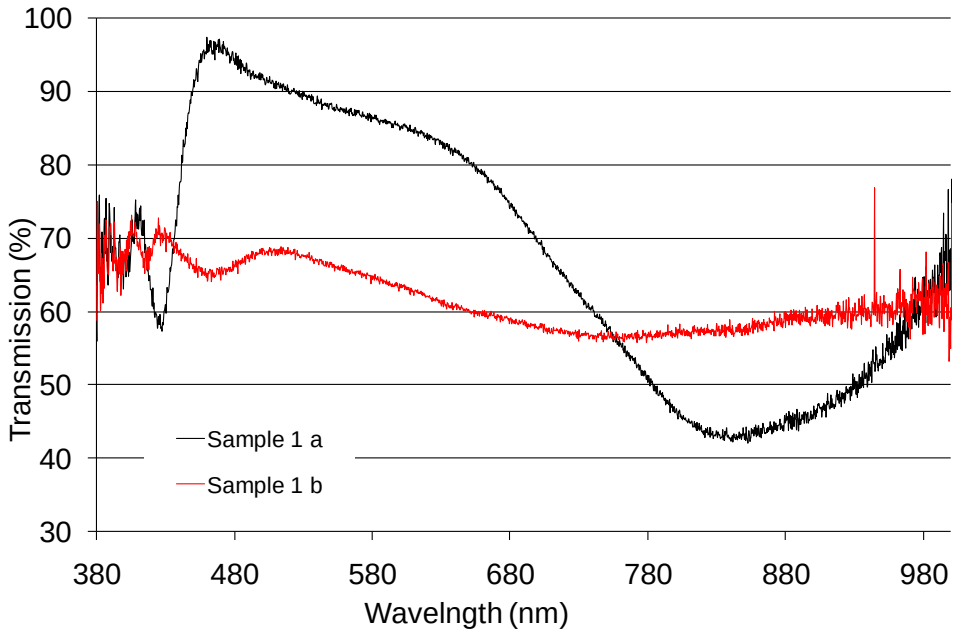

Figure 4-4. Spectral profile of the Au nanohole array of 1500 nm period, and 50 nm film thickness. The black line is the transmission profile measured over the aperture, while the red line is the transmission profile taken between the nanoholes.

The 800 nm period Au nanohole array was spectrally scanned. The spectral contour plot is shown in Figure 4-6. Using the micro-stepper motor, the substrate spectra were captured at 100 nm spatial intervals. Figure 4-6 shows the transmission spectrum from 377 nm to 950 nm. The 30 contours range from 0% to 37% transmission, the maximum recorded transmission intensity. The colour illustrates the percentage of transmission.

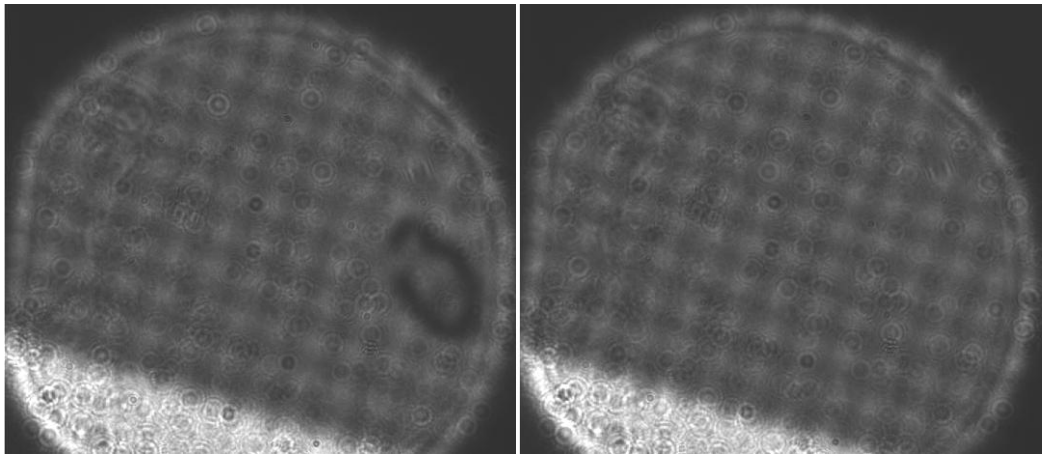

Figure 4-5. Transmission images of the Au nanohole array of 800 nm period, 200 nm nanohole diameter and 50 nm film thickness.

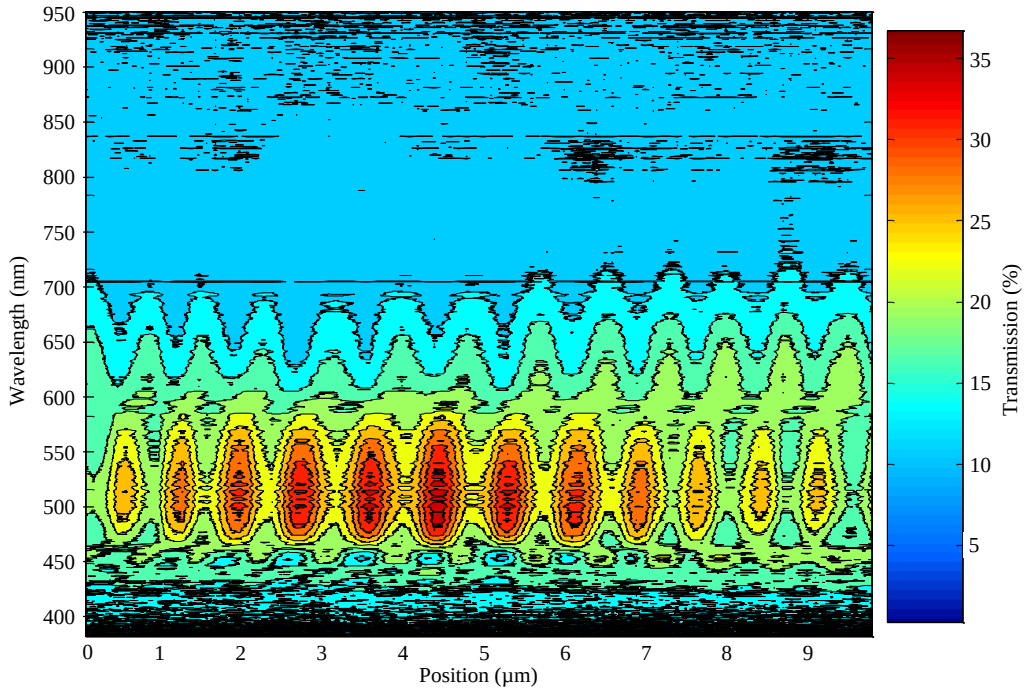

Figure 4-6. Spectral contour plot of the Au nanohole array with the 800 nm period.

Twelve nanohole features are seen, confirming the nanohole period of approximately 800 nm. The primary contour features are around 520 nm which closely matches the expected location of the primary transmission peak.

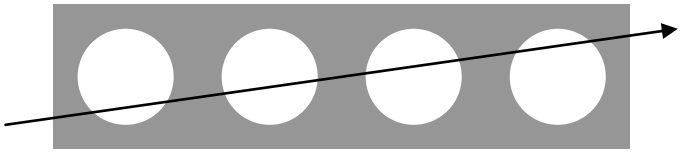

Figure 4-7. Imperfectly aligned scanning path over the nanohole array.

As the scanning axis was not perfectly aligned with the nanohole array axis, the substrate was scanned slightly diagonally across the nanoholes' axis, Figure 4-7. The variation in the maximum transmission signal across the holes can be explained by the alignment of the scanning probe, being located near the edge of the nanohole and propagating across the middle of the nanohole, as it moves over the substrate. The four transmission spectra features positioned between 2.5 μm and 5.5 μm are the nanohole centres.

4.4 Discussion and implications

We have designed a far-field transmission instrument for acquiring spatially resolved single nanohole transmission spectrum by scanning over the nanohole array surface. We have shown that our instrument can produce spectral characteristics of single holes. Such access to individual nanostructures as single sensing units enables the design of large scale sensor array platforms, e.g. nanohole arrays where each aperture is a sensor.

The experimental results have demonstrated the system's capability to acquire and distinguish spectral features associated with individual nanoholes and the edge effects by scanning throughout the nanohole array. More importantly, the transition of spectral characteristics may be monitored, as the probe travels over each hole.

A potential application for individual nanostructure analyses arises in arrays of where individual structures may be treated as individual sensors. Therefore a large

number of analytes can be tested on a single substrate. Another advantage of such an approach is the small sample volume for a very large number of analyte sites (Levene et al. 2003; Rigneault et al. 2005).

We now apply a modified version of the instrument to more structures. In Chapter 5 it is utilised for characterising behaviour of various nano-scale geometries with polarisation and wavelength dependent transmission. The research may be applied to the analysis of any single nano-scale geometries, such as surface plasmon antennae or polarisation susceptible rectangular nanoholes.

Chapter 5

5 POLARISATION AND WAVELENGTH SELECTIVE POLARITON GENERATOR

Excitation and localisation of surface plasmon polariton modes in metal-dielectric structures can be utilised to construct nanophotonic materials and devices with tuneable optical dispersion. Recently, surface plasmon antenna consisting of a nanohole surrounded by circular corrugations has been demonstrated which channel/transmit incident light of a specific wavelength range. This chapter presents selective polariton generator devices that demonstrate wavelength and polarisation selective light transmission, based on surface plasmon antennae principles. Here we report on our investigation into various design aspects of the surface plasmon polariton structures with specific polarisation and wavelength selectivity. The structures have been modelled for optical transmission, gated switching, and polarisation selective properties. Section 5.2 describes the methodology of modelling, designing, and fabricating the selective polariton generator structures, along with the instrumentation used for characterising their spectral responses. Section 5.3 discusses the work on single surface plasmon generator structures and the establishment of polarisation selective behaviour, while, section 5.4 discusses the work on multi-state surface plasmon generator structures which offer multiple polarisation and wavelength selective behaviour.

5.1 Introduction

There are a number of surface plasmon antenna designs that range from deposited nanoparticle chains to plain and circular grating configurations. The understanding and interaction of light with nano-geometries on metal-dielectric interfaces has led to a development of unique nanophotonic materials and devices

with tuneable optical scattering and transmission, constructed using the excitation and localisation of surface plasmon polariton (SPP) modes (Barnes et al. 2003).

A number of groups extensively researched and characterised the properties of circular surface plasmon antennae (Shuford et al. 2006; Hofmann et al. 2007), a central nanohole surrounded by annular corrugations. Previous studies on circular surface plasmon structures have investigated the effects of variables such as corrugation period and depth (Shuford et al. 2006), while their susceptibility to incident light polarisation has received less attention.

As the grating structures contribute to the momentum of incident light, they can be designed so that the wavevector of the diffracted wave equals the wavevector of the surface plasmon wave. The matching of the incident light with surface plasmon waves is discussed in more detail in Section 1.2.2. Therefore, a single aperture encircled by periodic corrugations in the metal surface will also display surface plasmon enhanced transmission. The work in this thesis focuses on the structures consisting of a central nanohole surrounded by corrugations.

The following section describes the methodology of modelling, designing, and fabricating the selective polariton generator structures, along with the instrumentation used for characterising their spectral responses.

5.2 Materials and methods

A number of selective polariton generator (SPG) structures were designed, modelled, and fabricated, to show polarisation and wavelength selective transmission through the central nanohole. These were based on nanoholes flanked with different grating geometries. Each structure contains a central nanohole (through to the glass surface) of 300 nm in diameter, in a metal film. Corrugation periods of 570 nm to 730 nm were used to elicit specific and

distinguishable spectral transmission peaks. All experiments were carried out in air.

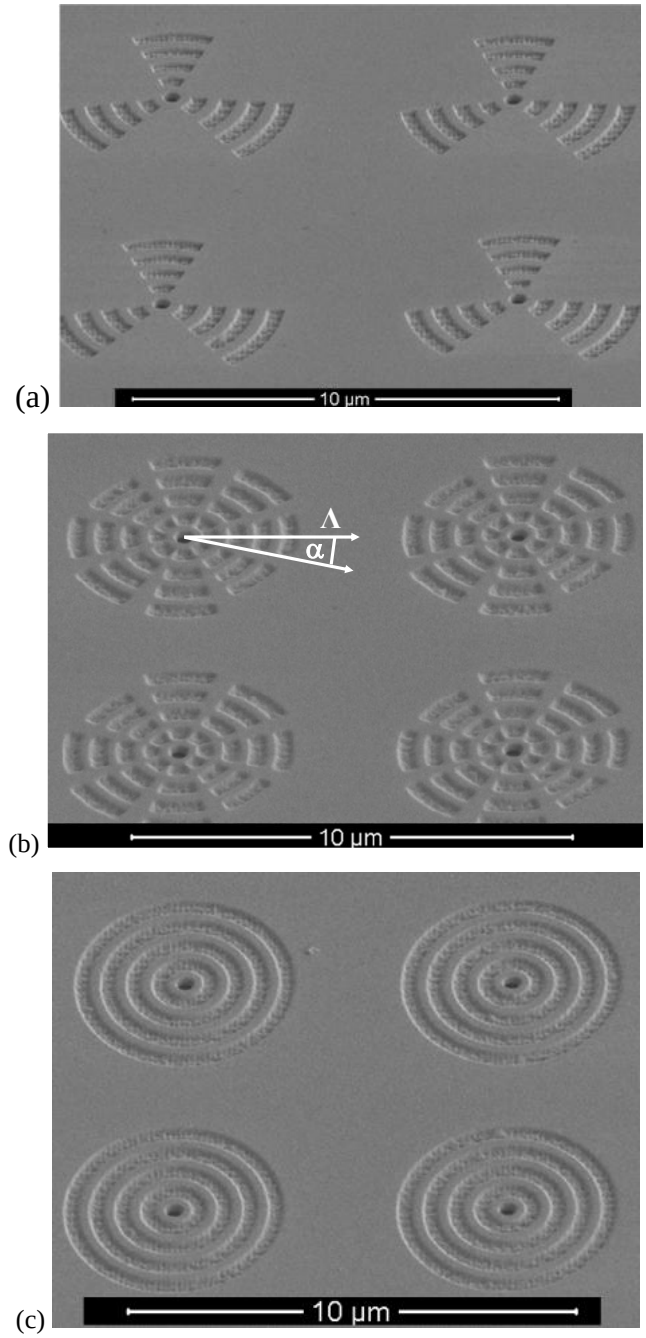

Figure 5-1. Polariton generators fabricated using FIB milling. Scanning electron microscope images taken at 52º to the substrate surface of, (a) semi-triple SPG structures (570 nm, 630 nm, 690 nm corrugation periods) (b) quad SPG structures (570 nm to 690 nm corrugation period), and (c) elliptical continuous SPG structures (570 nm to 690 nm corrugation period).

The edge to edge spacing between structures was set at 2 μm to minimise the potential for periodic plasmon interaction between devices and to enable individual SPG analysis. Simulations showed that neighbouring SPG structures affect the peak transmission intensity of a single structure by around 3%, which we consider insignificant. The corrugation depths were chosen to be around 80 – 90 nm (approximately 15% of the corrugation period) to yield optimal operation as determined by our simulations and as suggested by Shuford et al. (2006).

Ten different sets of structures were fabricated, from which seven sets were analysed for their spectral characteristics. These include: two sets of fully circular structures with single grating periods around the central nanohole; two sets with partially encircling single grating periods; four sets of partially encircling structures with multiple (2, 3 and 4) grating periods; and two sets with continuously varied grating periods, fully encircling the central nanohole.

The remaining three sets of structures were fabricated in case the similarly designed structures failed in the process, or were required to further characterise and understand their spectral characteristics. The structures are shown in Figure 5-1. The corrugation fan angle, α, is the extent of the corrugation rings around the circle. The corrugation axis, Λ, is the line that extends from the centre of the nanohole along the 0º of the corrugation fan angle.

5.2.1 Numerical modelling

Computational modelling plays a crucial role in the field of nanophotonic research, providing the means to characterise and customise a given structure or a system. In this research, numerical models of nanohole arrays, surface plasmon antennae, single and multi-state selective polariton generator structures have been designed in FDTD Solutions (Lumerical Solutions, Inc., Vancouver, Canada) software. Simulations were performed, prior to fabrication to ensure the designs exhibited desired characteristics.

FDTD Solutions uses finite-difference time-domain techniques to solve Maxwell's equations (Lumercial Solutions 2008). It addresses a wide variety of applications involving the scattering, diffraction, and propagation of optical radiation.

It is useful for many engineering problems including biophotonics, display technology, optical communications, optical sensing and imaging, and semiconductor manufacturing. Capabilities within the FDTD software environment include integrated optical sensors, light emitting diode optimisation, nanowire grid polarisers, digital micromirrors, ring resonators, optical waveguides, optical filters, photonic crystals, CMOS image sensor pixels, and DVD surface design (Lumercial Solutions 2008).

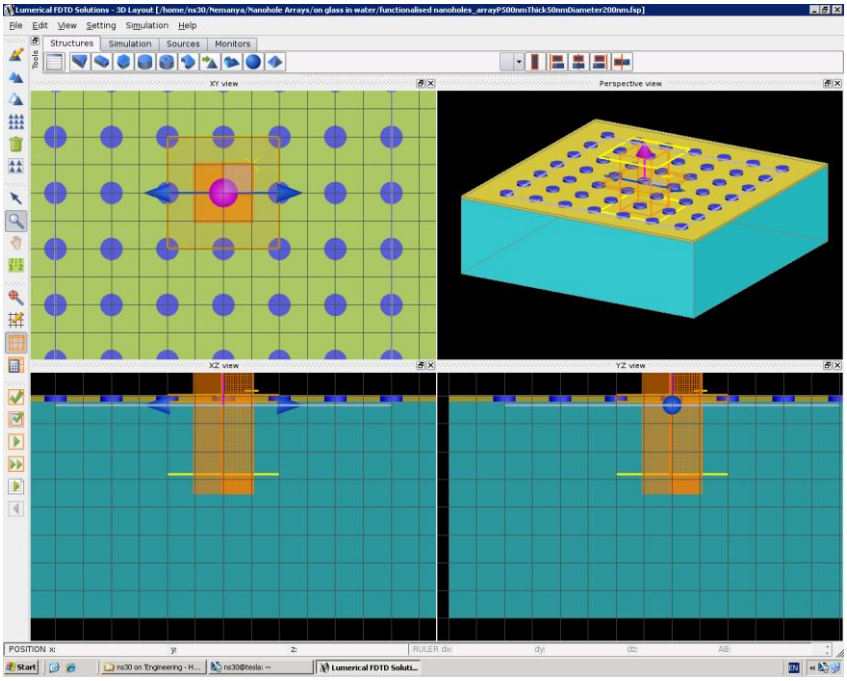

Figure 5-2. Screen shot from the FDTD Solutions of a nanohole array. The array has a 500 nm periodicity, 200 nm hole diameter and 50 nm gold thickness on glass substrate. The four individual frames depicted in the screen shot show (left to right, top to bottom), XY plane, Perspective view, XZ plane and YZ plane.

A noteworthy aspect of FDTD Solutions is its ability to perform parallel computation on multiple cores, multiprocessors and clusters. This enables large-scale and rapid simulation of optical components, by distributing computational load and memory requirements. The package also offers an integrated scripting environment to customise simulation and analysis for design automation, and a movie generation feature for recording simulation field/intensity dynamics.

Figure 5-2 shows a screen shot of a nanohole array, while Figure 5-3 shows a screen shot of an orthogonally paired selective polariton generator structure. The script file for analysis of the finite-difference time-domain simulations, designed in FDTD Solutions, is located in Appendix D. The script calculates the transmission of the selective polariton structures for a 15 degrees cone and a full cone of transmission.

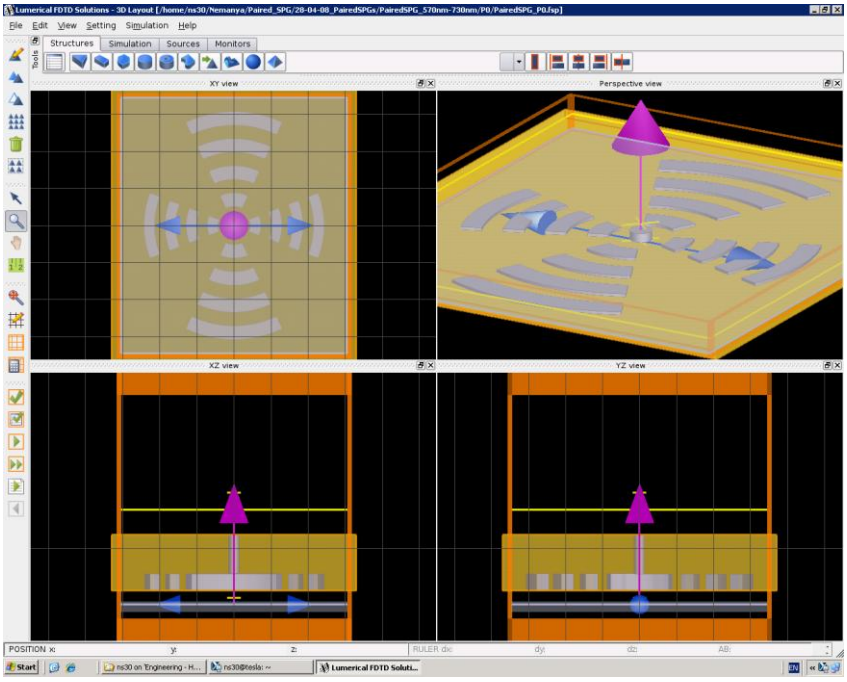

Figure 5-3. Screen shot from the FDTD Solutions of an orthogonally paired selective polariton generator with 570 nm and 730 nm period resonance corrugations in a 200 nm thick gold layer. The four individual frames depicted in the screen shot show (left to right, top to bottom), XY plane, Perspective view, XZ plane and YZ plane.

The simulation settings were:

- minimum mesh step 0.25 nm,
- maximum mesh step 10 nm,
- meshing refinement 5,
- auto non-uniform mesh type,
- boundary conditions – perfectly matched layers and
- default dielectric properties of Au.

The numerical model analysis considered three scenarios for the transmitted light analysis: a full collection cone of transmitted light, a 20º and a 15º cone of transmitted light. Except for the transmitted intensity, there are only minor differences between the resulting transmission spectra. All the simulated models presented in this chapter transmitted light with a collection cone of 15º. Version 5.1 of FDTD Solutions software was used for sections 5.3 and 5.4.1 and version 6.0 was used for section 5.4.3.

5.2.2 Design and fabrication

The structures were fabricated at Bio21 Institute in Melbourne, Australia. They were produced on gold-coated glass substrates (200 nm Au film on 4 nm Ti on 1 mm x 10 mm x 10 mm glass, SSENS, Netherlands). Focused ion beam (FIB) milling (Dual-beam xT Nova NanoLab, Ga ion source, 30 kV source) was used with a beam current of 100 pA.

The plasmonic structure designs were laid out in CorelDRAW X3 (Corel Corporation). The red, green and blue (RGB) colour scheme in the layout determined the ion beam milling specifications. Within the FIB milling software, the structure layout is imported as a 24 bits bitmap pattern. The imported pattern can be rescaled to any desired dimensions.

The Red component was currently not used. The Green component determines if the beam is on or off. Any other value than 0 activates the beam. The Blue component determines the dwell time per pixel, which is directly related to the ion milling depth. If blue is set to 0 the dwell time of a pixel is at the minimum of 100 ns. If blue is set to 255 the maximum dwell time is used. The dwell time for the pixels in between these values are linearly interpolated in 127 values. When drawing a bitmap it is recommended to use black (0,0,0) for non-milling points and blue for the milling points. The procedure for patterning a bitmap of nanostructures using focused ion beam milling is explained in Appendix E.

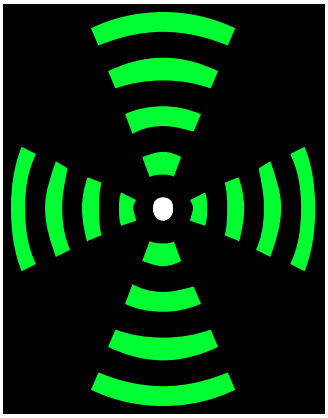

Figure 5-4. CorelDRAW X3 Graphic software layout design and the RGB colour scheme of an orthogonally paired selective polariton generator, plasmonic structure. The layout is scaled to the desired dimensions within the FIB milling software.

Figure 5-4 shows a CorelDRAW layout of a plasmonic structure, orthogonally paired selective polariton generator. The central through-hole had a dwell time set to maximum RGB (255,255,255) while dwell time for the corrugations was set to (0,255,50).

5.2.3 Spectral transmission analysis instrumentation

Spectral transmission analysis of substrates was performed using a purpose-built microscope (Figure 5-5), a setup similar to the instrument originally designed for individual nanohole analysis, discussed in section 4.2.

A magnified image of the structures was projected onto the charge coupled detector (CCD) camera (Pike F100B, Allied Vision Technologies, Stadtroda, Germany) to facilitate substrate alignment. The magnification of the setup provided individual element studies. Using a stage with a swivel the same magnified image was redirected onto a 400 µm core diameter optical fibre (0.12 NA) coupled to a CCD spectrometer (USB2000, Ocean Optics, Inc., Dunedin, FL).

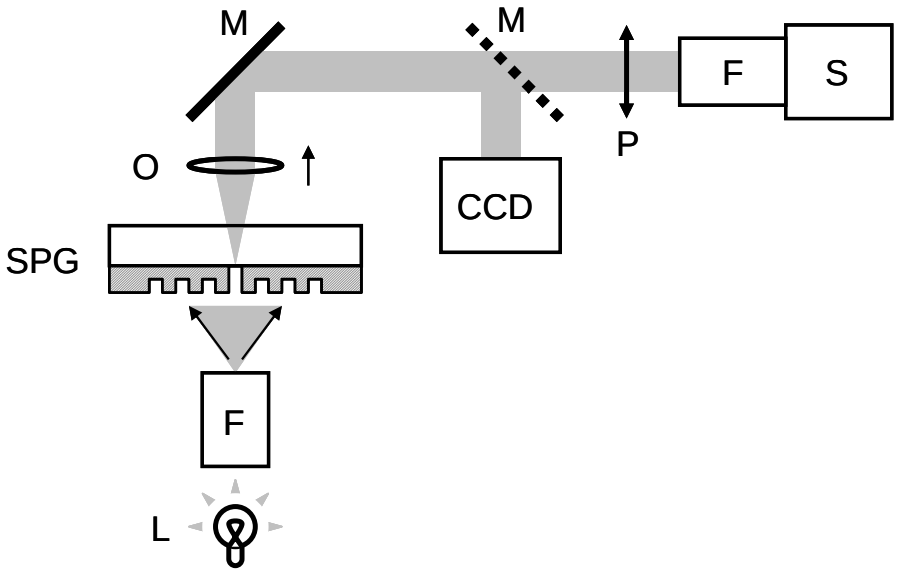

Figure 5-5. Experimental setup includes the light source (L), illumination and collection fibres (F), SPG substrate, objective lens (O), mirrors (M), CCD camera (CCD), polarisation element (P) and a linear CCD spectrometer (S).

The spectra were acquired for 5 seconds and averaged over three acquisitions. The acquired spectra were corrected for dark current and background light, and normalised to that of the halogen lamp.

A polarisation element was mounted on a rotation stage in the detection path to provide analyses at different polarisation angles. The hypothesis that there is no difference in the polarisation of incident light and the transmitted light of the structures was supported by models in FDTD Solutions software.

The following section discusses the work on single surface plasmon generator structures and the establishment of their polarisation selective behaviour.

5.3 Single surface plasmon generators

Single surface plasmon generator structures utilise partial or fully circular corrugations of only a single period, surrounding a single central nanohole. Here we discuss the fully circular structure, often referred to as surface plasmon antenna, and the partially encircled structure we call selective polariton generator (SPG).

Each of the selective polariton generator (SPG) structures consists of a photon antenna, which acts as a polariton generator, and a central nanohole for polariton tunnelling. The photon antenna is formed by corrugations on the metal film that may partially or fully encircle the nanohole. This grating provides the necessary momentum matching geometry for energy transfer from incident photons to the collective electron wave oscillation. The central nanohole facilitates the propagation of polaritons through to the opposite side of the metal film (Degiron et al. 2004; Chang et al. 2005). Corrugation period and depth determine the surface plasmon antenna's spectral transmission characteristics.

5.3.1 Circular surface plasmon antenna

Two circular surface plasmon (SP) antennae were fabricated as a reference for comparing our experimental results with theory (Lezec et al. 2002) and the finite-difference time-domain numerical models.

The corrugation periods of these two structures were 570 nm and 690 nm, while the corrugation depth was milled to approximately 80 – 90 nm. The central nanohole diameter was 300 nm, milled through the 200 nm Au film to the glass substrate. The scanning electron microscope image of the 570 nm circular surface plasmon antenna structures is shown in Figure 5-6.

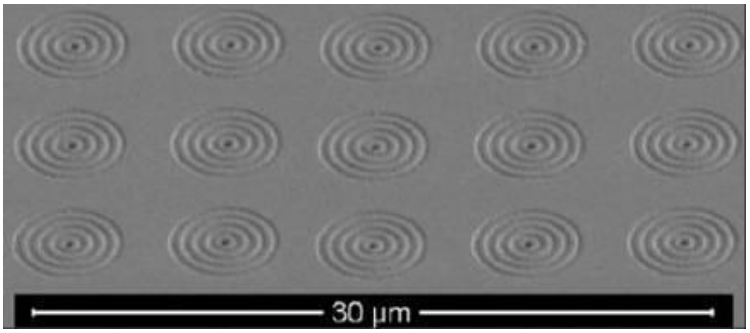

Figure 5-6. Scanning electron microscope image of an array of circular surface plasmon antennae fabricated using FIB milling. Image was taken at 52º to the substrate surface. The corrugation period of each structure is 570 nm.

The overlaid experimental and simulated transmission spectra are shown in Figure 5-7. For each corrugation period there is a corresponding peak transmission wavelength. This is due to the momentum matching condition of the grating for a particular wavelength.

For the antenna structure with the corrugation period of 570 nm, a peak transmission wavelength was measured at 674 nm, while the simulated model predicted 683 nm. For the structure with the corrugation period of 690 nm, a peak transmission wavelength was measured at 743 nm, while the simulated model

predicted 730 nm. There are only small spectral differences between the simulated and experimental results of the two circular surface plasmon antennae structures. These are the peak wavelength position (difference of 9 nm and -13 nm respectively) and the shape of the transmission curves. These could possibly be due to imperfections in the fabricated device and approximations in the modelling algorithm.

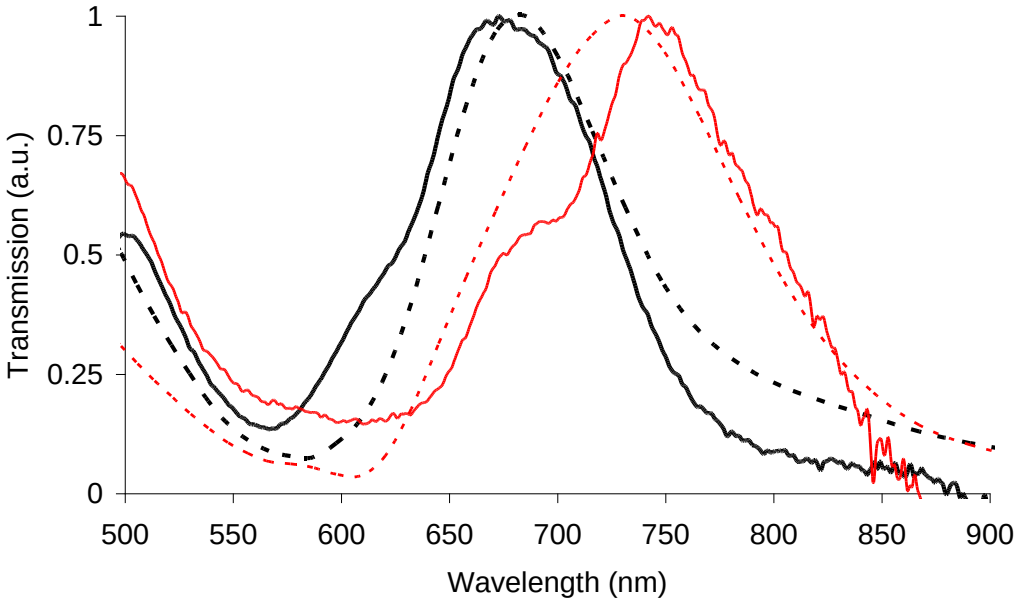

Figure 5-7. Overlay of transmission spectra for the two circular surface plasmon antennae with 570 nm (black: simulated - - -, experimental ─) and 690 nm (red: simulated ···, experimental ─) corrugation periods respectively.

There is agreement between theoretical simulations and experimental transmission curves for both structures. As expected, these substrates do not exhibit polarisation dependent sensitivity, maintaining a constant spectral profile for varying incident light polarisation. This is due to the uniform annular geometry, where the grating period has no anti-symmetric preference.

5.3.2 Single selective polariton generator

The selective polariton generator (SPG) design was a step towards introducing polarisation dependent transmission to the concept of a circular surface plasmon antenna. Two SPG structures were fabricated with the corrugation periods of 570 nm and 690 nm. The main design difference from the circular SP antennae is that the corrugations span a limited angle around the central nanohole, rather than fully encircling it. This geometry introduces angular preference to the structure, providing the basis of polarisation dependent behaviour.

The corrugation fan angle of the fabricated structures was 20º. The corrugation depth was milled to approximately 80 – 90 nm. The central nanohole diameter was 300 nm, milled through the 200 nm Au film to the glass substrate. Figure 5-8 shows a scanning electron microscope image of the fabricated SPGs with a 690 nm corrugation period.

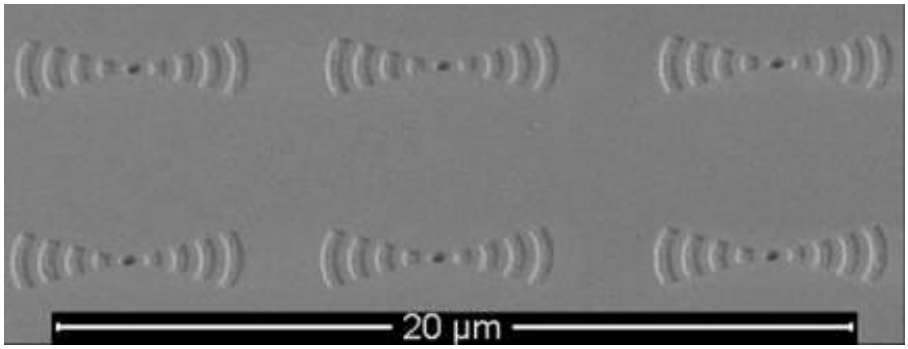

Figure 5-8. Scanning electron microscope image of single SPG structures fabricated using FIB milling. Image was taken at 52º to the substrate surface. The corrugation period of the structure is 690 nm.

Experimental measurements of polarisation and wavelength dependent properties of two single SPGs are shown in Figure 5-9 and Figure 5-10 with overlaid simulated data. The transmission has been scaled to the peak transmission intensity for the experimental and modelled results. The P0 curve refers to photon polarisation parallel to the corrugation axis, while the P90 refers to perpendicular

orientation. FDTD Solutions numerical modelling confirmed that the polarisation of incident light is preserved upon re-emission from the polariton generator structure. Therefore, the spectral properties may be characterised in either a polariser or an analyser configuration, which justified the choice of the instrumentation setup.

Figure 5-9 (a) demonstrates the spectral dependence of the SPG with 570 nm corrugation period to wavelength and polarisation of incident light. A distinct transmission peak at 672 nm with a full width half maximum of 135 nm drops in intensity as the analyser angle is altered from P0 to P90.

The polar plot in Figure 5-9 (b) presents the polarisation angle dependence of the transmission amplitude at the peak wavelength. The polarisation angle readings were recorded over 240º in 5º increments. The peak wavelength intensity reduces as the polarisation angle is rotated away from the central corrugation axis, rapidly decaying away as the angle exceeds beyond the edge of the structure's corrugation fan angle of 20º.

Enhanced optical transmission is defined as the ratio of the output to input power flux, the output power over the nanohole area divided by the power over the illuminated surface area. The enhanced optical transmission was calculated to be 9.9, at the peak wavelength. The 4-fold amplitude modulation indicates an ability to selectively switch the peak transmission 'on' and 'off' by controlling the incident photon polarisation.

Figure 5-10 (a) demonstrates the spectral dependence of the SPG with 690 nm corrugation period to wavelength and polarisation of incident light. These SPGs produced a similar response to light polarisation to the ones discussed, but at a longer peak wavelength. Here, a 757 nm transmission peak wavelength undergoes a 3.5-fold amplitude modulation when changing the polarisation from P0 to P90.

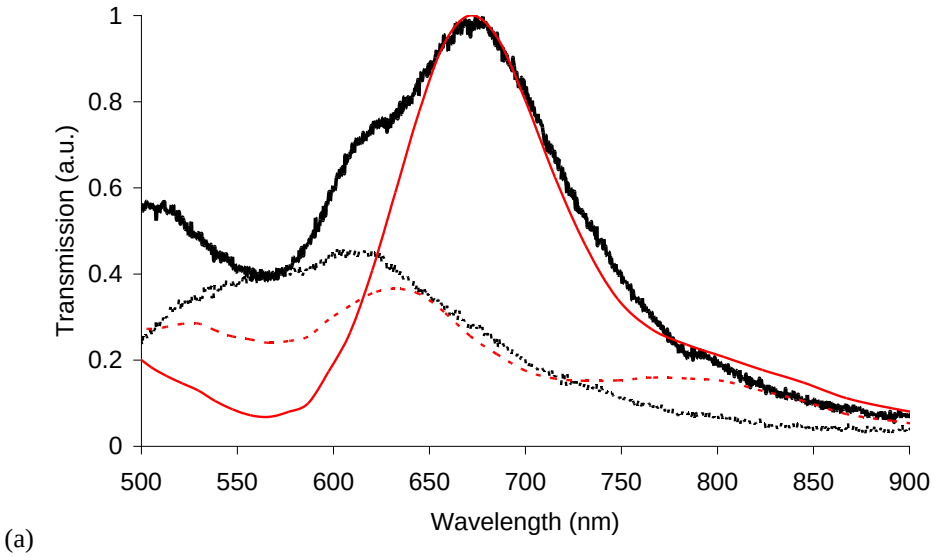

(a)

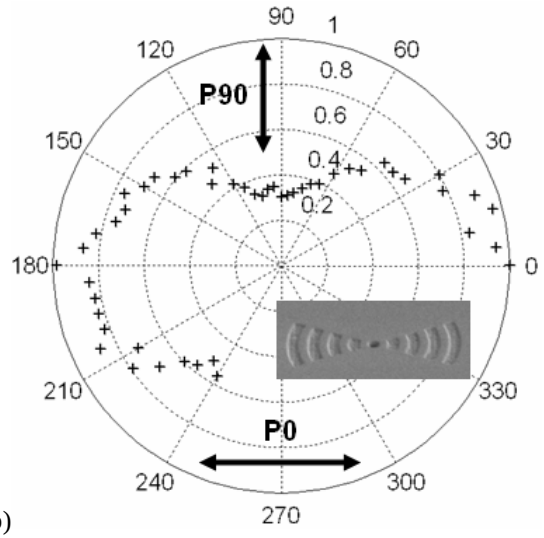

(b)

Figure 5-9. (a) Experimental (in black) and simulated (in red) transmission spectra at two light polarisations, P0 (—) and P90 (···), for SPG with corrugation periods of 570 nm. (b) Polar plots of peak transmission amplitude for polarisation angle variation over 240º in 5º increments. Bottom right inset in figure b is the SEM image of the 570 nm selective polariton generator (Sedoglavich et al. 2008c).

The enhanced optical transmission for the structure was calculated to be 7.88 at the peak wavelength. This is an increase from a single nanohole (300 nm hole

diameter), which has a calculated enhanced optical transmission of 1.4 at its peak wavelength.

The polar plot in Figure 5-10 (b) presents the polarisation angle dependence of the transmission amplitude at the peak wavelength. The polarisation angle readings were recorded over 200º in 5º increments. Here too, the peak intensity reduces as the polarisation angle is rotated away from the central corrugation axis, rapidly decaying as the angle exceeds beyond the edge of the structure's corrugation fan angle of 20º.

For both surface plasmon polariton structures the experimental and simulated transmission peaks are closely matched. Minor differences in shape possibly relate to the wide beam incidence angle (estimated to be 25º) in the experimental setup, imperfections in the fabricated devices and possible simplifications in the modelling algorithm.

Figure 5-9 (b) and Figure 5-10 (b) show that the peak intensity reduces rapidly for polarisation angles greater than ±20º from the angle of maximum intensity, which are beyond the structures' fan angle. The angle of maximum intensity coincides with the 0º axis of corrugation period. These results demonstrate the ability of SPG elements to selectively transmit a specified signal based on the incident wavelength (corrugation period) and the polarisation state.

Each of the SPG structures shown fundamentally consists of two components: a photon antenna (polariton generator) and a nanohole (polariton channel). The photon antenna is formed by corrugations on the gold film surface that partially surround the nanohole. This grating provides the necessary geometry for photon energy transfer via momentum matching between incident photons and the collective electron wave oscillation. The nanohole located in the middle acts as a channel that facilitates the propagation of polaritons through to the opposite side of the gold film (Degiron et al. 2004; Chang et al. 2005).

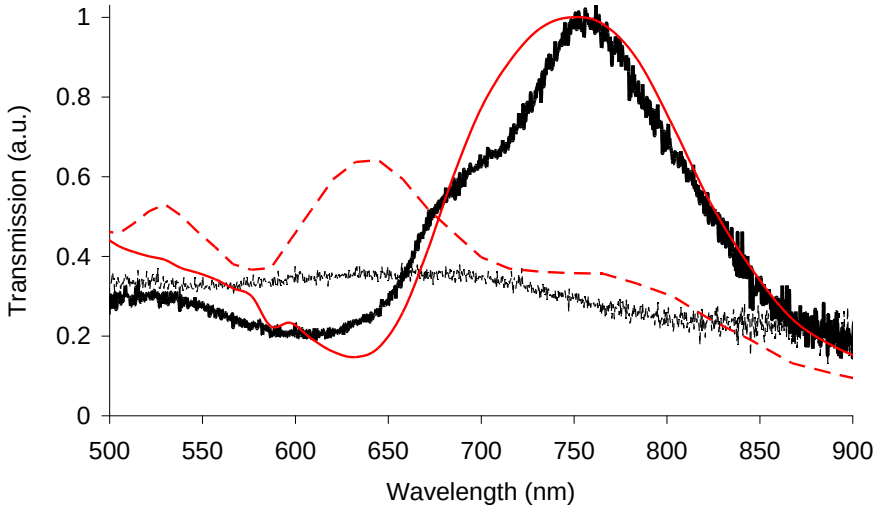

(a)

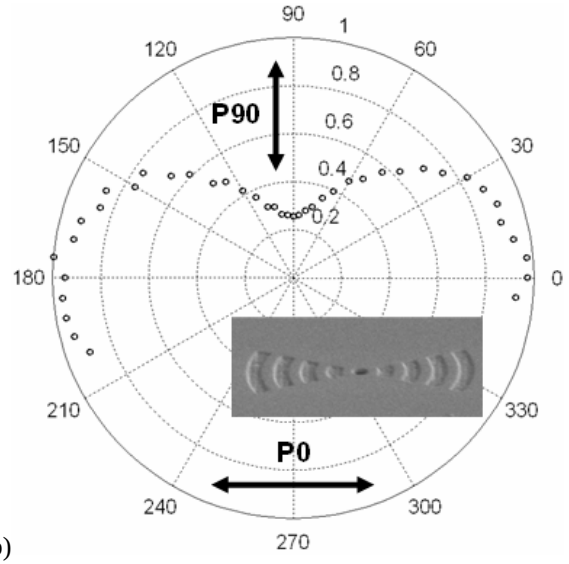

(b)

Figure 5-10. (a) Experimental (in black) and simulated (in red) transmission spectra at two light polarizations, P0 (—) and P90 (···), for SPG with corrugation periods of 690 nm. (b) Polar plots of transmission peak amplitude for polarisation angle variation over 200º in 5º increments. Bottom right inset in figure b is the SEM image of the 690 nm selective polariton generator(Sedoglavich et al. 2008c).

Spectral transmission characteristics and peak wavelength are selected based on antenna features such as corrugation period and depth. The transmission amplitude is determined by photon polarisation relative to the geometric

orientation of the polariton generator. Therefore, a selective photon-polariton coupling mechanism can be made to gate light propagation through the nanohole in a switch-like fashion. These types of components might have potential use in optical switching applications.

Characterising single selective polariton generators

The properties of circular surface plasmon antennae have previously been extensively researched and characterised (Shuford et al. 2006; Hofmann et al. 2007), where the effects of corrugation period and depth have been theoretically and experimentally defined. Here we further explore design considerations of single selective polariton structures, using FDTD numerical modelling.

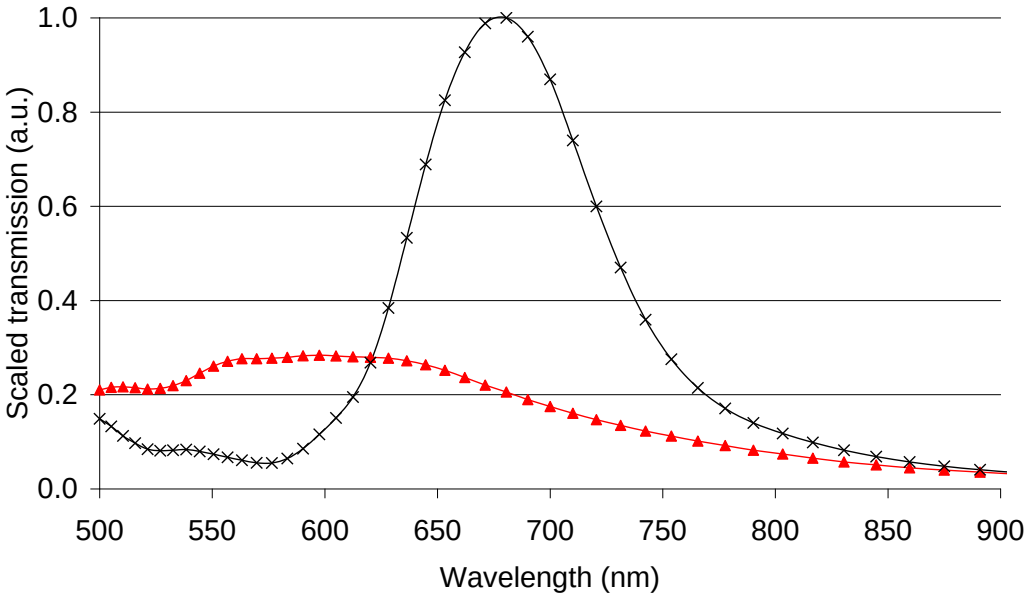

Figure 5-11. Single SPG structure of 620 nm grating period and a corrugation fan angle of 25º. Transmission scaled to the peak transmission wavelength for the light polarisation at 0º (crosses) and 90º (triangles) to the corrugation axis.

A single SPG with a 620 nm grating period has been modelled with a corrugation fan angle of 25º. The polarisation and wavelength dependent properties of the simulated structure are shown in Figure 5-11. The two transmission spectra resulted from the polarised light parallel and perpendicular to the corrugation axis. A distinct peak transmission wavelength is present at 680 nm, which is modulated 4.9 fold as the polarisation is switched by 90º from parallel to perpendicular relative to the corrugation axis.

The ratio of transmission between the two polarisations was analysed for better extraction of spectral features, shown in Figure 5-12. The highest modulation ratio of 5.1 is achieved at the wavelength of 690 nm.

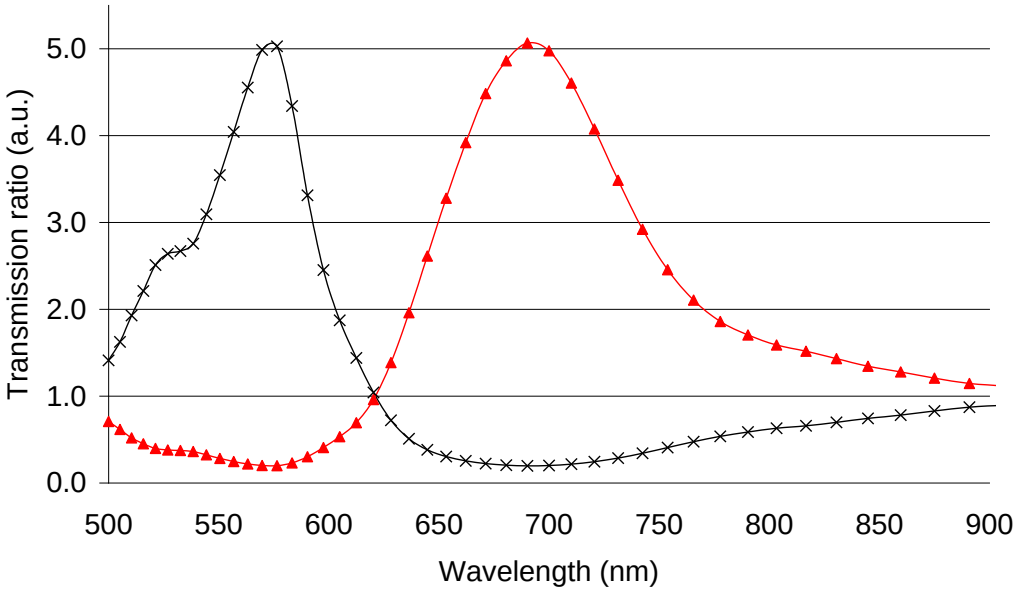

Figure 5-12. Single SPG structure of 620 nm grating period and a corrugation fan angle of 25º. Transmission ratio of polarisation at 0º relative to 90º (0º : 90º triangles, 90º : 0º crosses).

There is another wavelength present with significant, 5 fold, intensity ratio modulation, at 576 nm. This is a byproduct of the structure's partially encircled nanohole rather than design intent. This secondary modulation peak offers a single

SPG with wavelength and polarisation differential analysis. This extra feature, however, is more pronounced in single SPGs of shorter corrugation periods. It is caused by the partially encircled nanohole, exhibiting properties of an isolated hole for polarisation angles not flanked by corrugations. The transmission profile of an isolated nanohole has a preferential transmission of shorter wavelengths. The feature of the isolated nanohole is least inhibited when the light polarisation is perpendicular to the corrugation axis.

Figure 5-13 shows the normalised transmission and the peak transmission wavelength of the modelled 570 nm SPGs with varying corrugation fan angles from 5º to 26.5º. An aspect of design consideration for single SPGs is the extent of the surface plasmon polariton excitation near the edges of the structures and how far away from the structure does excitation occur.

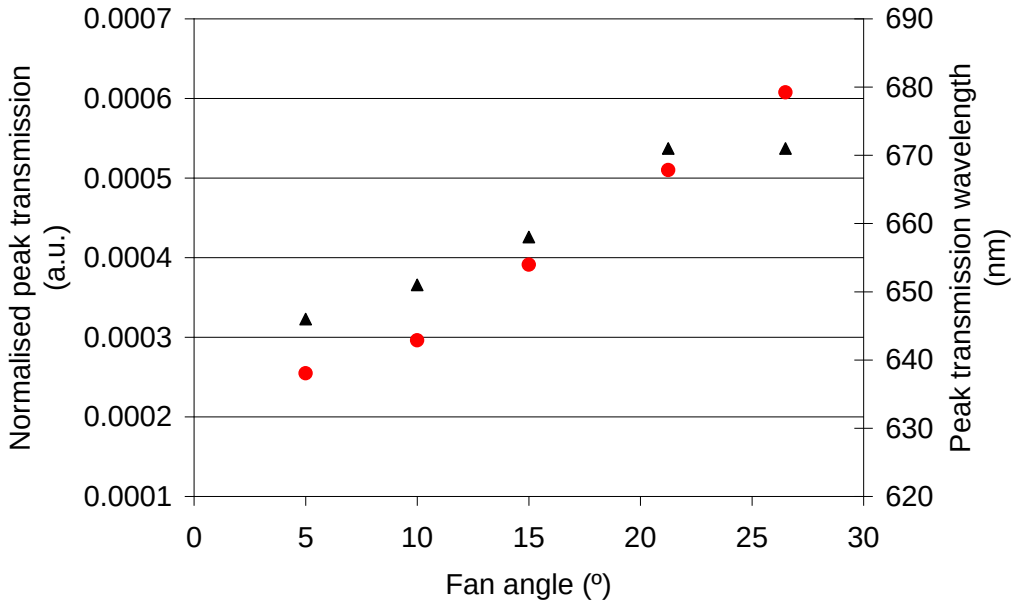

Figure 5-13. Peak transmission intensity (circles) is normalised to the amount of light incident upon the illuminated surface and peak transmission wavelength (triangles) as the structure's fan angle is varied from 5º to 26.5º.

For the same polarisation angle, at 0º to the corrugation axis, the peak transmission wavelength is red-shifted as the corrugation fan angle is increased, reaching a limit of 671 nm for fan angles larger than 20º. These results closely agree with the experimental results from section 5.3.2, where the peak transmission wavelength of a 570 nm SPG with 22º corrugation fan angle was measured to be 672 nm.

There is also a continuous increase in transmission intensity for wider corrugation fan angles indicating a more complex travel path of the polaritons, rather than a straight path parallel to the polarisation angle. Travelling surface plasmon polaritons might be experiencing reflections and guiding introduced by the edges of the corrugation structure. For maximising the peak intensity, a significant design consideration is the corrugation fan angle of the inner first corrugation ring. Due to the exponentially decaying travelling surface plasmons, the resulting transmission intensity was most affected by the inner resonant corrugation ring, increasing as the fan angle around the central nanohole is increased.

The following section explores the implementation of plasmonic Bragg reflectors within the single SPG designs.

5.3.3 Plasmonic Bragg reflector flanked configuration

After demonstrating the function of selective polariton generators, it was intended to further enhance the enhanced optical transmission of the system by flanking the SPGs with plasmonic Bragg reflectors (Marthandam and Gordon 2007).

Literature reported that plasmonic Bragg reflectors have improved enhanced optical transmission through subwavelength apertures. This has led us to investigate further SPG development by adding plasmonic Bragg reflectors to reflect scattered travelling surface plasmons back towards the central nanohole.

Several SPGs with a grating period of 690 nm and corrugation fan angle of 25º were simulated with additional secondary corrugations which act as Bragg reflectors. To meet the Bragg reflection condition, the periodicity of the secondary corrugations was chosen to be half the periodicity of the enclosed SPG grating. To reflect in-phase with the structure's transmitted light, the secondary corrugations were placed half a period away from the primary SPG corrugations.

The Bragg reflector corrugations were constructed with a 345 nm period of 25º fan angle at 345 nm away from the primary SPG corrugations. All the corrugation depths were set to 60 nm. Figure 5-14 shows the top view of the FDTD simulation model layout with three resonant and four secondary corrugations, which act as plasmonic Bragg reflector.

Figure 5-15 shows the results of five numerically modelled SPG configurations. The first two cases are of the SPG with two resonant 690 nm corrugation rings, with and without four Bragg reflector corrugations. The second two cases are of the SPG with three resonant 690 nm corrugation rings, with and without four Bragg reflector corrugations. The plain solid line shows the normalised transmission of the SPG with four resonant 690 nm corrugation rings without the plasmonic Bragg reflectors.

Due to the plasmonic Bragg reflectors, the single SPGs with only two resonant corrugations had largest enhancement. The peak wavelength blue-shifted from 705 nm to 675 nm, at which the intensity increased by 37%. This is 30% higher than the intensity of the original peak. Such significant enhancement is a result of the scattered polaritons travelling a short distance before reaching the central nanohole. However, due to only two resonant corrugations, the resonant condition was not tightly defined, resulting in wide spectral width. When Bragg reflectors are introduced, the spectral peak also becomes narrower, as they are designed to reflect at a specific wavelength.

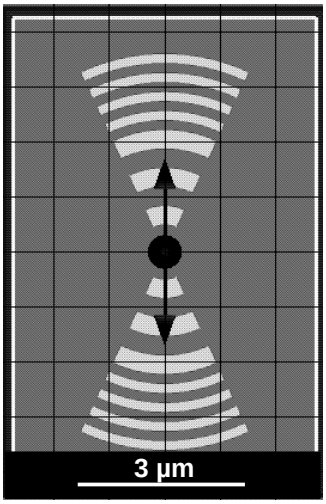

Figure 5-14. Top-down view of the FDTD modelled layout of a single SPG structure with three resonant, 690 nm grating periods, and four secondary corrugations which act as plasmonic Bragg reflectors.

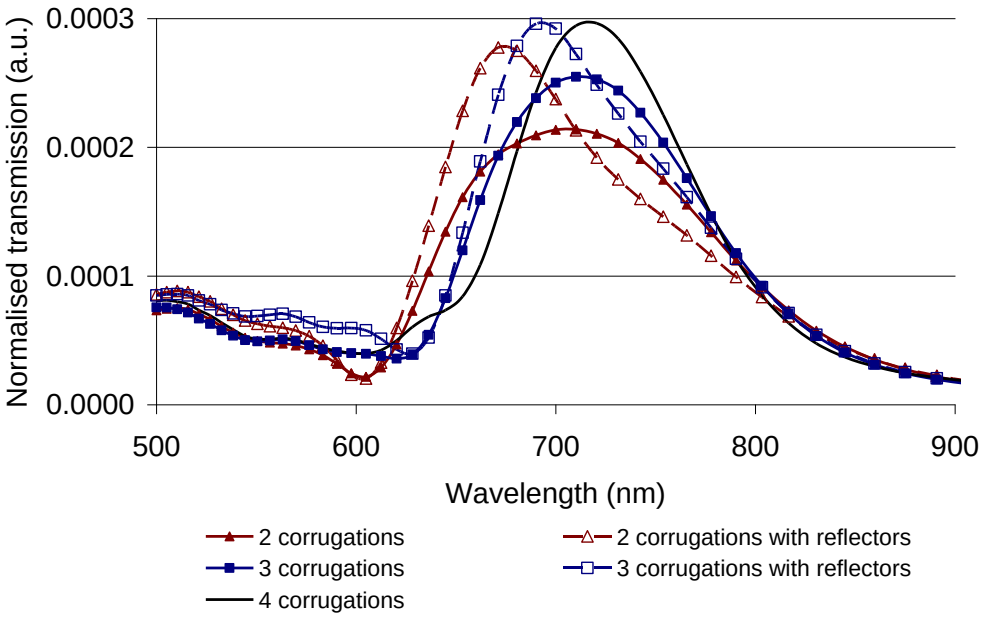

Figure 5-15. Transmission spectra, normalised to the amount of light incident on the structure, of five simulated single SPG configurations of 690 nm grating period with and without the secondary corrugations which act as plasmonic Bragg reflectors.

In the configuration of two resonant corrugations with plasmonic Bragg reflectors, the secondary corrugations are very close to the central nanohole. Therefore, these might exhibit secondary effects acting as resonant corrugations which couple shorter wavelength photons into polaritons and as plasmonic Bragg reflectors which focus the scattered polaritons back towards the nanohole. Along with the significant enhancement in optical transmission, this may explain the significant blue-shift of the peak transmission wavelength.

A less significant enhancement due to Bragg reflectors is seen for the SPGs with three resonant corrugations. The peak wavelength blue-shifted from 715 nm to 690 nm, at which the intensity increased by 24%. This is 16% higher than the intensity at the original peak. The lesser enhancement here is because the scattered surface plasmon polaritons having to travel a greater distance before reaching the central nanohole, decaying in intensity along the way. Here, we get a sharper spectral transmission peak as the third resonant corrugation tightens the wavelength selectivity condition.

The addition of Bragg reflector corrugations to the SPG layout, was an attempt to further increase the transmitted signal by reflecting scattered surface plasmon polaritons back towards the central nanohole, contributing to the overall transmission.

None of the Bragg reflector flanked configurations offered a higher transmission peak than the plain single SPG with four resonant corrugations. A small increase of around 7% in transmission intensity was achieved by the addition of a 5th resonant corrugation ring, indicating a saturation point, which limits the effect of the resonant corrugation rings by the rate of decay of travelling surface plasmon polaritons. The Bragg reflectors do not provide a significant transmission enhancement for SPGs with more than three resonant corrugations as the exponentially decaying intensity of travelling surface plasmons has the approximate propagation length of 3 μm (Homola et al. 1999b).

5.3.4 Summary

A surface plasmon polariton structure was developed, fabricated, and characterised, which can, by controlling light polarisation, selectively generate and transport polaritons of a desired wavelength. These SPG devices combine a tuneable plasmon resonator and a nanohole. The incident photon polarisation angle relative to the partially circular geometry, determined the transmission amplitude characteristics. This variable photon-polariton coupling mechanism permitted gated light propagation through the central nanohole in a switch-like fashion.

The addition of Bragg reflector corrugations to the SPG layout was an attempt to further increase the transmitted signal by reflecting scattered surface plasmon polaritons back towards the central nanohole, contributing to the overall transmission. None of the Bragg reflector flanked configurations offered a higher transmission peak than the one with only four resonant corrugations. Due to the exponentially decaying intensity of travelling surface plasmon waves, the plasmonic Bragg reflectors do not provide a significant transmission enhancement for SPGs with more than three resonant corrugations.

The simulations were compared with the experimental results for agreement of the models, which led to further investigation into more complex structures. The following section discusses the work on multi-state surface plasmon generator structures.

5.4 Multi-state selective polariton generators

Multi-state selective polariton generator structures utilise partial or fully encircling corrugations of multiple periodicities, surrounding a single central nanohole. Here we report on our investigation into various design aspects of the surface plasmon polariton structures with specific polarisation and wavelength selectivity. The structures have been modelled for optical transmission, gated switching, and polarisation selective properties.

The development of single SPG geometry, section 5.3.2, has led to the design and fabrication of a nanophotonic device with multiple elements. To explore this approach, two single SPGs were combined orthogonally around a single nanohole. This approach offers discrete polarisation dependent states of transmission wavelength. Another variation to the theme was the continuously varying grating period around the central nanohole, promising polarisation tuneable wavelength selective transmission.

Sections 5.4.1 and 5.4.2 discuss partially encircled structure by multiple individual SPGs, while the fully encircled polarisation tuneable SPG structure is described in section 5.4.3.

5.4.1 Paired selective polariton generators

Two single SPGs were combined orthogonally around a single nanohole to explore the concept of developing structures that may offer discrete polarisation dependent transmission states. These two SPGs have been combined to form a multi-state device. The performance of this new device is studied to determine its potential as a useful plasmonic element. Simulated and experimental results are presented.

A device was fabricated using FIB lithography, with combined corrugations of 570 nm and 690 nm respectively, fan angles of 23° and the corrugation depth of

~80 nm. The SEM image of the structures is shown in Figure 5-16, taken at 52° to the substrate surface.

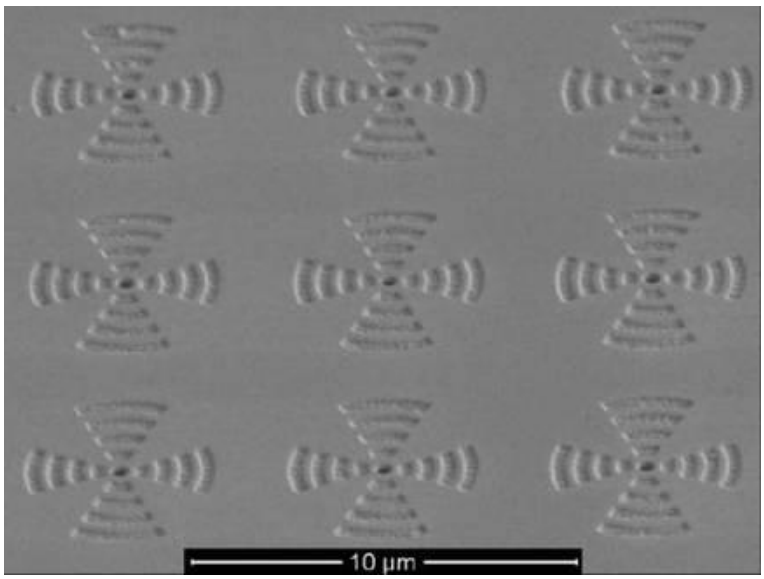

Figure 5-16. Paired selective polariton generators fabricated using FIB milling. Scanning electron microscope image was taken 52º to the substrate surface of the orthogonally paired SPG nanophotonic device (vertical and horizontal corrugation periods of 690 nm and 570 nm respectively).

The experimental spectral and polarisation characteristics of this structure are shown in Figure 5-17. The transmission plot in Figure 5-17 (a) demonstrates amplitude modulation of the two distinct transmission peaks at 662 nm and 774 nm, resulting from the change in the photon polarisation observed at 570 nm and 690 nm corrugation periods respectively. In Figure 5-17 (a) the legends P90 to P180 are the polarisation angles of light being measured.

The transmission peak at 662 nm alters in intensity 10-fold as the photon polarisation is changed by 90°. The 774 nm peak alters in intensity approximately 4-fold as the photon polarisation changed by 90°. The curves depict the transition for the 662 (774) nm peaks from on (off) to off (on).

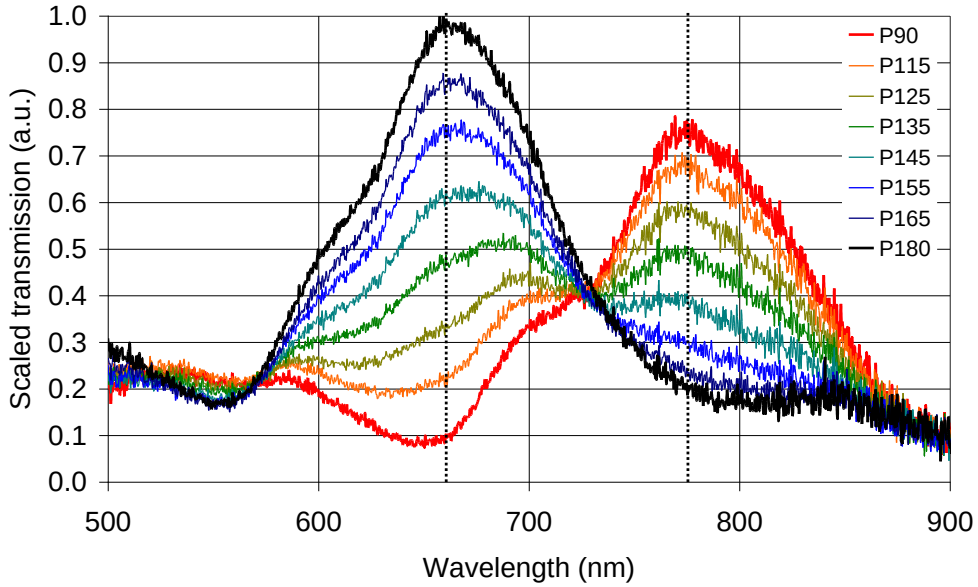

(a)

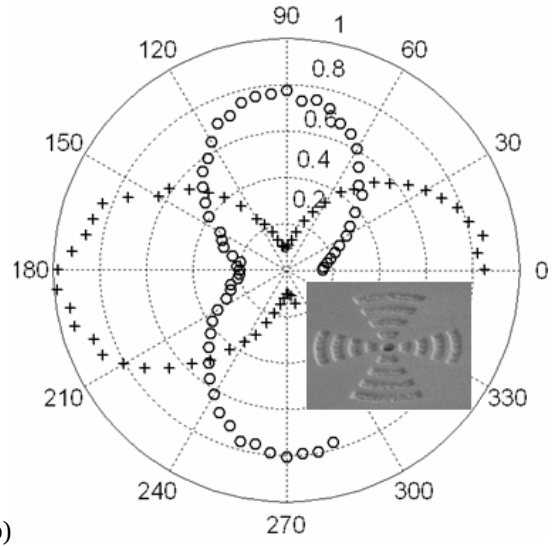

(b)

Figure 5-17. Characterisation of paired SPG device that combines two single SPGs of different corrugation periods, (570 nm horizontal and 690 nm vertical) centred around a single 300 nm diameter nanohole. (a) Experimental transmission spectra showing peak modulation over varied light polarisation angles. P90 to P180 refers to the polarisation angle of light being measured. (b) Polar plot of intensity versus polarisation angle for the two peaks at 662 nm (+) and 774 nm (O) showing out-of-phase light modulation (Sedoglavich et al. 2008c). The bottom right inset, in figure b, is the SEM image of the paired selective polariton generator.

The polar plot in Figure 5-17 (b) presents the transmission at each of the individual peak wavelengths. The polarisation angles range over 285° in 5° increments. This experimental data clearly exhibits synchronized modulation between the two transmission peaks, where one peak leads another peak by 90°. Hence, tri-state operation is achieved by incident photon modulation in polarisation and intensity (i.e. 0°, 90° and no resonant photons).

An additional observation is that in the combined SPG configuration, with multiple states, there is an increase in the amplitude swing for each peak over that obtained from single SPGs. This is a suppression of the spectral characteristics of an isolated nanohole. The spectral characteristic of an isolated nanohole is still present in single SPGs when the light polarisation is perpendicular to the corrugation axis. This suppression resulted in enhanced amplitude swing from 4 to 10-fold for 570 nm corrugation period, and from 3.5 to 4-fold for 690 nm corrugation period in the paired SPG configuration.

Characterising paired selective polariton generators

The design of a nanophotonic device is possible by combining multiple SPG elements around a central nanohole. The design considerations of grating periods, corrugation fan angles, transmission due to inner ring variations, and spectral separation of paired SPGs were investigated. The simulations were compared with the experimental results for agreement of the models, which may lead to experimental investigations of more complex structures.

Several different paired SPG structures were modelled with a range of grating periods, from 570 nm to 730 nm. The models looked at separation of the peak transmission wavelengths and crossover between individual spectra in the orthogonally paired configuration. The main design variables that were investigated were individual periodicity, photon-plasmon coupling efficiency, and individual corrugation fan angles.

The transmission characteristics of three paired SPGs are shown in Figure 5-18 for incident light polarisations of 0º and 90º relative to the corrugation axes. Their individual corrugation periods are 570:730 nm, 600:690 nm and 600:730 nm respectively. Figure 5-19 shows the transmission ratio of the same structures for incident light polarisations of 0º and 90º relative to the corrugation axes.

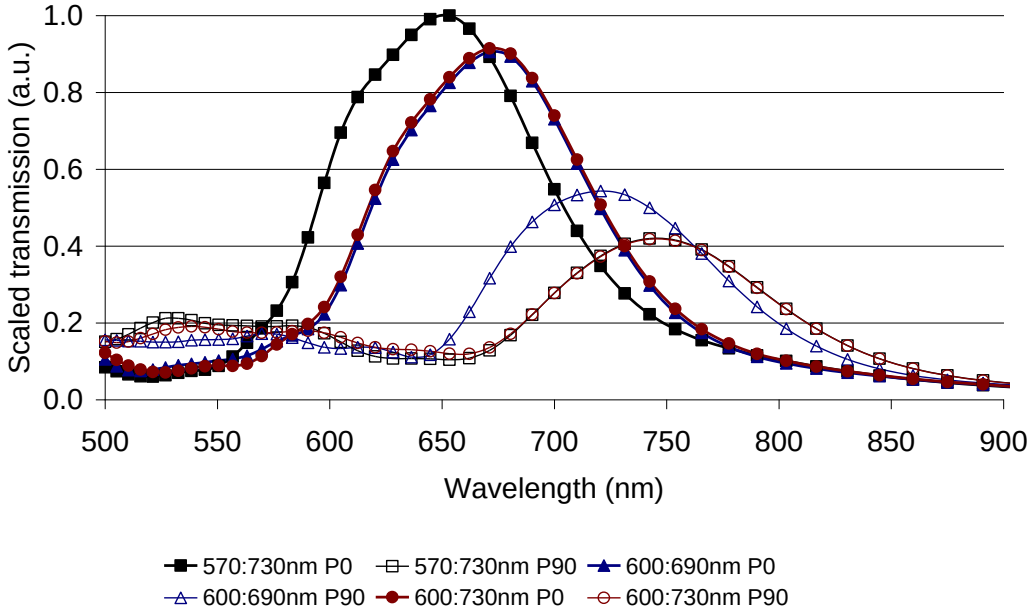

Figure 5-18. Paired SPG devices that combine two single SPGs of different corrugation periods centered on a 300 nm diameter nanohole. Transmission spectra of 570:730 nm, 600:690 nm and 600:730 nm paired SPGs with 21.5º and 25º structural fan angles respectively.

Figure 5-18 shows scaled transmission for the three structures, where each has a peak wavelength present for the individual polarisation states. The 570:730 nm paired SPG has peak wavelengths at 653 nm and 743 nm. These wavelength peaks are similar to the experimental results found in section, 5.4.1. There is a ~10 nm and ~30 nm respective red-shift from the experimentally measured 662 nm and 774 nm peaks. The 600:690 nm paired SPG has the peak wavelengths at 671 nm

and 721 nm. The 600:730 nm paired SPG has the peak wavelengths at 671 nm and 743 nm.

The numerically modelled structures tend to produce a closer spectral match with the experimental results for shorter corrugation periods while the data for longer period corrugations tends to be significantly red-shifted. There is also a noticeable underestimation of transmission peak intensities for longer corrugation periods, seen by the significantly lower transmission relative to the data from shorter corrugation periods. This was concluded by comparing the simulated data to the experimentally acquired results from a fabricated 570:730 nm paired SPG.

Figure 5-19 (a-c) shows the transmission ratio of three paired SPG configurations. The models illustrate that structures with shorter corrugation periods have higher transmission intensity, which leads to polarisation states having different peak intensities.

This characteristic is also present to a lesser extent in the experimental result of the paired SPG presented in section 5.4.1. The main cause of this variation is the reduced photon-plasmon coupling efficiency which is intrinsic to the structure's design. The modelled peak transmission wavelength is blue shifted relative to the experimental results.

The 570:730 nm structure has a transmission ratio of 9.5 and 2.6 for the two polarisation states at 650 nm and 780 nm wavelengths respectively, Figure 5-19 (a). The 600:690 nm structure has a transmission ratio of 6.6 and 2.2 for the two polarisation states at 640 nm and 780 nm wavelengths respectively, Figure 5-19 (b). The 600:730 nm structure has a transmission ratio of 7.4 and 2.6 for the two polarisation states at 660 nm and 790 nm wavelengths respectively, Figure 5-19 (c).

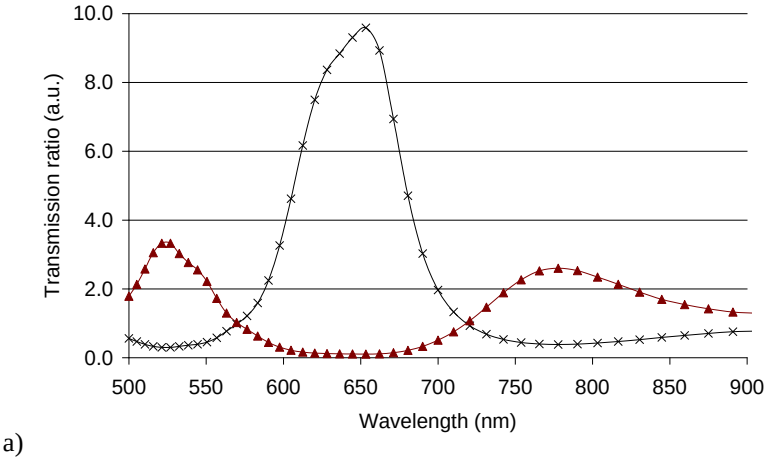

a)

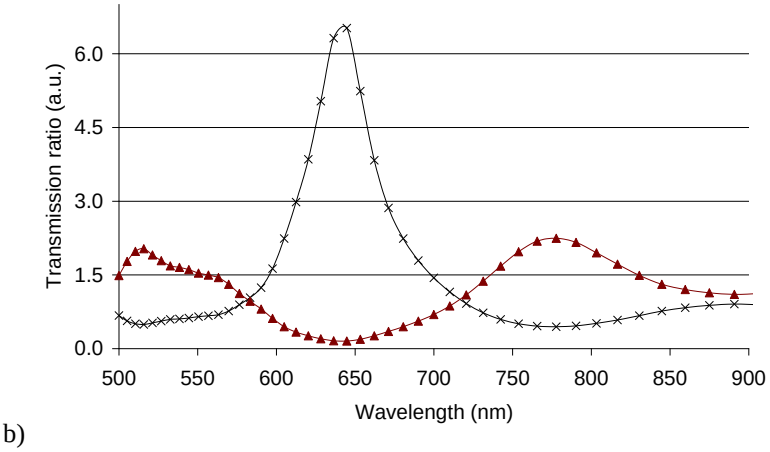

b)

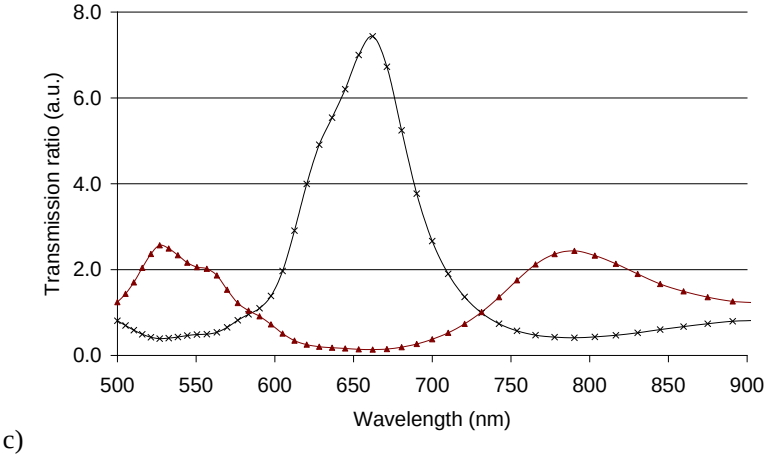

c)

Figure 5-19. Paired SPG devices that combine two single SPGs of different corrugation periods centred on a single 300 nm diameter nanohole. (a-c) transmission ratio of 570:730 nm, 600:690 nm and 600:730 nm structures of polarisation at 0º relative to 90º (0º : 90º crosses, 90º : 0º triangles).

In order to compensate for the disproportionate transmission between different states, the paired SPG design can be optimised further by increasing or decreasing the corrugation fan angles. Figure 5-20 shows the spectral and polarisation characteristics of the optimised 600:690 nm paired SPG structure modelled with a few variations from the original design seen in Figure 5-18 and Figure 5-19.

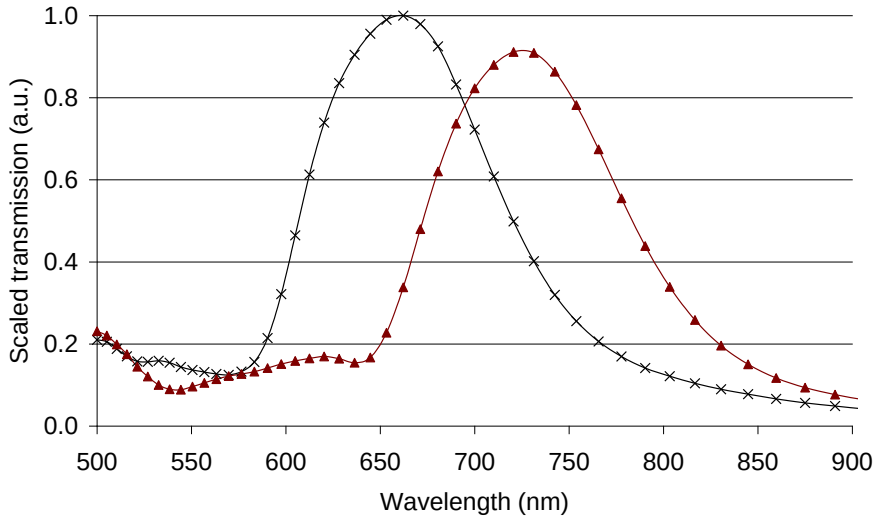

(a)

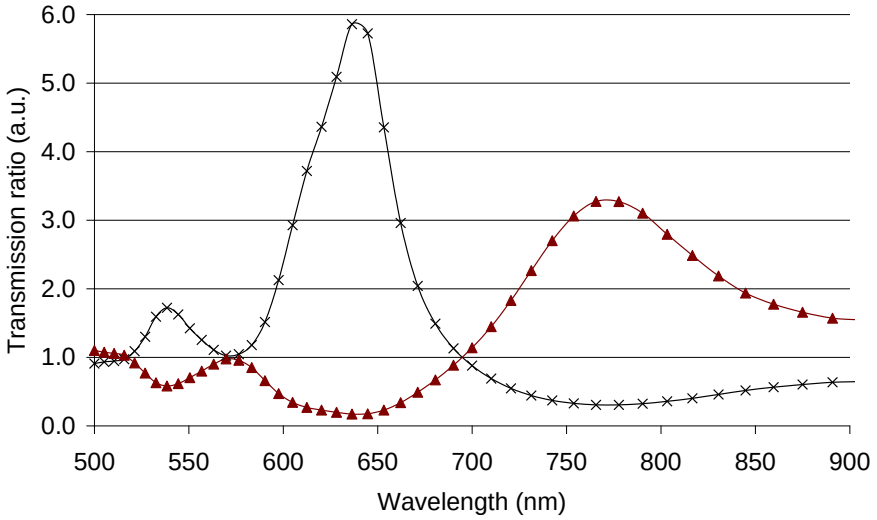

(b)

Figure 5-20. Optimised paired 600:690 nm SPG with 15º and 25º structural fan angles and a 22.5º wide first 690 nm corrugation ring (a) scaled transmission spectra showing peak modulation for two orthogonal light polarisation angles, (b) transmission ratio of the two polarisation states.

The corrugation fan angle of the 600 nm grating was reduced from 21.5° to 15°, allowing for a relative increase of the second transmission peak. This was caused by a drop in intensity of the first peak producing an overall drop throughout the entire spectrum. This reduced the second peak's OFF level intensity, resulting in a greater modulation ratio.

Another design change was the increase of the corrugation fan angle of the first ring on the 690 nm corrugation periods. As the first corrugation ring has the strongest amplitude contribution towards the transmission spectrum, this resulted in an increase of the second peak's transmission ratio, by increasing the intensity of the ON level.

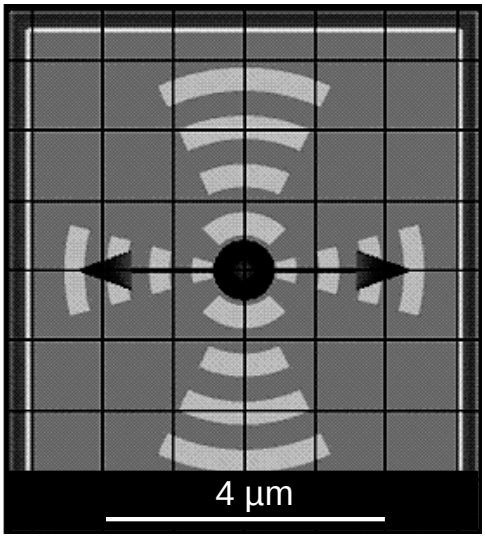

Figure 5-21. Top-down view of the optimised paired 600:690 nm SPG with 15º and 25º fan angles. First 690 nm corrugation ring is 22.5º wide.

The combination of the above two design changes produced an overall increased modulation ratio of the second transmission state of 50% at 780 nm, while the modulation ratio of the first state was only reduced by 10% at 640 nm. The model layout of the optimised 600:690 nm paired SPG structure is shown in Figure 5-21.

The following section discusses the work on a multi-state surface plasmon generator structure consisting of three partially encircling SPG structures.

5.4.2 Triplet SPG structure

The stage that followed the paired SPG development was the fabrication of a structure where three and four single SPGs were combined around a single nanohole. The SEM image of the FIB fabricated structure with three SPGs is shown in Figure 5-22. The individual SPG elements had the grating periods of 570 nm, 630 nm and 690 nm.

(a) 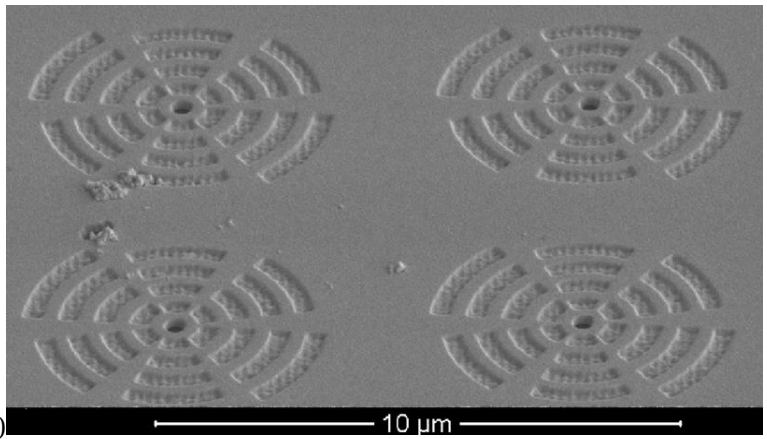

Figure 5-22. SEM image of triplet SPG structures, consisting of three individual SPG elements with 570 nm, 630 nm and 690 nm grating periods.

The triplet-SPG structure was experimentally characterised. The structure was analysed with the light polarisation angles through 360° in 5° increments. The spectral transmission plots are shown in Figure 5-23, with the polarisation angle range of 0° – 90° and 90° – 180° for plots (a) and (b) respectively. As experimentally determined and confirmed through modelling, the main limitation in designing multiple discrete states is the crosstalk between the individual grating geometries.

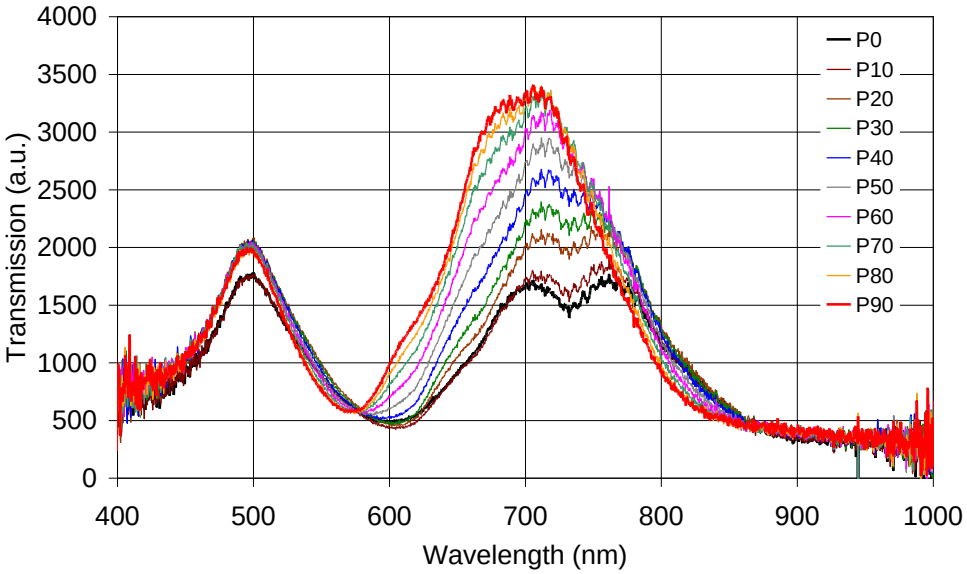

a)

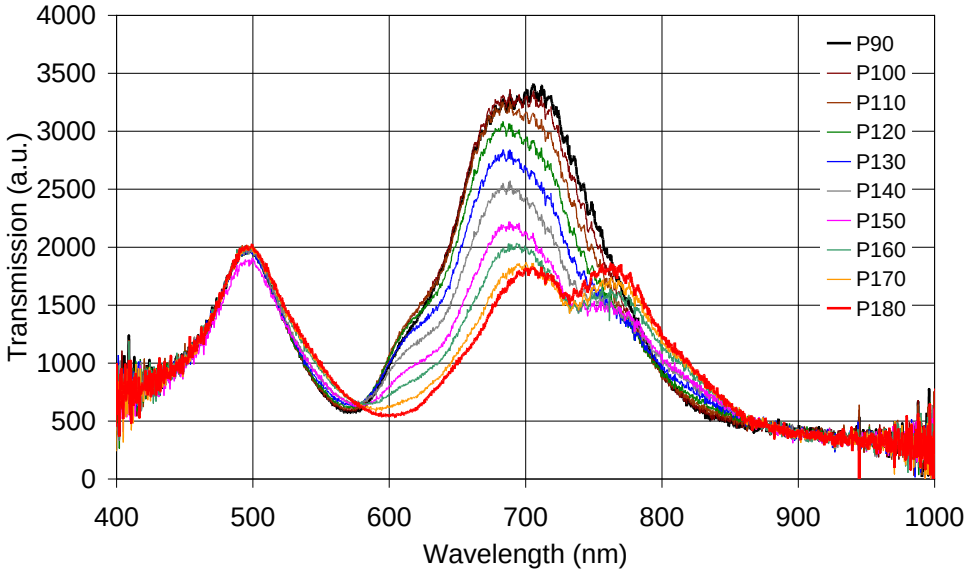

b)

Figure 5-23. Experimentally determined spectral transmission plots of a triplet-SPG with 570 nm, 630 nm and 690 nm grating periods. The range of light polarisation angles are (a) 0° – 90° (P0-P90) and (b) 90° – 180° (P90-P180).

Individual peaks are detectable, but there is a lot of coupling between each of the three individual SPGs. This prevents the spectrum from having separate transmission states associated with each SPG segment, causing a continuously varying spectrum. As more individual resonant grating geometries are

accumulated around a central nanohole, the individual peak transmission states (bands) start to merge into a continuously transitioning, spectrally shifting transmission peak.

By removing the inner-most corrugation ring, the inter-SPG coupling may be minimised, at the trade-off to intensity drop. Based on the unsatisfactory experimental results of the triplet-SPG structure, the characterisation of the quad-SPG was abandoned.

The following section discusses the work on a multi-state surface plasmon generator structure with the fully encircling SPG structure. The structure offers continually tuneable polarisation and wavelength selective behaviour.

5.4.3 Polarisation tuneable selective polariton generator

A SPG design, based on surface plasmon antennae principles, is demonstrated to provide a selective light transmission peak. The polarisation-sensitive structure selectively generates and transports polaritons of a desired wavelength through a circular subwavelength aperture.

Two polarisation tuneable structures were designed and fabricated with custom geometry to permit continuous transition of the polarisation and wavelength selective transmission peak. These were based on a nanohole flanked with a grating geometry where the corrugation period varies from 570 nm to 690 nm as the angle around the nanohole varies, from the horizontal to vertical axis. The range of corrugation periodicity was spread over 90º, symmetrically encircling the central nanohole.

As discussed in the previous sections of this chapter, by varying the state of incident light polarisation, different surface corrugation periodicity is selected, which controls different optical transmission peak wavelengths. Here a

polarisation tuneable SPG structure was designed to permit continuous tuning of its wavelength dependent transmission peak by the angle of the incident, linear polarised light. One set of structures has the nanohole within elliptical corrugations, while the other tuneable structure was designed with custom encircling geometry.

The elliptical geometry does not exhibit linear relationship between the change in the polarisation angle and the change in the corrugation period. Therefore, the new geometry was designed to provide a linear relationship between the change in polarisation angle and the change in the corrugation period. The SEM image of the tuneable, linearly continuous SPG is shown in Figure 5-24.

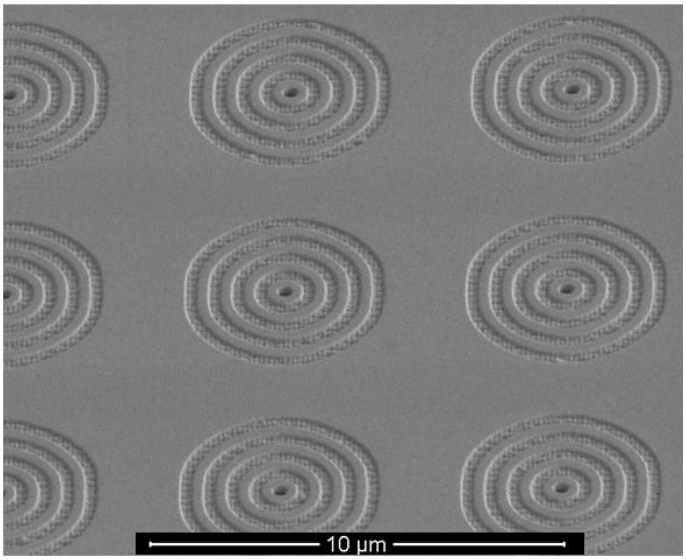

Figure 5-24. Scanning electron microscope image, taken at 52º to the substrate surface, of a linearly continuous SPG fabricated using FIB milling. Corrugation period along the horizontal and vertical axis is 570 nm and 690 nm, respectively.

The radius of each corrugation is related to the structures periodicity, which is defined by,

$$\Lambda = \Lambda_i + \frac{2\theta}{\pi}\left(\Lambda_f - \Lambda_i\right), \qquad \text{Eq. 5-1}$$

where the periodicity Λ depends on, Λ_i and Λ_f are the initial and final periodicity respectively, and θ is the polarisation angle of incident light. This results in a linear relationship between the change in periodicity and the change the polarisation angle.

$$\frac{d\Lambda}{d\theta} = \frac{2}{\pi}\left(\Lambda_f - \Lambda_i\right), \qquad \text{Eq. 5-2}$$

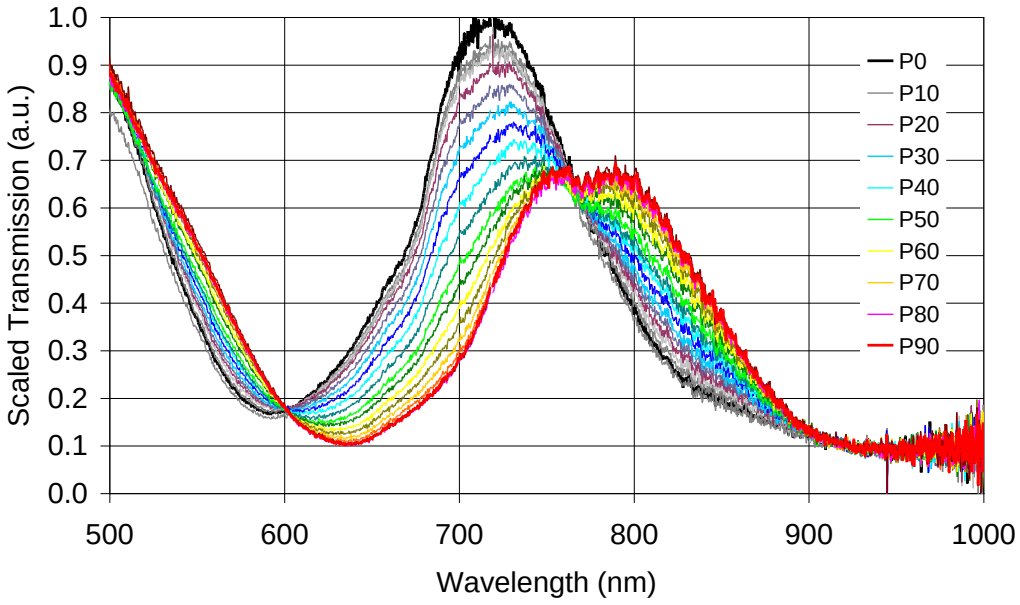

Figure 5-25. Experimental results of the linearly tuneable SPG for light polarisation angles from 0º to 90º (P0-P90) (Sedoglavich et al. 2009).

The SPG structure was experimentally characterised and compared with the numerical FDTD model. The experimentally obtained spectral and polarisation characteristics are shown in Figure 5-25. The data was recorded at 5º intervals over a 360º range of polarisation angles. The figure presents a subset where the light polarisation angle was varied over a range of 90º.

At a polarisation angle of 0º, parallel to the 570 nm corrugation, horizontal axis, the transmission curve peaks at 718 nm. As the polarisation angle is increased, the transmission peak gradually shifts to longer wavelengths. When the angle is increased past 90º, i.e. parallel to the 690 nm corrugation axis, the transmission curve starts to shift back to the blue wavelength range. The cycle repeats as the polarisation angle is rotated through a full range of 360º.

The experimental results demonstrate the structure's tuneable characteristics, with the transmission peak varying from 718 nm to 758 nm. However, a minor secondary peak develops as the polarisation angle approaches 90º.

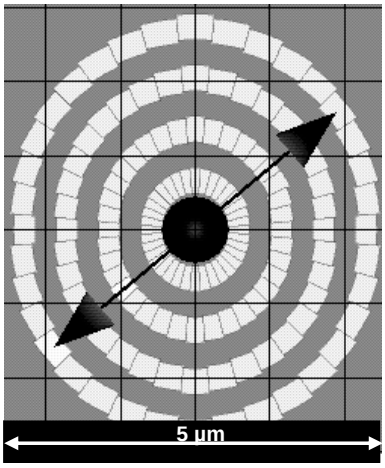

Figure 5-26. Discretized FDTD layout of the linearly tuneable SPG structure model. For the particular layout, the black, two edged arrow represents the modelled incident light polarisation of 40º from the 570 nm corrugation axis.

As it was not possible to simulate continuously varying periodicity, the FDTD model approximated the true structure. The corrugation periods were discretised into 10º steps. The layout of the numerical model is shown in Figure 5-26. The transmitted light collection was modelled within a 15º output cone. The figure shows a particular simulation where the incident light polarisation was set to 40º from the 570 nm corrugation axis.

The simulated spectral and polarisation characteristics of the tuneable SPG structure are shown in Figure 5-27. The simulations were run at 10º polarisation angle intervals from 0º to 90º. At 0º the transmission curve peaks at 680 nm, red-shifting as the polarisation is increased towards 90º.

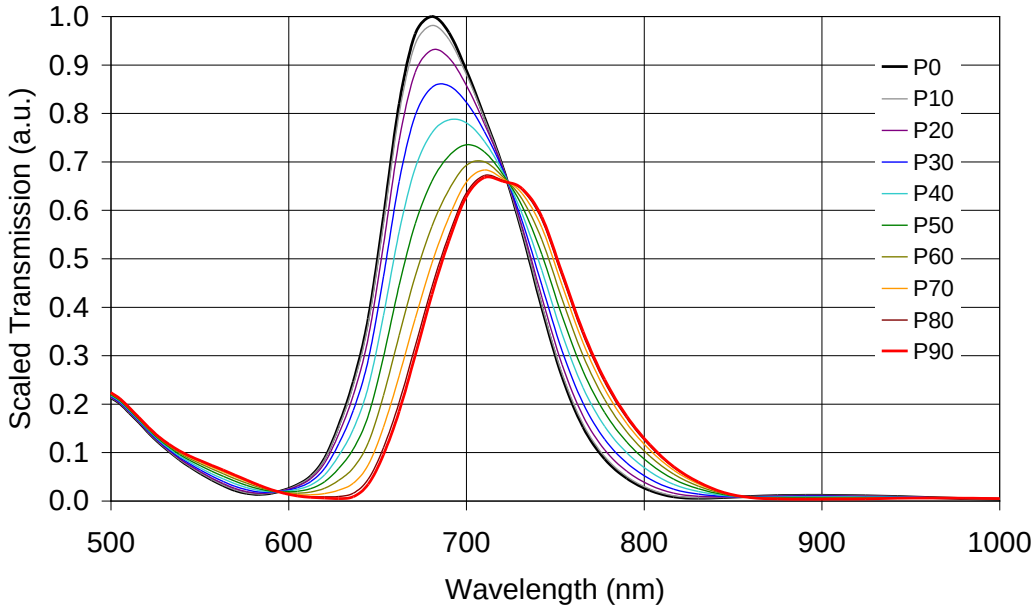

Figure 5-27. Simulated results of the linearly tuneable SPG for light polarisation angles from 0º to 90º (P0-P90) (Sedoglavich et al. 2009).

Using FDTD modelled data the enhanced optical transmission for the structure was calculated to be 17.2 and 12.1 for the polarisation angles of 0° and 90° respectively. The simulated data exhibits similar spectral and polarisation characteristics as the experimental results. The most noticeable differences are the

transmission peak which is blue-shifted 40 nm and the smaller secondary peak in the simulated data.

The experimental and modelled spectral responses were compared. Figure 5-28 presents the wavelength change of the left transmission peak as the light polarisation angle is varied through 90º. A second x-axis is shown to illustrate the expected corrugation period at each polarisation angle.

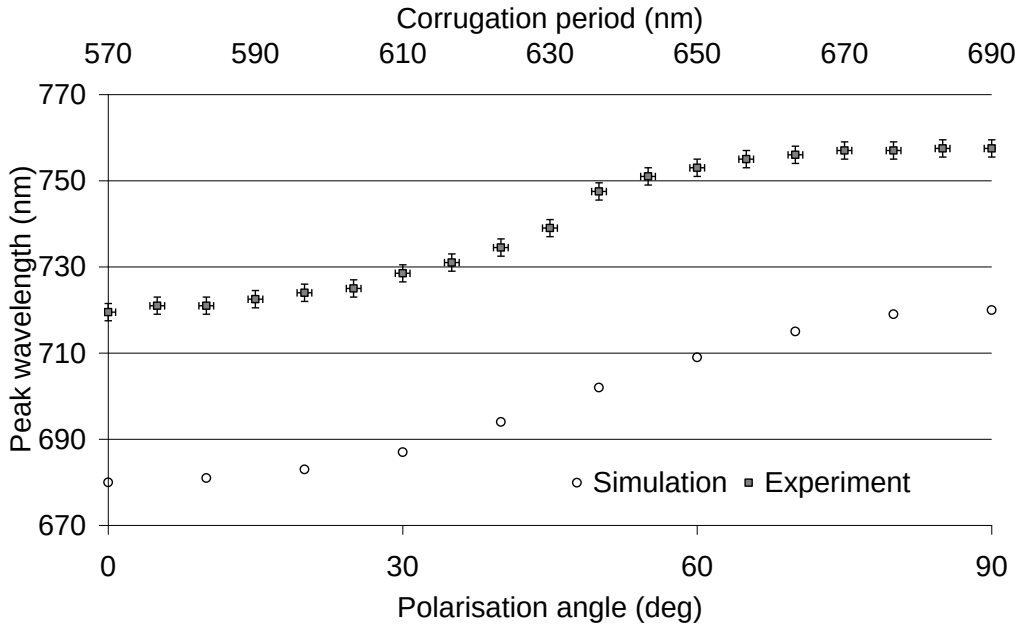

Figure 5-28. Comparison of the experimental and the modelled results, tracking the left transmission peak (Sedoglavich et al. 2009).

In the middle region, between 20º and 70º, the peak transmission wavelength is linearly dependent on the polarisation angle in the simulations, while at the extremes the rate of change decays away. Experimental results have similar transmission behaviour, however not quiet as linear.

Both the experimental and simulated data exhibit the same spectral shift of 40 nm over the full range of polarisation angles, but over a slightly different transmission

wavelength range. The error bars in the experimental results correspond to the readout error, ±1º for the polarisation angle and ±2 nm for the peak transmission wavelength. This data clearly demonstrates the structure's tuneable transmission characteristics.

5.4.4 Summary

Based on the development of surface plasmon antennae with partial circular gratings, selective polariton generator designs allowed for a variety of geometric configurations around a central nanohole. Here reported were the investigations into various design aspects of multi-state surface plasmon polariton structures.

Multi-state SPG designs were based on the combination of single SPGs. These structures utilise partially or fully encircling corrugations of multiple periods, surrounding a single central nanohole. This resulted in multiple polarisation and wavelength selective behaviour. The structures have been developed, fabricated, characterised, and modelled for optical transmission, gated switching, and polarisation selective properties.

Initial design considered two single SPGs which were combined orthogonally around a single nanohole. The design considerations of grating periods, corrugation fan angles, transmission due to inner ring variations, and spectral separation of paired SPGs were investigated. The simulations were compared to the experimental results for agreement with the models.

The performance of this new structure was studied to determine its potential as a useful plasmonic device. It was found that the paired SPGs offer discrete polarisation dependent transmission states.

This was followed by a discussion of the work on multi-state surface plasmon generators consisting of three and four partially encircling SPG structures. These

were fabricated and the triplet-SPG was experimentally characterised. From the experimental results it was found that the individual peaks are detectable, but there was a lot of coupling between each of the three individual SPGs. This prevented the spectrum from having separate, discrete transmission states associated with each SPG segment, causing a continually varying spectrum.

The results from the paired and triplet SPG designs have led to the work on a multi-state surface plasmon generator structure with the fully encircling SPG structure. The new geometry was designed to provide a linear relationship between the change in the polarisation angle and the change in the corrugation period. Therefore, the geometry offered continual, light polarisation tuneable peak transmission wavelength.

5.5 Discussion and implications

Previous studies on circular surface plasmon antennae structures have investigated the effects of variables such as corrugation period and depth (Shuford et al. 2006), while their susceptibility to incident light polarisation has received less attention.

A range of simple and complex wavelength and polarisation selective polariton generator (SPG) structures have been modelled, developed, fabricated and characterised. By varying SPG designs around a central nanohole we achieved operation of nanophotonic devices where optical transmission peak wavelengths are controlled via the polarisation state of the incident photons.

These are based on the principles of circular surface plasmon antennae and exhibit various polarisation selective light transmission behaviour. These SPGs have been simulated, fabricated, and tested for optical transmission, gated switching, and polarisation selective properties using a purpose-built spectral transmission microscope.

The polarisation-sensitive structures combine a tuneable plasmon resonator, surface corrugations, and a subwavelength aperture to selectively generate and transmit polaritons of a desired wavelength through a central nanohole. By specifying surface geometry and polarisation orientation, we can control the operational characteristics of these elements. Polariton generation is enabled or disabled by selecting the desired photon polarisation to interact with a specific geometric aspect of the structure.

Transmission intensity is determined by photon polarisation relative to the geometric orientation of the polariton generator, leading to a selective photon-polariton coupling mechanism. This was used to gate light propagation through the central nanohole in a switch-like fashion.

Through FDTD modelling and reference to our experimental results, simulations looked at various configurations towards customising single and paired SPGs for desired polarisation and wavelength selective transmission. The design considerations of grating periods, corrugation fan angles, transmission due to inner ring variations, and spectral separation were investigated along with flanking the structures with Bragg reflector corrugations.

Individual SPGs permitted on-off gated-switching of transmission intensity, with calculated enhanced optical transmission of up to 10 and up to 4-fold measured amplitude modulation. The paired SPGs gave rise to multiple spectrally discrete transmission peaks which when modulated provide multi-state operation in a single device. The measured amplitude modulation was up to 10-fold. For the linearly continuous SPG, by controlling the polarisation, as a tuning variable, it selectively generates and transports polaritons of a desired wavelength. The enhanced optical transmission was calculated to be up to 17.2. Both the experimental and simulated data exhibited the same spectral shift of 40 nm over the full range of polarisation angles, but over a slightly different transmission wavelength range.

Even though the work by Bravo-Abad ,Garcia-Vidal and Martin-Moreno (2003) offers simultaneous transmission of two different wavelengths, it does not offer selective transmission of each one at a time. Work in this thesis has made a contribution in the area of selective transmission properties of single subwavelength apertures, in thin metal film, flanked by asymmetric configurations of periodic grooves.

In an attempt to improve the SPG functionality, the use of plasmonic Bragg reflectors was investigated. This was encouraged by the report of enhancing the enhanced optical transmission of the nanohole array system by flanking them with various plasmonic Bragg reflector configurations (Marthandam and Gordon 2007).

The addition of Bragg reflectors to a single SPG, resulted in the largest enhancement for the SPGs with only two resonant corrugations. This was due to the least distance the reflected polaritons had to travel before reaching the central ;nanohole. However, due to only two resonant corrugations, the resonant condition was not tightly bound, resulting in wide spectral width.

Due to the exponential decay of travelling surface plasmon polaritons, none of the Bragg reflector flanked configurations offered a higher transmission peak than the SPG with four resonant corrugations. Therefore, Bragg reflectors do not provide advantageous transmission enhancement for SPG configurations with more than three resonant corrugations.

For transmission through a single nanoscale aperture, if the diffraction pattern is scanned along the direction of incoming polarisation, the intensity should be constant (like a spherical wave plane). On the other hand, in the perpendicular direction, the intensity decreases with increasing angle (Bethe 1944). In the later, the angular dependence is a $\cos^2\theta$ function. The transmission intensity of single

and paired SPGs were seen to follow a $\cos^2\theta$ relationship using the polar plots for various light polarisation angles, agreeing with the predictions from the literature.

Each of the SPG structures shown, fundamentally consists of two components: a photon antenna (polariton generator); and a nanohole (polariton channel). The photon antenna is formed by corrugations on the gold film surface that partially encircle the nanohole. This grating provides the necessary geometry for photon energy transfer via momentum matching between incident photons and the collective electron wave oscillation. The nanohole located in the middle acts as a channel that facilitates the propagation of polaritons through to the opposite side of the gold film (Degiron et al. 2004; Chang et al. 2005).

Spectral transmission characteristics and peak wavelength are selected based on antenna features such as corrugation period and depth. The transmission amplitude is determined by photon polarisation relative to the geometric orientation of the polariton generator. Therefore, a selective photon-polariton coupling mechanism can be made to gate light propagation through the nanohole in a switch-like fashion.

Based on the versatility of SPG designs and characteristics, these structures have the potential for further research and application in areas ranging from polariton generators, and multi-state nanophotonic switching and devices, to tuneable spectroscopic elements and biosensors.

5.5.1 Limitations of the study and future research

Regarding the work on selective polaritons generators (SPGs), while the work by Bravo-Abad, Garcia-Vidal and Martin-Moreno (2003) offers simultaneous transmission of two different wavelengths, it does not offer selective transmission of each one at a time. Also, by tuning the geometric parameters defining the

corrugation of the output side, these two wavelengths can emerge from the structure as two very narrow beams propagating at well-defined directions. A recommendation for future work on the SPG designs is to mirror the corrugation geometry onto the exit side of the nanohole, so to confine the emerging light to a small angle of divergence. This should provide a higher intensity signal along with directionality.

Another group presented a new design configuration of nanohole arrays, with finite-difference time-domain simulations showing that transmission efficiency may reach 80% in the visible spectral range (Baida and Labeke 2003). This was achieved by filling the central region of each hole with a concentric cylinder of a smaller diameter, resulting in a periodic array of annular apertures. Their work could offer another potential improvement to the current SPG designs by replacing the central nanohole with an annular aperture, increasing transmission efficiency.

An aspect of future work should consider the implementation of surface chemistry for actual bio-chemical sensing applications. These are to utilise various improvements brought about with the design modifications presented in this thesis.

Chapter 6

6 CONCLUSION

The purpose of this research was the development and characterisation of nanophotonic devices, which utilise plasmonic phenomena and have potential for sensor applications. The key elements of the research were design, fabrication, testing, and optimisation of devices. This chapter concludes the research by recalling the thesis aims and objectives, commenting on the findings and discusses the implications of the study.

The foundation of plasmonic based sensors was the utilising of a photon coupling mechanism into oscillating electron waves, plasmon resonance condition. This research enquired to combine aspects of electronics, photonics, and nanotechnology to develop, characterise, and report on new plasmonic devices.

The first objective of the research was to develop and characterise a gold grating surface plasmon resonance sensor platform for use with one or multiple target samples. It further looked into improving the platform sensitivity along with utilising a low cost substrate (Sedoglavich et al. 2007b, 2007a; Sedoglavich et al. 2008b).

The platform offers improved sensing performance by combining SPR angular interrogation with the PPC technique. This work provided an incremental step towards taking the large scale SPR analyses to a lower cost, desktop format. Based on the results presented, it is feasible that the technique could be implemented for a number of biological and physical applications where screening of very large number of samples may be beneficial.

The phase-polarisation contrast technique was implemented within the SPR analysis platform due to its signal enhancement in non-optimum SPR coupling conditions.

The second objective was to gain understanding into the operation of localised surface plasmon resonance devices. The aim was to develop an instrument for resolving transmission of single nanoholes, by scanning over the nanohole array surface, as a tool for characterising individual nano-scale devices. This work has contributed to the publication on implementation of gold nanohole arrays as immunoassays (Sharpe et al. 2008).

Although past diffraction limit, we have shown that our instrument can produce spectral characteristics of single holes. A potential application for individual nanostructure analyses arises in arrays of nanostructures where individual ones are treated as individual sensors. Such access to individual elements as single sensing units permits for the design of large scale sensor array platforms, e.g. nanohole arrays where each aperture is a sensor. A modified version of the instrument was utilised for characterising behaviour of various nano-scale geometries with polarisation and wavelength dependent transmission.

The third objective was to model, develop, fabricate, and characterise new nanophotonic structures based on plasmonic phenomena. The intent of this objective was to explore new designs of nanophotonic structures utilising selective behaviour based on the polarisation and wavelength of incident light. Data from the finite-difference time-domain software simulation and the experimental results of the fabricated structures were presented (Sedoglavich et al. 2008a; Sedoglavich et al. 2008c; Sedoglavich et al. 2009).

A range of simple and complex wavelength and polarisation selective polariton generator structures were designed. Individual SPGs permitted on-off

gated-switching of transmission intensity. The paired SPGs gave rise to multiple spectrally discrete transmission peaks which when modulated provide multi-state operation in a single device. For the linearly continuous SPG, by controlling the polarisation, as a tuning variable, it selectively generated and transported polaritons of a desired wavelength.

The findings of this study should provide helpful information about the instrumental design of surface plasmon resonance imaging platforms and open new avenues into nanophotonic structures which offer polarisation and wavelength selective behaviour. This selective behaviour may find the potential for further research and applications in areas ranging from polariton generators, and multi-state nanophotonic switching and devices, to tuneable spectroscopic elements and biosensors.

Appendices

Appendix A

The hardware and software description of the spin coater designed for placing thin films of polyvinyl alcohol onto bare gold CD-R surfaces.

```
// ------------------------------------------------------------------------
// CD-drive motor acceleration control - Single Edge Control PWM output
// Engineer: Nemanya Sedoglavich
// Date: 18/10/06
// System designed for a reliable & controllable thin film spin coating onto the gold CD-R grating
// surface.
// ------------------------------------------------------------------------

#include <LPC21xx.H>                    // LPC21xx definitions

void delay(unsigned long int);

void init_PWM (void){
  PINSEL0 = 0x00000002;          // PWM1 P0.0
  PWMPC = 1;                     // controls division of pclk by some constant
                                 // value before it is applied to the PWM Timer Counter
  PWMPR = 0x000000500;           // Load Prescaler

  PWMPCR = 0x00000200;           // PWM channel 1 single edge control, PWM1 output enabled
  PWMMCR = 0x00000003;           // an interrupt is generated when PWMMR0 matches the value
                                 // in the PWMTC. The PWMTC will be reset if PWMMR0
                                 matches it.
                                 // a.k.a. On match with timer reset the counter
  PWMMR0 = 0x0000036D;           // PWM cycle rate. 1236 => ~140 msec

  PWMLER = 0x00000003;           //enable shadow latch for match 0 and 1
  PWMTCR = 0x00000002;           // the PWM Timer Counter and the PWM Prescale Counter are
                                 // synchronously reset on the next positive edge of pclk.
  PWMTCR = 0x00000009;           // the PWM Timer Counter and PWM Prescale Counter are
                                 // enabled for counting. PWM mode is enabled.
}
```

```
void main (void) {
        int i;

 init_PWM();

  while (1) {              // Loop forever

// Slow acceleration
 for(i = 0; i <= 400; i++){

 PWMMR1 = 0x000000FF;      // Match0 value. Duty cycle = 100%x(MR1/MR0)
 PWMLER = 0x00000002;      // allows the last value written to the PWM Match 1 register to
                           // be
                           // become effective when the timer is next reset by a PWM
                           // Match event.
                           // set latch to update PWM registers next cycle

 delay(250000);            // time delay

 PWMMR1 = 0x0000000A;      // Match0 value. Duty cycle = 100%x(MR1/MR0)
 PWMLER = 0x00000002;      // allows the last value written to the PWM Match 1 register to
                           // be
                           // become effective when the timer is next reset by a PWM
                           // Match event.
                           // set latch to update PWM registers next cycle

 delay(630000);            // time delay
}

 PWMMR1 = 0xFFFFFFFF;      // Match0 value. Duty cycle = 100%x(MR1/MR0)
 PWMLER = 0x00000002;      // allows the last value written to the PWM Match 1 register to
                           //be
                           // become effective when the timer is next reset by a PWM
                           // Match event.
                           // set latch to update PWM registers next cycle
for(i = 0; i <= 20; i++){
 delay(100000000);         // time delay
```

```
}

 PWMMR1 = 0x00000000;          // Match0 value. Duty cycle = 100%x(MR1/MR0)
 PWMLER = 0x00000002;          // allows the last value written to the PWM Match 1 register to
                               // be
                               // become effective when the timer is next reset by a PWM
                               // Match event.
                               // set latch to update PWM registers next cycle

 delay(800000000);             // time delay
 }
}

/************************/
/* Delay Time Function */
/*    1-4294967296     */
/************************/
void delay(unsigned long int count1){
 while(count1 > 0){
   count1--;
 }                             // Loop Decrease Counter
}
```

Appendix B

The MATLAB file used for processing the raw SPR data for the CD SPR platform.

```
% SPR image/raw data processing for the CD SPR platform
% Nemanya Sedoglavich
% 28-05-2006
clear all

%figure(3)
I = imread('co2 t2.tif');
%imview(I)

I = imrotate(I,(-90 + 4.75));   % rotate the image by 4.75 degrees
%imview(I)
I3 = I;

% Gaussian filter - along the vertical dimention
Sigma = 10;
Hsize = [60, 1];    % Kernel
H = FSPECIAL('gaussian',Hsize,Sigma);
I_blurred = imfilter(I,H,0);
%I3 = I_blurred;

%f = fft2(double(I_blurred));
%imshow(fftshift(log(abs(real(f)))),[])

I = I_blurred;

% Gaussian filter - along the horizontal dimention
Sigma = 3;
Hsize = [1, 23];    % Kernel
H = FSPECIAL('gaussian',Hsize,Sigma);
I_blurred = imfilter(I,H,0);
%figure(3)
```

```
%imshow(I_blurred)
%imview(I_blurred)

%f = fft2(double(I_blurred));
%imshow(fftshift(log(abs(real(f)))),[])

%I3 = I_blurred;
%I = im_final;
%I_temp = I;
I = I_blurred;

[r_size c_size] = size(I);

                % 1 : 1 : r_size
                % 100 : 1 : 1327
line_height_domain = 100 : 1 : 1327;
for line_height = line_height_domain

%line_height
%I = I_temp;

figure(1)
%plot(I3(line_height,:))
%pause();
%plot(I2(line_height,:))
%pause();
%plot(I(line_height,:))
%pause();
%I = I3;

% convert the image line into a vector
Line_y = double(I(line_height,:)');
Line_x = (1:1:c_size)';

% remove the black frame around the image, made by rotation
[r_line c_line] = size(Line_y);
```

```
for i = 1 : 1 :  r_line
   if Line_y(i) <= 9000
      Line_y(i) = 65520;
   end
end

% find coordinates for the minimum intensity value.
[min_y min_x] = min(Line_y(110:1000));
min_x =min_x+109;

% find the maximum intensity value
max_y = max(Line_y(110:1000));
upper_limit = 0.93 * max_y;

% find the closest max value to the sides of the min
%   use those as the domain values for the polyfit
domain_left = min_x;
domain_right = min_x;
first_left = 0;
first_right = 0;

% x-axis domain
for x = 1 : 1 : c_size
   % bottom SPR limit
   if min_x - x <= 0
      domain_left = 1;
      first_left = 1;
      break;
   end
   % top SPR limit
   if min_x + x >= 1000
      domain_right = 1000;
      first_right = 1;
      break;
   end
   if Line_y(min_x + x) >= upper_limit
      if first_right == 0
```

```
            domain_right = min_x + x;
            first_right = 1;
        end
    end
    if Line_y(min_x - x) >= upper_limit
        if first_left == 0
            domain_left = min_x - x;
            first_left = 1;
        end
    end
    if first_right == 1 && first_left == 1
        break;
    end
end

%domain_left;
%domain_right;

% slightly expand the polyfit region
domain_left = domain_left - 20;
domain_right = domain_right + 20;

% ================================================================
figure(1)
hold on
% polyfit 4th or 5th order fit
p = polyfit(Line_x(domain_left:domain_right),Line_y(domain_left:domain_right),4);

%To see how good the fit is, evaluate the polynomial at data points with
resolution = 0.1;
domain = domain_left : resolution : domain_right;  % increase poyval resolution
f = polyval(p,domain);

domain_units = domain .* (3.14*10^-3);
plot(domain_units, f, 'color','r')
%pause();
%hold on
```

```
% local minima
[min_y min_x] = min(f);
SPR_intenisty = min_y;
SPR_position = domain_left + (min_x.*resolution);
%k = polyder(p)  % returns the derivative of the polynomial p
%f = polyval(k,Line_x(468:525));
%plot(Line_x(468:525), f, 'color','g')

% ====================================================================

SPR_curve(line_height) = SPR_position;
%[r_p c_p] = size(f);
%curve(line_height, 1 : 1 : c_p) = f;
hold off
end

figure(2)
%plot(1:r_size, SPR_curve(1:r_size)')
micro_line_height_domain = line_height_domain.*4.65;
SPR_curve_angle = SPR_curve.*(3.14*10^-3);  % Angle
SPR_curve_n = SPR_curve_angle.*(0.01207);  % RIU
plot(micro_line_height_domain, SPR_curve_n(line_height_domain)')
axis([300 6200 -0.01 0.03]) %axis([300 6200 -0.00035 0.00035])  % axis([xmin xmax ymin ymax])
xlabel('Image position [\mum]')
ylabel('Arb SPR response \Deltan [RIU]')
title('Arb SPR RIU response')
%legend('Air', 'CO_2')
grid on
% ====================================================================

%hold on
% polyfit on the entire SPR image
%p2 = polyfit(115:280, SPR_curve(115:280),1);

%To see how good the fit is, evaluate the polynomial at data points with
```

```
%f2 = polyval(p2,115:280);
%plot(115:280, f2, 'color','r')
%hold on

% polyfit on the entire SPR image
%p3 = polyfit(310:970, SPR_curve(310:970),1);

%To see how good the fit is, evaluate the polynomial at data points with
%f3 = polyval(p3,310:970);
%plot(310:970, f3, 'color','r')
%hold on

% polyfit on the entire SPR image
%p4 = polyfit(1100:1400, SPR_curve(1100:1400),1);

%To see how good the fit is, evaluate the polynomial at data points with
%f4 = polyval(p3,1100:1400);
%plot(1100:1400, f4, 'color','r')
%hold on

hold off

save('co2 t2', 'SPR_curve_n')
figure(2)
hgsave('co2 t2 SPR graph')
figure(1)
hgsave('co2 t2 SPR curves')
save('co2 t2', 'curve')
```

Appendix C

MATLAB code for calculation the SPR angle.

```
function SPR_angle_calculation

% Calculation of the SPR angle using the momentum matching equation of the
% incident light and the plasmons on the gold grating
clear all

lambda_0 = 670*10^-9;   % excitiation wavelength Laser Diode
m = 1;                  % diffraction order
period = 1560*10^-9;    % period of the grating

E_m1 = -11.84;          % electric permitivity of gold, real
E_m2 = i*1.36;          % electric permitivity of gold, imaginary
E_m = E_m1 + E_m2;

%E_d = [air 1.000584;       CO2 1.0008982;  Helium 1.000070

E_d = 1.000584; %n = 1.000292;    % Air

Theta_0_1 = asin(((2*pi/lambda_0)*sqrt((E_m1 * E_d)/(E_m1 + E_d)) - (m*2*pi/period))
/(2*pi/lambda_0))
Theta_0_deg_1 = Theta_0_1 * 180 /pi

E_d = 1.0008982; %n = 1.000449;  % CO2

Theta_0_2 = asin(((2*pi/lambda_0)*sqrt((E_m1 * E_d)/(E_m1 + E_d)) - (m*2*pi/period))
/(2*pi/lambda_0))
Theta_0_deg_2 = Theta_0_2 * 180 /pi

E_d = 1.000070 ; %n = 1.000035;   % Helium

Theta_0_3 = asin(((2*pi/lambda_0)*sqrt((E_m1 * E_d)/(E_m1 + E_d)) - (m*2*pi/period))
/(2*pi/lambda_0))
```

```
Theta_0_deg_3 = Theta_0_3 * 180 /pi

Delta_Theta_0_deg = abs(Theta_0_deg_2 - Theta_0_deg_1)
clear all
clear figure
```

Appendix D

The script for analysis of the finite-difference time-domain simulations designed in FDTD Solutions.

```
################################################
# File: power_in_cone15deg.lsf
#
# This file will calculate the transmission properties of a SPG
# for a 15 degrees cone and a full cone of transmission.
################################################

clear;

# choose the half angle over which we will integrate
half_angle = 15; #in degrees

sim_name="bullseye_ring";
do_farfield = 1;                    # 1 = do farfield, 0 = load presaved data
mname="transmission";               # monitor name
na=150;                             # points in far field projection

f=getdata(mname,"freqDFT");
x=getdata(mname,"x");
y=getdata(mname,"y");
nf=length(f);
ff_data=matrix(na,na,nf);  # matrix for storing far field data

if (do_farfield) {  # compute far field projections
   for (i=1:nf) {
      ff_data(1:na,1:na,i)= farfield3d(mname,i,na,na);
      ?num2str(i/nf*100);           # progress counter
   }
   ux = farfieldux(mname,i,na,na);
   uy = farfielduy(mname,i,na,na);
   savedata(sim_name,ff_data,ux,uy);
```

```
} else {
   loaddata(sim_name);
}

# Calculate total transmission
T_total=transmission(mname);

# new integration calculation
# Filter not required for cones
# See link for details:
# http://www.lumerical.com/fdtd_online_help/ref_fdtd_scripts_farfield3dintegrate.php
T_cone=matrix(nf);
for (i=1:nf) {
  E2=pinch(ff_data,3,i);
 # find the fraction of light in the half_angle compared to 90 degrees
  p_90=   farfield3dintegrate(E2,ux,uy, 89.9, 0,0);
  p_cone= farfield3dintegrate(E2,ux,uy, half_angle, 0,0);
  fraction_in_cone = p_cone/p_90;
  T_cone(i) = fraction_in_cone * T_total(i); # scale by transmission
}

# set up an integration mesh, and angle filters
#T_cone=matrix(nf);
#Ux = meshgridx(ux,uy);
#Uy = meshgridy(ux,uy);
#Uz = sqrt(1 - Ux^2 - Uy^2);
#cos_theta = real(Uz) + 1e-20; # avoid divide by zero errors
#filter_90= ( sqrt(Ux^2+Uy^2) <= sin(89.9*pi/180) ); # only allowed to integrate up to 89.9
degrees to avoid numerical problems
#filter = real(acos( Uz  )) <= half_angle*pi/180;
#filter = filter * filter_90;

#image(ux,uy,filter,"","","Angular integration region","polar");
#for (i=1:nf) {
#  E2=pinch(ff_data,3,i);

#  # find the fraction of light in the half_angle compared to 90 degrees
```

```
#fraction_in_cone=integrate(E2*filter/cos_theta,1:2,ux,uy)/integrate(E2*filter_90/cos_theta,1:2,ux
,uy);
#  T_cone(i) = fraction_in_cone * T_total(i); # scale by transmission
#}

plot(c/f*1e9,T_total, T_cone,
        "Wavelength (nm)","Power (normalized)");
legend("Total","Cone");

write("Transmission15degCone.txt",num2str(T_cone));
write("TransmissionTotal.txt",num2str(T_total));
write("Wavelength.txt",num2str(transpose(c/f*1e9)));
```

Appendix E

The procedure for patterning a bitmap of nanostructures using focused ion beam milling.

Therefore, the RGB control of the FIB milling is as follows:
RGB 0 / 0 / 0 (black) Beam is blanked
RGB 0 / 1 / 0 Beam is on, 100ns min dwell time
RGB 0 / 1 / 255 Beam is on, Maximum dwell time
RGB 255 / 255 / 255 (white) Beam is on, Maximum dwell time

A procedure for milling a bitmap has several steps. After selecting a patterning page control, the bitmap shape is selected on the bottom of the pattern selection dropdown menu. A square is dragged onto the screen that represents the area of patterning. The position of the square can be changed by dragging. Then, the bitmap layout pattern is loaded using the open dialog by selecting File in the properties menu. The bitmap appears in the imaging quad. At this point, one can modify layout size and aspect ratio to Free or Fixed depending if the bitmap is required to stretch. Then, the patterning can begin.

Reference

Abeles, F. 1976. Surface electromagnetic waves ellipsometry. *Surface Science* 56 237-51.

Baida, F. I. and D. V. Labeke. 2003. Three-dimensional structures for enhanced transmission through a metallic film: Annular aperture arrays. *Physical Review B* 67(15) 155314-1 - -7.

Barnes, W. L., A. Dereux and T. W. Ebbesen. 2003. Surface plasmon subwavelenght optics. *Nature* 424 824-30.

Bethe, H. A. 1944. Theory of Diffraction by Small Holes. *Physical Review* 66(7&8) 163-82.

Betzig, E. and J. K. Trautman. 1992. Near-Field Optics: Microscopy, Spectroscopy, and Surface Modification Beyond the Diffraction Limit. *Science* 257 189-95.

Bravo-Abad, J., F. J. Garcia-Vidal and L. Martin-Moreno. 2003. Wavelength de-multiplexing properties of a single aperture flanked by periodic arrays of indentations. *Photonics and Nanostructures - Fundamentals and Applications* 1 55-62.

Brolo, A. G., R. Gordon, B. Leathem and K. L. Kavanagh. 2004. Surface Plasmon Sensor Based on the Enhanced Light Transmission through Arrays of Nanoholes in Gold Films. *Langmuir* 20(12) 4813-5.

Chang, S.-H., S. K. Gray and G. C. Schatz. 2005. Surface plasmon generation and light transmission by isolated nanoholes and arrays of nanoholes in thin metal films. *Optics Express* 13(8) 3150-65.

Chen, Y., Y. Wang, Y. Zhang and S. Liu. 2007. Numerical investigation of the transmission enhancement throguh subwavelength hole array. *Optics Communications* 274 236-40.

Csaki, A., A. Steinbruck, S. Schroter and W. Fritzsche. 2006. Combination of Nanoholes with Metal Nanoparticles - Fabrication and Characterisation of Novel Plasmonic Nanostructures. *Plasmonics* 1 147-55.

Cubukcu, E., E. A. Kort, K. B. Crozier and F. Capasso. 2006. Plasmonic laser antenna. *Applied Physics Letters* 89(9) 093120-1 - -3.

Cui, Y., M. T. Bjork, J. A. Liddle, C. Sonnichsen, N. Boussert and P. A. A. 2004. Integration of colloidal nanocrystals into lithographically patterned devices. *Nano Letters* 4(6) 1093-8.

Cullen, D. C., R. G. W. Brown and C. R. Lowe. 1987. Detection of Immuno-complex Formation via Surface Plasmon Resonance on Gold-coated Diffraction Gratting. *Biosensors* 3 211-25.

Degiron, A. and T. W. Ebbesen. 2004. Analysis of the trasnsmission process through single aperture surrounded by periodic corrugations. *Optics Express* 12(16) 3694-700.

Degiron, A. and T. W. Ebbesen. 2005. The role of localised surface plasmon modes in the enhanced transmission of periodic subwavelength apertures. *Journal of Optics A: Pure and Applied Optics* 7 90-6.

Degiron, A., H. J. Lezec, N. Yamamoto and T. W. Ebbesen. 2004. Optical transmission properties of a single subwavelength aperture in a real metal. *Optics Communications* 239 61-6.

DiMaio, J. R. and J. Ballato. 2006. Polarization-dependent transmission through subwavelength anisotropic aperture arrays. *Optics Express* 14(6) 2380-4.

Ebbesen, T. W., H. J. Lezec, H. F. Ghaemi, T. Thio and P. A. Wolff. 1998. Enhanced optical transmission through sub-wavelength hole arrays. *Nature* 391 667-9.

Fontana, E. 2004. Theoretical and experimental study of the surface plasmon resonance effect on a recordable compact disk. *Applied Optics* 43(1) 79-87.

Garcia-Vidal, F. J., H. J. Lezec, T. W. Ebbesen and L. Martin-Moreno. 2003. Multiple Paths to Enhance Optical Transmission through a Single Subwavelength Slit. *Physical Review Letters* 90(21) 213901-1 - -4.

Garcia-Vidal, F. J., E. Moreno, J. A. Porto and L. Martin-Moreno. 2005. Transmission of light through a single rectangular hole. *Physical Review Letters* 95(10) 103901.

Genet, C. and T. W. Ebbesen. 2007. Light in tiny holes. *Nature* 445 39-46.

Gordon, R. and A. G. Brolo. 2005. Increased cut-off wavelength for a subwavelength hole in a real metal. *Optics Express* 13(6) 1933-8.

Gordon, R., A. G. Brolo, K. L. Kavanagh, D. Sinton and J. Pond. 2004. Understanding the Enhanced Optical Properties of Nanohole Arrays in Metals. *Photons* 2(1) 15-8.

Gordon, R., L. K. S. Kumar and A. G. Brolo. 2006. Resonant Light Transmission Through a Nanohole in a Metal Film. *IEEE Transactions on Nanotechnology* 5(3) 291-4.

Hofmann, C. E., E. J. R. Vesseur, L. A. Sweatlock, H. J. Lezec, F. J. G. d. Abajo, A. Polman and H. A. Atwater. 2007. Plasmonic Modes of Annular Nanoresonators Imaged by Spectrally Resolved Cathodoluminescence. *Nano Letters* 7(12) 3612-7.

Homola, J., I. Koudela and S. S. Yee. 1999a. Surface plasmon resonance sensors based on diffraction gratings and prism couplers: sensitivity comparison. *Sensors and Actuators B* 54 16-24.

Homola, J., S. S. Yee and G. Gauglitz. 1999b. Surface plasmon resonance sensors: review. *Sensors and Actuators B* 54 3-15.

Huang, F. M. and N. Zheludev. 2007. Focusing of light by a nanohole array. *Applied Physics Letters* 90(9) 091119-1 -3.

Ishi, T., J. Fujikata, K. Makita, T. Baba and K. Ohashi. 2005. Si Nano-Photodiode with a Surface Plasmon Antenna. *Japanese Journal of Applied Physics* 44(12) 364-6.

Jory, M. J., G. W. Bradberry, P. S. Cann and J. R. Sambles. 1995. A surface-plasmon-based optical sensor using acousto-optics. *Meas. Sci. Technol.* 6 1193–200.

Jory, M. J., P. S. Vukusic and J. R. Sambles. 1994. Development of a prototype gas sensor using surface plasmon resonance on gratings. *Sensors and Actuators B* 17 203-9.

Kabashin, A. V., V. E. Kochergin, A. A. Beloglazov and P. I. Nikitin. 1998. Phase-polarisation contrast for surface plasmon resonance biosensors. *Biosensors & Bioelectronics* 19 1263-9.

Kochergin, V. E., A. A. Beloglazov, M. V. Valeiko and P. I. Nikitin. 1998. Phase properties of a surface-plasmon resonance from the viewpoint of sensor applications. *Quantum Electronics* 25(5) 444-8.

Kreibig, U. and M. Vollmer. 1995. *Cluster Materials*. Heidelberg, Germany: Springer-Verlag

Kretschmann, E. and H. Raether. 1968. Radiative decay of non-radiative surface plasmons excited by light *Z. Naturforsch* 23A 2135-6.

Lakowicz, J. R. 2005. Radiative decay engineering 5: metal-enhanced fluorescence and plasmon emission. *Analytical Biochemistry*(337) 171-94.

Lawrence, C. R., N. J. Geddes, D. N. Furlong and J. R. Sambles. 1996. Surface plasmon resonance studies of immunoreactions utilizing disposable diffraction gratings. *Biosensors & Bioelectronics* 11(4) 389-400.

Lee, K.-L., C.-W. Lee, W.-S. Wang and P.-K. Wei. 2007. Sensitive biosensor array using surface plasmon resonance on metallic nanoslits. *Journal of Biomedical Optics* 12(4) 044023-1 - -5.

Leebeeck, A. D., L. K. S. Kumar, V. D. Lange and D. Sinton. 2007. On-Chip Surface-Based Detection with Nanohole Arrays. *Analytical Chemistry* 79(11) 4094-100.

Lesuffleur, A., L. K. S. Kumar, A. G. Brolo, K. L. Kavanagh and R. Gordon. 2007. Apex-Enhanced Raman Spectroscopy Using Double-Hole Arrays in a Gold Film. *The Journal of Physical Chemistry C Letters* 111(6) 2347-50.

Levene, M. J., J. Korlach, S. W. Turner, M. Foquet, H. G. Craighead and W. W. Webb. 2003. Zero-Mode Waveguides for SIngle-Molecule Analysis at High Concentrations. *Science* 299 682-6.

Lezec, H. J., A. Degiron, E. Devaux, R. A. Linke, L. Martin-Moreno, F. J. Garcia-Vidal and T. W. Ebbesen. 2002. Beaming Light from a Subwavelength Aperture. *Science* 297 820-2.

Liedberg, B., C. Nylander and I. Lundstrom. 1995. Biosensing with surface plasmon resonance - how it all started. *Biosensors & Bioelectronics* 10 1-9.

Lin, L., R. J. Reeves and R. J. Blaikie. 2006. Surface-plasmon-enhanced light transmission through planar metallic films. *Physical Review B* 74(15) 155407-1 - -6.

Liu, Z., J. M. Steele, W. Srituravanich, Y. Pikus, C. Sun and X. Zhang. 2005. Focusing Surface Plasmon Resonance with Plasmonic Lens. *Nano Letters* 5(9) 1726-9.

Lumercial Solutions, I. 2008. *FDTD Solutions User Manual, Release 6.0*: Lumerical Solutions, Inc.

Marthandam, P. and R. Gordon. 2007. Plasmonic Bragg reflectors for enhanced enhanced optical transmission through nano-hole arrays in a gold film. *Optics Express* 15(20) 12995-3002.

Martin-Moreno, L., F. J. Garcia-Vidal, H. J. Lezec, A. Degiron and T. W. Ebbesen. 2003. Theory of Highly Directional Emission from a Single Subwavelength Aperture Surrounded by Surface Corrugations. *Physical Review Letters* 90(16) 167401-1 - -4.

Matsuura, K. 2007. MUE20901 CFI LU Plan Epi ELWD 100X Objective Lens, 14-05-2007.

Nelson, B. P., T. E. Grimsrud, M. R. Liles, R. M. Goodman and R. M. Corn. 2001. Surface Plasmon Resonance Imaging Measurements of DNA and RNA Hybridization Adsorption onto DNA Microarrays. *Analytical Chemistry* 73(1) 1-7.

Nikitin, P. I. and A. A. Beloglazov. 1994. A multi-purpose sensor based on surface plasmon polariton resonance in a Schottky structure. *Sensors and Actuators A* 41-42 547-52.

Nikitin, P. I., A. A. Beloglazov, V. E. Kochergin, M. V. Valeiko and T. I. Ksenevich. 1999. Surface plasmon resonance interferometry for biological and chemical sensing. *Sensors and Actuators B* 54 43-50.

Nikitin, P. I., A. A. Beloglazov, M. V. Valeiko, J. A. Creighton, A. M. Smith, N. A. J. M. Sommerdijk and J. D. Wright. 1997. Silicon-based surface plasmon resonance chemical sensors. *Sensors and Actuators B* 38-39 53-7.

Nikitin, P. I., A. N. Grigorenko, A. A. Beloglazov, M. V. Valeiko, A. I. Savchuk, O. A. Savchuk, G. Steiner, C. Kuhne, A. Huebner and R. Salzer. 2000. Surface plasmon resonance interferometry for micro-array biosensing. *Sensors and Actuators* 85 189-93.

Njoh, K., S. Chappell, R. Errington and P. Smith. 2007. Optical antenna arrays in the visible range. *Optics Express* 15(6) 3478-87.

Otto, A. 1968. Excitation of surface plasma waves in silver by the method of frustrated total reflection *Z. Physik* 216 398-410.

Pockrand, I. and H. Raether. 1976. Surface Plasma Oscillations in Silver Films with wavy surface profiles: a quantitative experimental study. *Optics Communications* 18(3) 395-9.

Popov, E., N. Bonod, M. Neviere, H. Rigneault, P.-F. Lenne and P. Chaumet. 2005a. Surface plasmon excitation on a single subwavelength hole in a metallic sheet. *Optical Society of America* 44(12) 2332-7.

Popov, E., M. Neviere, A.-L. Fehrembach and N. Bonod. 2005b. Enhanced transmission of light through a circular structured aperture. *Applied Optics* 44(32) 6898-904.

Prikulis, J., P. Hanarp, L. Olofsson, D. Sutherland and M. Kall. 2004. Optical Spectroscopy of Nanometric Holes in Thin Gold Films. *Nano Letters* 4(6) 1003-7.

Rehwald, S., M. Berndt, F. Katzenberg, S. Schwieger and E. Runge. 2007. Tunable nanowires: An additional degree of freedom in plasmonics. *Physical Review Letters B* 76(8) 085420-1 -4.

Rigneault, H., J. Capoulade, J. Dintinger, J. Wenger, N. Bond, E. Popov, T. W. Ebbesen and P.-F. Lenne. 2005. Enhancement of Single-Molecule Fluorescence Detection in Subwavelength Apertures. *Physical Review Letters* 95(11) 117401(4).

Rindzevicius, T., Y. Alaverdyan, A. Dahlin and F. Hook. 2005. Plasmonic Sensing Characteristics of Single Nanometric Holes. *Nano Letters* 5(11) 2335-9.

Sedoglavich, N., R. Künnemeyer and J. C. Sharpe. 2008a. Design considerations of selective polariton generators for multi-state plasmonic devices. *SPIE Optics and Photonics - Plasmonics: Metallic Nanostructures and Their Optical Properties VI*, 26, Aug. 2008, San Diego, California, USA., 26, Aug. 2008, Proc. SPIE 7032, 703222.

Sedoglavich, N., R. Künnemeyer and J. C. Sharpe. 2009. Polarization tunable selective polariton generator. *Applied Physics Letters* 94(10) 101111-3.

Sedoglavich, N., R. Künnemeyer, S. R. Talele and J. C. Sharpe. 2007a. Interferometric surface plasmon resonance based on low cost grating substrates. *SPIE Photonics West - Plasmonics in Biology and Medicine IV*, 14, Feb. 2007, San Jose, California, USA., 14, Feb. 2007, Proceedings of SPIE.

Sedoglavich, N., R. Künnemeyer, S. R. Talele and J. C. Sharpe. 2007b. Phase-polarisation contrast for surface plasmon resonance based on low cost grating substrates. *Advanced Materials & Nanotechnology 3*, 11-16 February 2007, Wellington, New Zealand, 11-16 February 2007.

Sedoglavich, N., R. Künnemeyer, S. R. Talele and J. C. Sharpe. 2008b. Phase-polarisation contrast for surface plasmon resonance based on low cost grating substrates. *Current Applied Physics* 8(3-4) 351-4.

Sedoglavich, N., J. Sharpe, R. Künnemeyer and S. Rubanov. 2008c. Polarisation and wavelength selective transmission through nanohole structures with multiple grating geometry. *Optics Express* 16(8) 5832-7.

Sharpe, J. C., J. Mitchell, L. Lin, N. Sedoglavich and R. Blaikie. 2008. Gold nanohole array substrates as immunobiosensors. *Analytical Chemistry* 80(6) 2244-9.

Shen, S., T. Liu and J. Guo. 1998. Optical phase-shift detection of surface plasmon resonance. *Applied Optics* 37(10) 1747-51.

Shinn, M. and W. M. Robertson. 2005. Surface plasmon-like sensor based on surface electromagnetic waves in a photonic band-gap material. *Sensors and Actuators B* 105 360-4.

Shuford, K. L., M. A. Ratner, S. K. Gray and G. C. Schatz. 2006. Finite-difference time-domain studies of light transmission through nanohole structures. *Applied Physics B* 84 11-8.

Shuford, K. L., M. A. Ratner, S. K. Gray and G. C. Schatz. 2007. Electric Field Enhancement and Light Transmission in Cylindrical Nanoholes. *Journal of Computational and Theoretical Nanoscience* 4(2) 239-46.

Singh, B. K. and A. C. Hillier. 2006. Surface Plasmon Resonance Imaging of Biomolecular Interactions on a Grating-Based Sensor Array. *Analytical Chemistry* 78(6) 2009-18.

Smith, E. A. and R. M. Corn. 2003. Surface plasmon resonance imaging as a tool to monitor biomolecular interactions in an array based format. *Applied Spectroscopy* 57(11) 320-32.

Steele, J. M., Z. Liu, Y. Wang and X. Zhang. 2006. Resonant and non-resonant generation and focusing of surface plasmons with circular gratings. *Optics Express* 14(12) 5664-70.

Vukusic, P. S., G. P. Bryan-Brown and J. K. Sambles. 1992. Surface plasmon resonance on grating as a novel means for gas sensing. *Sensors and Actuators B* 8 155-60.

Wilkop, T., Z. Wang and Q. Cheng. 2004. Analysis of μ-Contact Printed Protein Patterns by SPR Imaging with a LED Light Source. *Langmuir* 20(25) 11141-8.

Wood, R. W. 1902. On a remarkable case of uneven distribution of light in a diffraction grating spectrum. *Phil. Magm.* 4 396-402.

Wu, C.-M. and M.-C. Pao. 2004. Sensitivity-tunable optical sensors based on surface plasmon resonance and phase detection. *Optical Society of America* 12(15) 3509-14.

Xinglong, Y., W. Dingxin, W. Xing, D. Xiang, L. Wei and Z. Xinsheng. 2005. A surface plasmon resonance imaging interferometry for proteing micro-array detection. *Sensors and Actuators B* 108 765-71.

Yin, L., V. K. Vlasko-Vlasov, A. Rydh, J. Pearson, U. Welp, S. H. Chang, S. K. Gray, G. C. Schatz, D. B. Brown and C. W. Kimball. 2004. Surface plasmons at single nanoholes in Au films. *Applied Physics Letters* 85(3) 467-9.